ICNS 2021

The Seventeenth International Conference on Networking and Services

May 30th – June 3rd, 2021

ICNS 2021 Editors

Mary Luz Mouronte López, Universidad Francisco de Vitoria - Madrid, Spain

Manuela Popescu, IARIA, USA/EU

ICNS 2021

Foreword

The Seventeenth International Conference on Networking and Services (ICNS 2021), held between May 30 – June 3rd, 2021, continued a series of events targeting general networking and services aspects in multi-technologies environments. The conference covered fundamentals on networking and services, and highlighted new challenging industrial and research topics. Network control and management, multi-technology service deployment and assurance, next generation networks and ubiquitous services, emergency services and disaster recovery and emerging network communications and technologies were considered.

IPv6, the Next Generation of the Internet Protocol, has seen over the past three years tremendous activity related to its development, implementation and deployment. Its importance is unequivocally recognized by research organizations, businesses and governments worldwide. To maintain global competitiveness, governments are mandating, encouraging or actively supporting the adoption of IPv6 to prepare their respective economies for the future communication infrastructures. In the United States, government's plans to migrate to IPv6 has stimulated significant interest in the technology and accelerated the adoption process. Business organizations are also increasingly mindful of the IPv4 address space depletion and see within IPv6 a way to solve pressing technical problems. At the same time IPv6 technology continues to evolve beyond IPv4 capabilities. Communications equipment manufacturers and applications developers are actively integrating IPv6 in their products based on market demands.

IPv6 creates opportunities for new and more scalable IP based services while representing a fertile and growing area of research and technology innovation. The efforts of successful research projects, progressive service providers deploying IPv6 services and enterprises led to a significant body of knowledge and expertise. It is the goal of this workshop to facilitate the dissemination and exchange of technology and deployment related information, to provide a forum where academia and industry can share ideas and experiences in this field that could accelerate the adoption of IPv6. The workshop brings together IPv6 research and deployment experts that will share their work. The audience will hear the latest technological updates and will be provided with examples of successful IPv6 deployments; it will be offered an opportunity to learn what to expect from IPv6 and how to prepare for it.

Packet Dynamics refers broadly to measurements, theory and/or models that describe the time evolution and the associated attributes of packets, flows or streams of packets in a network. Factors impacting packet dynamics include cross traffic, architectures of intermediate nodes (e.g., routers, gateways, and firewalls), complex interaction of hardware resources and protocols at various levels, as well as implementations that often involve competing and conflicting requirements.

Parameters such as packet reordering, delay, jitter and loss that characterize the delivery of packet streams are at times highly correlated. Load-balancing at an intermediate node may, for example, result in out-of-order arrivals and excessive jitter, and network congestion may manifest as packet losses or large jitter. Out-of-order arrivals, losses, and jitter in turn may lead to unnecessary retransmissions in TCP or loss of voice quality in VoIP.

With the growth of the Internet in size, speed and traffic volume, understanding the impact of underlying network resources and protocols on packet delivery and application performance has assumed a critical importance. Measurements and models explaining the variation and interdependence of delivery characteristics are crucial not only for efficient operation of networks and network diagnosis, but also for developing solutions for future networks.

Local and global scheduling and heavy resource sharing are main features carried by Grid networks. Grids offer a uniform interface to a distributed collection of heterogeneous computational, storage and network resources. Most current operational Grids are dedicated to a limited set of computationally and/or data intensive scientific problems.

Optical burst switching enables these features while offering the necessary network flexibility demanded by future Grid applications. Currently ongoing research and achievements refers to high performance and computability in Grid networks. However, the communication and computation mechanisms for Grid applications require further development, deployment and validation.

We take here the opportunity to warmly thank all the members of the ICNS 2021 Technical Program Committee, as well as the numerous reviewers. The creation of such a high quality conference program would not have been possible without their involvement. We also kindly thank all the authors who dedicated much of their time and efforts to contribute to ICNS 2021.

Also, this event could not have been a reality without the support of many individuals, organizations, and sponsors. We are grateful to the members of the ICNS 2021 organizing committee for their help in handling the logistics and for their work to make this professional meeting a success.

We hope that ICNS 2021 was a successful international forum for the exchange of ideas and results between academia and industry and for the promotion of progress in the fields of networking and services.

We are convinced that the participants found the event useful and communications very open.

ICNS 2021 Chairs:

ICNS 2021 Steering Committee
Eugen Borcoci, University "Politehnica" of Bucharest (UPB), Romania
Carlos Becker Westphall, Federal University of Santa Catarina, Brazil
Mary Luz Mouronte López, Universidad Francisco de Vitoria - Madrid, Spain
Alex Sim, Lawrence Berkeley National Laboratory, USA
Jeff Sedayao, Intel Corporation, USA
Ivan Ganchev, University of Limerick, Ireland / Plovdiv University "Paisii Hilendarski", Bulgaria
Juraj Giertl, Deutsche Telekom IT Solutions, Slovakia

ICNS 2021 Industry/Research Advisory Committee
Steffen Fries, Siemens, Germany
Sathiamoorthy Manoharan, University of Auckland, New Zealand
Massimo Villari, Universita' di Messina, Italy
Éric Renault, Institut Mines-Télécom - Télécom SudParis, France
Young-Joo Suh, POSTECH (Pohang University of Science and Technology), Korea
Rui L.A. Aguiar, University of Aveiro, Portugal

ICNS 2021 Publicity Chairs
Daniel Basterretxea, Universitat Politecnica de Valencia, Spain
Marta Botella-Campos, Universitat Politecnica de Valencia, Spain

ICNS 2021

ICNS 2021 Steering Committee

Eugen Borcoci, University "Politehnica" of Bucharest (UPB), Romania
Carlos Becker Westphall, Federal University of Santa Catarina, Brazil
Mary Luz Mouronte López, Universidad Francisco de Vitoria - Madrid, Spain
Alex Sim, Lawrence Berkeley National Laboratory, USA
Jeff Sedayao, Intel Corporation, USA
Ivan Ganchev, University of Limerick, Ireland / Plovdiv University "Paisii Hilendarski", Bulgaria
Juraj Giertl, Deutsche Telekom IT Solutions, Slovakia

ICNS 2021 Industry/Research Advisory Committee

Steffen Fries, Siemens, Germany
Sathiamoorthy Manoharan, University of Auckland, New Zealand
Massimo Villari, Universita' di Messina, Italy
Éric Renault, Institut Mines-Télécom - Télécom SudParis, France
Young-Joo Suh, POSTECH (Pohang University of Science and Technology), Korea
Rui L.A. Aguiar, University of Aveiro, Portugal

ICNS 2021 Publicity Chairs

Daniel Basterretxea, Universitat Politecnica de Valencia, Spain
Marta Botella-Campos, Universitat Politecnica de Valencia, Spain

ICNS 2021 Technical Program Committee

Abdelhafid Abouaissa, University of Haute-Alsace, France
Fatemah Alharbi, University of California, Riverside, USA / Taibah University, Yanbu, Saudi Arabia
Sadiq Ali, University of Engineering and Technology, Peshawar, Pakistan
Adel Alshamrani, University of Jeddah, Saudi Arabia
Delaram Amiri, University of California Irvine, USA
Patrick Appiah-Kubi, University of Maryland University College, USA
Michael Atighetchi, Raytheon BBN Technologies, USA
F. Mzee Awuor, Kisii University, Kenya
Muhammed Ali Aydin, Istanbul University - Cerrahpaşa, Turkey
Bharath Balasubramanian, ATT Labs Research, USA
Mohammad M. Banat, Jordan University of Science and Technology, Jordan
Ilija Basicevic, University of Novi Sad, Serbia
Imen Ben Lahmar, University of Sfax, Tunisia
Samaresh Bera, IISc Bangalore, India
Robert Bestak, Czech Technical University in Prague, Czech Republic
Hasan Burhan Beytur, Middle East Technical University, Turkey
Eugen Borcoci, University "Politehnica" of Bucharest (UPB), Romania
Fernando Boronat Seguí, Universidad Politécnica De Valencia-Campus De Gandia, Spain

Vasco N. G. J. Soares, Instituto de Telecomunicações / Instituto Politécnico de Castelo Branco, Portugal

Rute Sofia, fortiss GmbH, Germany

Samy S. Soliman, University of Science and technology - Zewail City of Science and Technology, Egypt

Junggab Son, Kennesaw State University (Marietta Campus), USA

Mhd Tahssin Altabbaa, Istanbul Gelisim University, Turkey

Fengxiao Tang, Tohoku University, Japan

Yoshiaki Taniguchi, Kindai University, Japan

Luis Tello-Oquendo, Universidad Nacional de Chimborazo, Ecuador

Yinglei Teng, Beijing University of Posts and Telecommunications, China

Giorgio Terracina, Università della Calabria, Italy

Serpil Üstebay, İstanbul Medeniyet University, Turkey

K. Vasudevan, IIT Kanpur, India

Ferdinand von Tüllenburg, Salzburg Research Forschungsgesellschaft, Austria

Kefei Wang, Louisiana State University, USA

Cong-Cong Xing, Nicholls State University, USA

Anjulata Yadav, Shri G.S. Institution of Technology and Science, Indore, India

Anna Zatwarnicka, Opole University of Technology, Poland

Justin Zhan, University of Arkansas | College of Medicine - University of Arkansas for Medical Sciences, USA

Qi Zhao, UCLA, USA

Tao Zheng, Orange Labs China, China

Fuhui Zhou, Nanjing University of Aeronautics Astronautics, China

Ye Zhu, Cleveland State University, USA

Galina A. Zverkina, V. A. Trapeznikov Institute of Control Sciences of Russian Academy of Sciences (ICS RAS), Moscow, Russia

Copyright Information

Table of Contents

Comparison of Performance in Weed Detection with Aerial RGB and Thermal Images Gathered at Different Height

Jose F. Marin[1], David Mostaza-Colado[2], Lorena Parra[2, 3], Salima Yousfi[2], Pedro V. Mauri[2], and Jaime Lloret [3]

[1] *Area verde MG Projects SL. C/ Oña, 43 28933 Madrid*, Spain

[2]Instituto Madrileño de Investigación y Desarrollo Rural, Agrario y Alimentario (IMIDRA), Finca "El Encin", A-2, Km 38, 2, 28800 Alcalá de Henares, Madrid, Spain

[3] Instituto de Investigación para la Gestión Integrada de Zonas Costeras Universitat Politècnica de València, Valencia, Spain

Email: jmarin@areaverde.es, david.mostaza@madrid.org, loparbo@doctor.upv.es, salima.yousfi@madrid.org, pedro.mauri@madrid.org, jlloret@dcom.upv.es

Abstract— **Weed detection is a crucial aspect of reducing the usage of phytosanitary products. Most studies about weed detection have been performed with linear crops; few studies can be found in crops with high soil coverage. In this paper, we have evaluated the effect of drone flying height on wild species detection. We have gathered images in a golf course from 4 to 16 m above ground. A non-professional drone with a camera with 1.5 megapixels was used to gather the pictures. The images are composed of red, green, and blue bands. Images were gathered in three zones with a very high infestation, high infestation, and low infestation of *Daucus carota*. To evaluate the effect of flying height, we calculate the percentage of the affected area and compare the obtained rates for different height, assuming that the rate at 4 m is 100% of detection. To determine is a pixel represent the wild plant or the grass, a vegetation index is used. Our results indicate that the error in estimating the affected area is relatively low, from 8 to 10 m; in some cases, overestimation errors are detected. Nonetheless, the relative error beyond 12 m reaches up to 25% of relative error. In these cases, the error consists of an underestimation of the presence of a wild plant.**

Keywords-image processing; drone; turfgrass; green areas; vegetation indexes; wild plants.

I. INTRODUCTION

The green areas are special agroecosystems characterized by the cultivation of a single species, grasses, to maintain a green cover in cities. Several authors pointed out the importance of green areas in cities and their potential benefits for air quality, quality of life of citizens, and enhancing social cohesion [1].

One of the requirements for the green areas is having a homogenous coverage with a low or null incidence of wild plants. This is especially important in green areas intended for recreational purposes. To stop the proliferation of weed plants, periodic mowing and phytosanitary products can be applied. Nonetheless, considering the global efforts to reduce pesticide applications and the particular scenario for green areas, it is essential to minimize the application of phytosanitary.

One of the best ways to reduce the amount of used product is to develop tools for early detection [2]. Thus, the infected area in which products must be applied is small, and a reduced amount of phytosanitary product is used. The use of image processing techniques acquired by different means has become essential in agriculture to identify the proliferation of pest, diseases and wild plants. Nevertheless, using these tools in green areas is reduced since most techniques cannot be directly applied due to the vegetation patterns. While in most cropping systems, the crops are schemed as lines, and the proliferation of green biomass outside that lines can be considered a wild plan, in green areas, there are no lines. Instead, the grass covers all the ground, and the wild plans might appear interspersed with the grasses.

Most of the tools developed for agriculture are based on this linear scheme and the recognition through artificial intelligence of the wild plants. Nonetheless, this requires internet access, and the data cannot be processed in real-time in most cases. On the other hand, some indexes have been developed based on combining the Red-Green-Blue (RGB) components of an image. Initially, those are the most used components since not all drones incorporate thermal images. Moreover, in several cases, the optimal combination of RGB can be used to differentiate between the crop and the wild plants. Although those indexes are not as accurate as artificial intelligence, they can be applied in real-time and in scenarios without internet access. Moreover, this methodology can be used with the appropriate adaptations for other similar crops such as cereals or pastures.

In recent papers, we have established different indexes, based on bands combinations, to determine the presence or absence of wild plants in a green area [3]. Another option is to use the edge detection technique to identify the wild plants [4]. Nevertheless, both techniques have been applied only with images gathered at low height and good spatial resolution. As far as we know, no tests have been done to determine the maximum flying height possible for gathering data with commercial drones. Even that the professional drones might have cameras with better spatial resolution, fixing an average limitation for commonly-used drones with regular cameras is needed. Once we identify the maximum flying height, it will be possible to estimate the required time to monitor an area.

In this paper, we analyze the possibility of detecting wild plan in a green area using images gathered with Bebop 2 Pro drone at a flying height of 4 m to 16 m. We use pictures gathered in an area with the presence of *Daucus carota* L., a wild plant. The band combination is the technique used to determine the weed plant presence. First, we will evaluate the incidence of the wild plant as the percentage of pixels defined as a wild plant in a rectangular area. Then, we will compare the incidence in three areas, with diverse levels of incidence, at different flying heights to determine the maximum height that can be used for monitoring purposes.

The rest of the paper is structured as follows; Section 2 outlines the related work. The materials and methods are described in Section 3. Section 4 analyzes the results, highlighting the implications of the flying height. Finally, conclusions and future work are summarized in conclusion.

II. RELATED WORK

In this section, we are going to summarize the existing efforts for detecting wild species and the different options for grass monitoring with drones.

First of all, we differentiate the options for remote sensing. According to Huang et al. [5], we can divide the remote sensing into four systems attending to the distance from the ground and the used equipment. Images gathered at least 5 m height are usually collected by ground-based systems and considered proximal remote sensing. Images gathered with drones are collected between 10 and 200 m. Each method has each own characteristics, restrictions and limitations. In our paper, we are using a drone, but according to the flying height, we are in-between both systems described by Huang et al.

In [6], Hassanein and El-Sheimy used an Inspire 1 drone from DJI with an X3 RGB camera to determine the presence of wild species in crops (canola and bean). Authors shave selected as flying height 20, 40, 80, and 120 m. Their methodology consists of segmenting the image and generate vegetation indexes for each segment. Then, they apply a threshold to determine if in this grid there are wild plants or not. Their methodology offered good results at high height (80 and 120 m). Nonetheless, the authors do not provide the used threshold or equations for detecting the wild plants in their paper. The employed camera has a higher resolution than our camera (they used a professional drone). Moreover, they do not indicate the size of the wild plant sports detected. In this case, their methodology can be applied in a large area where a high proliferation of wild plants is expected.

Barrero and Perdomo proposed image fusion for gramineous detection in rice fields in [7]. They combine two cameras for obtaining images and fuse the data. The first camera was an RGB camera with 12.1 megapixels; the second one was a multispectral camera with 1.2 megapixels. Their methodology, fuse data using neural networks, was efficient with images gathered at 60 and 70 m. Although authors have proven their methodology at a higher height than us, they have better cameras and professional drones. In our case, the drone and camera stability are not as accurate as in their case since their drone has a gimbal. In addition, our camera has 1.5 megapixels for RGB image.

The effect of pixel size, which directly relates to flying height, over the accuracy of wild species detection was studied by Tamouridou et al. in [8]. Authors used machine learning to determine the presence or absence of wild plants in an abandoned field, previously used for cereals cropping. First, the authors applied the Maximum Likelihood classifier. Their images had a pixel size of 0.1 m. Next, they study the effect of reducing the pixel size on accuracy. Their results indicate that similar accuracy is found for the pixel size of 0.1 to 1.5 m. Still, a substantial reduction in the accuracy is found for 2 m (the largest evaluated pixel size).

Another study, presented by Zou et al. [9], shows the accuracy of wild species detection in crops. The authors used a DJI, MAVIC 2. They have an image of the pixel size of 5 mm obtained with a flying height of 20m. The authors obtained good accuracies by combining different artificial intelligence techniques. In our case, the acquired images have a pixel size of 3mm (at a flying height of 4 m) to 8.5 mm (at a flying height of 16 m).

As far as we know, no paper has evaluated the effect of incrementing the flying height using non-professional drones in green areas. Most studies are developed for linear crops using professional drones, heavier gimbal, and higher spatial resolution.

III. MATERIALS AND METHODS

In this section, we are going to detail the procedure followed for gathering and processing the data, as well as the employed hardware and software to obtain the results.

A. Data gathering process

In order to test the effect of flying height on the quantification of infection by wild plants, images of grass were gathered in a golf course. The photos were taken in one of the green areas, which was suffering from an infection of *Daucus carota* L., one of the common wild plants. The green was composed of *Agrostis stolonifera* L. T1, mowed periodically at 3.8mm. A picture of the data gathering process can be seen in Figure 1 (a).

(a) (b) (c) (d)
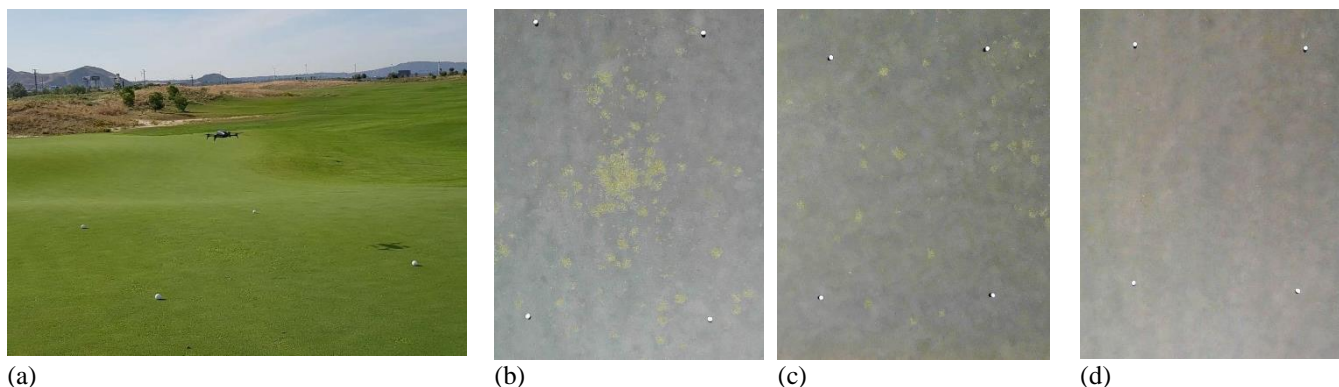
Figure 1. Images of the data gathering process, (a) picture taken during the data gathering, (b) to (d) data gathered for each studied area.

Along the same green, three study areas were delimited according to different incidence levels of the wild plant. To delimit the areas, four golf balls were used to define the 4 vertexes of a polygon. The three areas were described as "Very High Incidence", see Figure 1 (b); "High Incidence", see Figure 1 (c); and "Low Incidence" see Figure 1 (d).

The area delimited by the four balls has an average surface of 3x7 m. Images were gathered at 5 different flying heights, from 4 m to 16m height. In Figure 1 (b) to 1 (d), we show the data gathered at 4 m height. All the images were collected on the same morning and with the same meteorological conditions. The data gathering process had a duration of less than 1 h

B. Drone and image characteristics

To gather the data, we have selected a commercial drone with typical characteristics. The chosen drone is the Parrot Bebop 2 Pro [10]. It has a flying autonomy of 20 min and a weight of 504 g. In addition, it has a peak velocity of 60 km/h and four helixes.

The drone has two different cameras. One of them has a fixed position, and the second one can be moved. For these tests, we need to use the zenith pictures to use the second camera. It is essential to consider that for this drone, and this is the camera with lower resolution. The gathered images have 1080x1440 pixels and 24-bit colour.

C. Image processing

To process the image, specific software (generally used for remote sensing) is used. We have selected ArcGIS 10.5 for its versatility. Once the photos are included in the ArcMap, from ArcGIS software [11], they are converted into 8-bit colour images to simplify the operations.

First of all, a vegetation index based on RGB data can differentiate pixels with grass from pixes with the wild plant. The vegetation index is a linear combination of the two or more bands of the picture, which produce different values according to the presence or absence of wild plant; more information can be found in [3]. In past papers [3], we have developed vegetation indexes. Nonetheless, those indexes were used for mixed lawns composed of two or more grass species. In this case, as we have a single grass species, we will try to simplify the existing indexes. After calculating the vegetation index, the threshold to differentiate the type of cover is determined. Then, the image is reclassified [12], the pixels without wild plant are classified as 0, and the pixels which values indicate the presence of wild plant are classified as 1.

Following, for each image, we generate a vectorial layer formed by a polygon that delimits the studied area. As the flying height increases, the size of the polygon (in pixels) decreases. To define the polygon, the inner extreme of each one of the balls is used.

Once the image is classified as "Infected Pixel=0" and "No Infected Pixel=1", the tool Zonal Statistic as a Table [13] is used to obtain the summary of data in each studied area. The most critical data are the summation, the mean, and the standard deviation from the statistics. The statistics summary of each polygon is exported to Excel. Finally, in Excel, some other parameters are calculated. The % of affection is calculated using the total number of pixels in the studied area and the number of pixels with values = 1 (obtained through the summation).

We consider that the data gathered at 4 m is the most accurate one. Thus, we consider that this data has no error in their results. This is 100% of detection. The percentages of detection obtained at other height are compared to identify maximum height that offers accurate values.

IV. RESULTS

In this section, we are going to analyze the obtained data. First, we will see if previously used indexes might be used for this case or if indexes can be simplified in order to accelerate the calculations. Secondly, we compare the results in terms of accuracy at different heights.

A. Obtention of vegetation index

We have considered the two indexes presented in [3]. Among the proposed indexes, the first is the one that detects the wild plant. A modification of this index is proposed for this paper. The new index is defined in (1). The soil removal coefficient is removed from the index, and the mathematic operations have been modified.

$$Vegetation\ Index = B1+B2-B3 \qquad (1)$$

where B1 is the red band, B2 is the green band, and B3 is the blue band.

Theoretically, the index can have values from -256 to 512. Nonetheless, the found values go from -29 to 260. After analyzing the vegetation index values of the 15 evaluated images, we have established the threshold as 190. While values higher than 190 are defined as will plant, the values lower equal or lower than 189 are defined as grass. This is a significant improvement concerning the previous indexes, in which the definition of wild plant or grass is based on natural breaks (or Jenks), and no fixed value can be used.

In Figure 2, we can see the results of applying the index to the images gathered at 4 m in all the studied areas. We can see for each studied area the RGB picture, the results after applying the index, and the classified raster once the threshold is applied. The polygon that defines the studied area is visible for index images to facilitate the interpretation of results.

We have compared the results of applying this index with the index defined in [3], and the results are similar. Thus, we keep with the index of (1).

B. Comparison of incidence of wild species at different height

This subsection will analyze the differences in the obtained incidence of images gathered at a different height. First of all, we include a short summary of the statistical information obtained for each image in Table II. The Zones are identified by the Id: 1 = Very High Infestation, 2 = High Infestation, and 1 = Low infestation. The height indicates the flying height at which the picture is obtained. The area and sum are the numbers of pixels of the studied area and the number of pixels classified as a wild plant. Those are the

values used to calculate the % of the affected area. Finally, the Mean and the Standard Deviation (STD) indicate the variability of data in the studied areas. If there is no effect of flying height on a wild plant mean and STD detection, each zone should be similar. Nonetheless, we can see that the values decrease as the height increase. Therefore, we can affirm that there is an effect of flying height over the wild species detection.

In order to identify the maximum flying height, we are going to consider not only the mean and the STD but also the error in the estimated affected area. For that purpose, we are going to compare the estimated affected area with each one of the images. Figure 2 shows the calculated affected area according to the number of pixels of the studied area and the number of pixels classified as a wild plant. We can see that the zones with Very High Infestation are the ones with a higher % of the affected area (3.66% to 2.04% from 4 to 16m). The zone with High Infestation has an affected area of 0.39 % to 0.12 %, and the Zone with Low Infestation from 0.05% to 0%.

TABLE I.   REPRESENTATION OF RGB PICTURE, THE INDEX AND THE CLASSIFIED RESULT
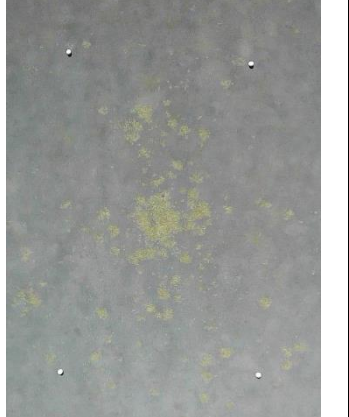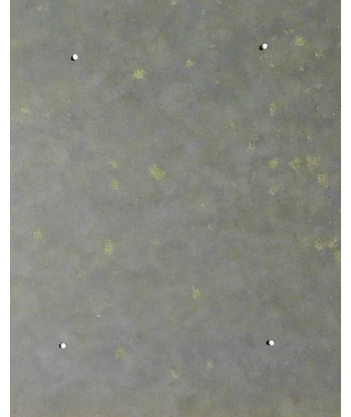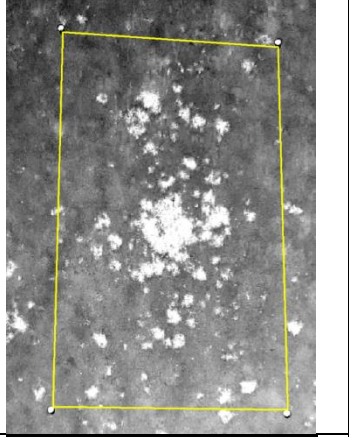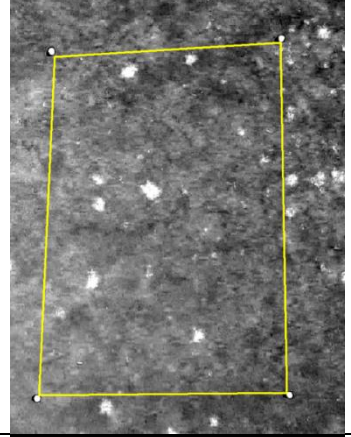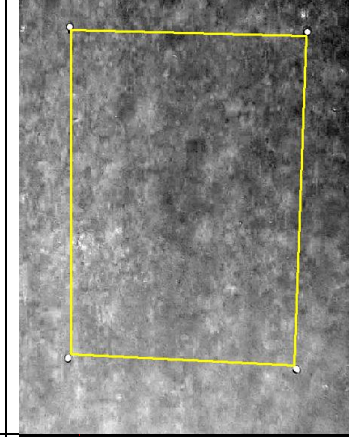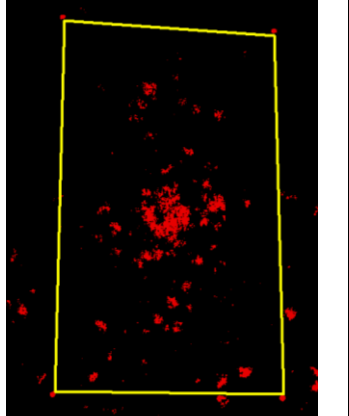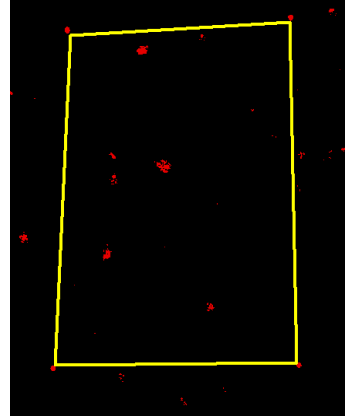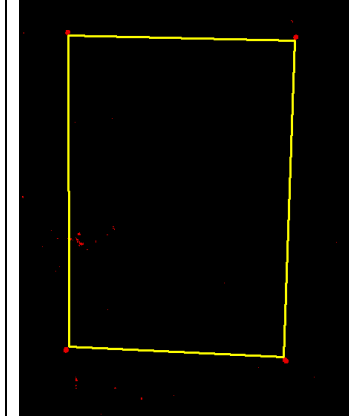
TABLE II.   SUMMARY OF OBTAINED INFORMATION OF EACH AREA

Zone (Id)	Height (m)	Area	Wild plant	Mean	STD
		(number of pixels)		*(pixel value)*	
1	4	326956	11953	0.036558	0.187675
1	8	178129	6585	0.036968	0.188682
1	10	124936	4135	0.033097	0.17889
1	12	47070	1251	0.026577	0.160845
1	16	29356	601	0.020473	0.141611
2	4	245417	958	0.003904	0.062356
2	8	127101	740	0.005822	0.076081
2	10	67318	339	0.005036	0.070784
2	12	35319	101	0.00286	0.053399
2	16	19955	25	0.001253	0.035373
3	4	266248	137	0.000515	0.022678
3	8	147082	31	0.000211	0.014516
3	10	89412	9	0.000101	0.010032
3	12	35570	5	0.000141	0.011855
3	16	20203	0	0	0

Comparing the percentages at different heights, the data gathered at 4 and 8 m offer almost identical data in Zone 1, while the calculated areas at 10m are slightly lower. For Zones 1 and 2, the percentage increase in some cases at 8 and 10 m due to the increment of size pixel and the reduced number of pixels that contain wild species. This is a common effect when the flying height increase and the number of interesting pixels (pixels classified as a wild plant) are low. This effect was not found in Zone 3.

We consider the Absolute Error (AE) in our estimations, assuming that the results of the image obtained at 4 m represents 100% of the affected area. Thus, we calculate the AE of each image having the % of affected areas at 4 m as a reference. The more evident results can be seen for Zone 1 (Very High Infestation); in this case, the AE is almost null for 8 m (-0.04%). The AE reaches 0.34, 0.99, and 1.6 1 % the 10, 12, and 16 m. For the other areas, the errors are much lower since the affected areas are smaller.

In Relative Error, see Figure 3, the errors can be compared among areas. Those errors with positive value indicate an overestimation of the infestation; meanwhile, errors with negative value indicate an underestimation. As detailed before, For Zones 1 and 2, there are some points, with low height, with an overestimation of the incidence. Nonetheless, after 12 m, in all the cases, there is an underestimation. Note that the error at 12 m is almost the same for Very High Infestation (-27.3%) and High Infestation (-26.7%). It is important to remark that with Low Incidence, there is no overestimation.

Considering the negative effect of underestimation in the proliferation of wild species and the delay of phytosanitary products application, we consider that 10 m should be the established threshold for monitoring with this sort of drones.

C. Limitations of proposed technic and implications of established threshold

In this section, we are going to analyze the limitations of our study and the implications of the established threshold for the flying height.

First of all, there is a bias in our tests given the used drone. Each camera has a different resolution parameter, which affects the resolution of the obtained pictures. Moreover, the

fact of having the image in 8-bit to simplify the analyses affect the accuracy of our results. Nonetheless, these biases can be assumed since the specialized drones with cameras with high resolution (in terms of pixels) still have a high cost, and their weight can be a limiting factor according to the national or regional regulations. Moreover, cameras with higher resolution are used with professional drones, with a higher cost (almost 10 times more), which the enterprises cannot readily assume. The 8-bit constriction has an effect on the accuracy of the proposed vegetation index, but this is necessary if we want to keep the image processing in real-time or nearly real-time.

It is essential to consider that this threshold, established for cameras with similar resolution than the used one, might be helpful in different wild species. Nonetheless, the threshold must be re-evaluated to detect grass diseases such as *Fusarium* or Dollar spot. The main reason is that the affected areas by the diseases are smaller than with wild species.

Finally, we are going to analyze the impact over the flying time of modifying the threshold between 8, 10 and 12 m. The maximum covered areas with these flying thresholds are 80x60 m for 4m high, 88x65m for 10 m high, and 96x70m for 12 m high. The variation in the flying height increases a 20% and 40% (for 10 and 12 m, respectively). Considering the time required to fly over an area of 60x80 m, the drone will need 20 min at 8 m, 17.5 min at 10 m, and 15 min at 12 m. This increment in the required time to cover a small area must be scaled when an entire golf course or green areas in cities must be evaluated. Thus, we are going to indicate the required time to cover different interesting and well-known areas for the different flying height (8 to 12 m). For example, in a golf course type Regulation Course with turfgrass areas from 350,000 m^2, the required flying time will be 24.30, 21.26, and 18.23hours. For golf course type Par 35 or 36 with a Standard combination (average turfgrass surface of 120,000 m^2, the required flying time will be 8.33, 7.29, and 6.25 hours. For other sports such as polo, which fields have an average surface of 40,134 m2, the time required is 2.7, 2.4, and 2 hours. For soccer or rugby fields, an average surface of 10,800 m^2, the time of flying needed will be 45, 39.37, 33.75 minutes. In the case of the hockey field, an average of 5,027 m^2, the flying time will be 21, 18.3, 15.7 minutes. Finally, for a tennis court, an average extension of 195 m2, less than 1 minute is required regardless of the flying height.
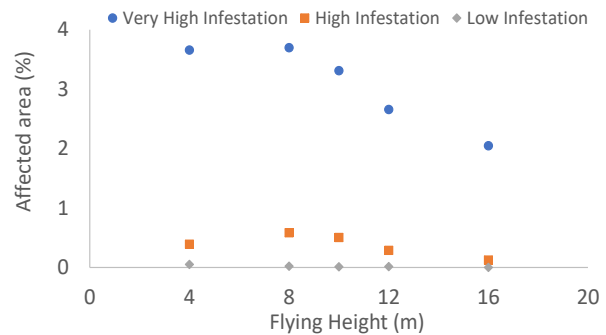
Figure 2.   Comparison of estimated affected areas at each height
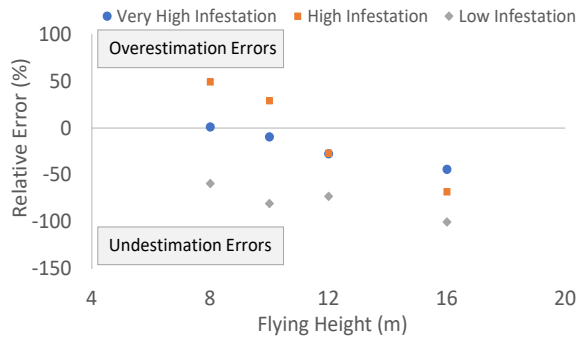
Figure 3.   Relative Error of estimated affected area

The other advantage of our proposed method is that controlling the infected areas with pictures will reduce the possible overestimation by the workers and reduce the consumed time. Currently, workers, particularly in green areas with high requirements, have to walk through the area periodically, searching for the apparition of diseases or wild plants.

V.   CONCLUSION AND FUTURE WORK

In this paper, we have studied the effect of flying height on detecting the infestation of grass with a wild plant (*Daucus carota)*. This is especially relevant in the management of green areas since a fast detection will save phytosanitary products, reducing the maintenance cost and increasing its sustainability.

We need to find a balance between spatial resolution (low flying height had high resolutions) and flying time vs. covered area (high flying height had better relation) in selecting the flying height. We have evaluated the error in determining the percentage of infestation in a green area for different flying heights. Our results indicate that 10 m should be the maximum height given the characteristics of our camera.

In future work, we will include thermal images to evaluate if having a combination of four bands allows having a better index with which we can have a higher threshold for the flying height. Regarding the index, we will work on its standardization for different undesired species in order to simplify the process in the future. In addition, we will compare the flying height for images captures with professional drones. If possible, we will compare the recommended threshold for wild species with a threshold for disease.

ACKNOWLEDGMENT

REFERENCES

[1] D. D'Alessandro, et al., "Green areas and public health: improving wellbeing and physical activity in the urban context". Epidemiol Prev, 2015, 39(4), pp. 8-13.

[2] L. Parra, et al., "Edge detection for weed recognition in lawns. Computers and Electronics in Agriculture", 2020, 176, pp.105684.

[3] L. Parra, V. Torices, J. Marín, P.V. Mauri, and J. Lloret, "The Use of Image Processing Techniques for Detection of Weed in Lawns". In Proccedings of the Fourteenth International Conference on Systems (ICONS 2019), Valencia, Spain, 2019, pp. 24-28.

[4] L. Parra, et al., "Comparison of Single Image Processing Techniques and Their Combination for Detection of Weed in Lawns". International Journal On Advances in Intelligent Systems, 12 (3 and 4), 2019, pp. 177-190.

[5] Y. Huang, K. N. Reddy, R. S. Fletcher, and D. Pennington, "UAV low-altitude remote sensing for precision weed management". Weed technology, 32(1), 2018, pp. 2-6.

[6] M. Hassanein and N. El-Sheimy, "An Efficient Weed Detection Procedure Using Low-Cost UAV Imagery System for Precision Agriculture Applications". International Archives of the Photogrammetry, Remote Sensing & Spatial Information Sciences, 2018, pp. 1-7.

[7] O. Barrero and S. A. Perdomo, "RGB and multispectral UAV image fusion for Gramineae weed detection in rice fields". Precision Agriculture, 19(5), 2018, pp.809-822.

[8] A. A. Tamouridou, et al., "Evaluation of UAV imagery for mapping Silybum marianum weed patches". International journal of remote sensing, 38(8-10), 2017, pp. 2246-2259.

[9] K. Zou, X. Chen, F. Zhang, H. Zhou, and C. Zhang, "A Field Weed Density Evaluation Method Based on UAV Imaging and Modified U-Net". Remote Sensing, 13(2), 2021, pp. 310.

[10] Specifications of Prarrot BeBop 2 Pro. Available at: https://s.eet.eu/icmedia/mmo_35935326_1491991400_5839_16054.pdf. Last access in 16/04/2021.

[11] Webpage of ArcGIS software. Available at: https://desktop.arcgis.com/en/. Last access in 16/04/2021

[12] Description of Reclassify Tool. Available at: https://desktop.arcgis.com/en/arcmap/10.3/tools/spatial-analyst-toolbox/reclassify.htm. Last access in: 16/04/2021

[13] Description of Zonal Statistic as Table Tool. Available at: https://desktop.arcgis.com/en/arcmap/latest/tools/spatial-analyst-toolbox/zonal-statistics-as-table.htm. Last access in: 16/04/2021

Evaluation of Temporal Stability of Dissolved Oxygen Conditions in a Small-Scale Phytodepuration System

Barbara Stefanutti[1], Celia Cano[2], Jose Plaza[2], Lorena Parra [2, 3], Pedro V. Mauri[2]

[1] Universidad de Alcalá de Henares, Plaza de San Diego, s/n, 28801 Alcalá de Henares, Madrid

[2]Instituto Madrileño de Investigación y Desarrollo Rural, Agrario y Alimentario (IMIDRA), Finca "El Encin", A-2, Km 38, 2, 28800 Alcalá de Henares, Madrid, Spain

[3] Instituto de Investigación para la Gestión Integrada de Zonas Costeras Universitat Politècnica de València, Valencia, Spain

Email: barbara.stefanutti@edu.uah.es, celia.cano.shaw@madrid.org , joseplaza2512@gmail.com , loparbo@doctor.upv.es, pedro.mauri@madrid.org

Abstract— **Water regeneration is a top priority to achieve sustainability. Different alternatives to the traditional wastewater treatments that combine nitrification-anammox-denitrification are becoming popular in the last few years. These systems combine bacteria and plants to remove the organic matter and generate harvestable biomass. Despite the importance of oxygen concentration for the degradation of organic matter, no studies analyse the variation of dissolved oxygen in those systems. In this paper, we are going to evaluate the temporal and spatial variability of dissolved oxygen in the ponds of a phytodepuration system composed of *Typha domingensis* to identify if the bottom of the ponds is in anaerobic/anoxic conditions or not. Thus, the concentration of dissolved oxygen in 6 points and at 4 depth are measured during 2 months. Our results indicate that there is a high temporal variability of dissolved oxygen, caused mainly by the entrance of water into the system. The variability was much lower in the bottom of the third (and last) tank. The spatial distribution of the oxygen in normal conditions follows a gradient, having the highest concentration (0.5 mg/L) on the surface of the first pond and the lower concentration at the bottom of the second and third ponds ($\approx$0.1 mg/L). Finally, we relate the system's performance with the produced biomass, 1.8 kg/m^2, and the reduction of total dissolved solids, 80%.**

Keywords-Typha domingensis; spatial variability; anaerobic conditions; wastewater; crops

I. INTRODUCTION

The wastewater treatment is an urgent need to accomplish the Sustainable Development Goals and have clean waters. The regenerated waters can be a valuable resource for agriculture since they can be used to irrigate crops. In recent years, the use of regenerated water has increased, and the apparition of alternative systems, such as the phytodepuration, are becoming popular [1]. The phytodepuration consists of the combined use of bacteria and plants to regenerate the water in ponds.

The operation principle of phytodepuration is that different bacteria in the water under anaerobic and aerobiotic conditions are capable of transforming the organic matter into nutrients through the combination of nitrification-anammox-denitrification processes [2]. This process is facilitated thanks to the introduction of small amounts of oxygen in the water by the plants through their roots. On the other hand, the plants consume the excess of nutrients in the water. Thus, the water quality is improved as the plant grows

by absorbing these nutrients. The excess of nutrients and organic matter might cause environmental damages in rivers and lakes, known as eutrophication. Moreover, the phytodepuration systems do not produce any sewage sludge.

Recently, a research project to evaluate the use of small-scale phytodepuration to regenerate the wastewater of a small region is started. A phytodepuration system based on three ponds was set up. In this paper, we want to evaluate the variability of Dissolved Oxygen (DO) concentration along the ponds. First of all, we want to assess the generated vertical gradient of DO from the surface to the bottom. The plants inject oxygen into the water in the radicular area and while the bacteria are consuming this DO. On the other hand, and considering that the system will not work as a stationary system with a fixed and determined flow, we have to evaluate if this operation principle is functional. The system is injecting wastewater into the phytodepuration according to the water level of the reception tank.

This phytodepuration system aims to combine the regeneration of wastewater with the cropping of vegetals which can be later used for different purposes. This method is very convenient for rural areas with small villages and agroindustry, which produce wastewater with very high organic matter levels. Furthermore, the phytodepuration might involve a new source of income by harvesting the cropped plants for the rural population. Specifically, in our system, we have southern cattails as a crop. It has several applications, mainly as livestock feed [3]. Even so, recent research has proved their use for bioenergy production [4].

Although several authors pointed out the relevance of DO in converting organic matter into nutrients, no one paper shows the evaluation of its variability (temporal nor spatial) and its range in those systems. The inclusion of sensing technologies, or at least periodic monitorisation with probes, must be considered to evaluate the system's performance. Despite the importance of monitorisation in agriculture, where we find several monitoring systems [5], the monitorisation of phytodepuration is still in an early development stage.

In this paper, we analyse the variability of DO in our system. We will evaluate its temporal and spatial variability for 6 measuring points (at the entrance and exit of each pond) and 4 different depth per point (from the surface to the bottom). We will compare the stability of conditions in each pond for two months to define if they are reaching nearly anoxic conditions, which are required in the bottom of the

ponds. A commercial optical probe was used to measure the DO. Data was gathered, as average, once per week. Thus, we will present the harvested biomass, which is growing over the water and injecting oxygen at the end of the study, in kg and kg/m^2. Furthermore, the rate of total dissolved solids removal is given.

The rest of the paper is structured as follows; Section 2 outlines the related work. Section 3 describes the materials and methods. The obtained results are analysed in Section 4, highlighting the implications of DO on the system's performance. Finally, Section 5 summarises the conclusions and future work.

II. RELATED WORK

In this section, we are going to summarise the studied DO characteristics in phytodepuration and similar processes.

In [6], Borges et al. studied the variability of several parameters on constructed wetland system to treat water from the Corumbataí River. Their system consists of 4 reactors on continuous water flow. The water input is the river which is considered reactor 1. In reactor 2, they have macrophytes (*Eichhornia crassipes* (Mart.) Solms), covering 80% of the water surface. Water was sampled at the end of each reactor. In their case, the initial DO level of water at the entrance of reactor 2 was 9 mg/L, and the DO after reactor 2 8.9 mg/L. Thus, they do not found any extra relevant oxygenation by the macrophytes (the water was fully oxygenated from the beginning). Their data indicates a reduction of total suspended solids of 54.5%. The authors also found an increase in the chemical demand of oxygen (CDO) of 26.7% after reactor 2.

Caselles-Osorio et al. [7] evaluated the modification of studied parameters on a horizontal subsurface-flow constructed wetland using *Cyperus articulatus* L. Authors pumped the wastewater from a septic tank to a set of 4 tanks, 2 of them with plants and the other 2 vertical perforated pipes. Their study had a duration of 3 months with a total of 43 measurements. The water exit from the septic tank with a DO concentration of 0.17 mg/L. The DO in the tanks with the plants reaches 2.1 ($\pm$1.2) mg/L. On the other hand, the tanks with the perforated pipes only went to 1.7($\pm$1.2) mg/L. After finishing the experiment, the harvested biomass was 5 kg/m2 in the tanks with plants.

García-Perez et al. in [8] evaluate the temporal variability of DO in a recirculating vertical flow constructed wetland. In their system, they pump the water from a septic tank. Their pond has 6 x 6 x 1.2 m. Gravel was added to cover 50% of the volume of the wetland. Thus, 25% of the wetland were uncovered. As plants for consuming the nutrients, the authors used maize. The authors measured the DO in 6 periods over the 220 days of the experiment. The water input had an average DO of 1.2 mg/L. Their results indicate that the wetland was in aerobic conditions with average values of 5.3 mg/L (maximum and minimum values of 7.1 and 34 mg/L). Nonetheless, the authors do not specify precisely where are the water samples were taken (surface or bottom).

A final example can be found in which Palta-Prado and Morales-Velasco used different Poaceae for domestic wastewater phytodepuration [9]. The authors pumped the wastewater from a reduced region into 4 treatments. The wastewater had an average DO of 5.67 mg/L. The different treatments consist of diverse plant species. Their results indicate that none of the treatments increased the DO values in water. Average DO values for each treatment were 5.5 to 5.16 mg/L. Thus, CDO was nearly halved in all the cases.

As far as we know, no one paper has analysed the distribution of DO in the phytodepuration system and their trend along with the system or depth. Furthermore, it has not been studied for constructed wetlands or natural wetlands used for remediation regardless of their soil/bottom characteristics. Thus, it is necessary to have a preliminary approximation before performing an exhaustive analysis or studying its variation when the flow is modified or before adding a more complex (polluted) water input.

III. MATERIALS AND METHODS

In this section, we are going to detail the characteristics of the phytodepuration system and the measuring process.

A. Description of the phytodepuration system.

The system has been built in "IMIDRA - El Encin" facilities at Alcalá de Henares (Spain). The phytodepuration system consists of an initial tank of 40 m^3. This tank has a coarse grating grid, acting as a primary decanter. The first tank receives the wastewater from the "El Encín" facilities, and it is estimated that 20% of the CDO is removed. Then, water reaches the rectangular ponds, which contain the floating plants. The phytodepuration system comprises three pools of 9.6 x 3.6 x 0.8 m each (27.6 m^3 per pool), with a volume of 83 m^3 (Figure 1). Based on previous experiences, a depth of the water layer of 80 cm has been established, considering a maximum root length of 50 cm. Thus, a lower zone of 25-30 cm remains for the decomposition of the sludge in which anoxic conditions are required.

B. Description of the phytodepuration system.

The concrete structure, consisting of three ponds, was finished in the middle of January of 2020, see Figure 2 (a). The selected plant was *Typha domingensis* Pers. An autochthonous plant is well adapted to eutrophic conditions and used widely for wastewater treatment [10][11]. The *T. domingensis* was located over floating plates. The floating plates have the function of keeping the plants on the water surface but also preventing the entrance of DO from the atmosphere to the water. Thus, it facilitates the generation of the required anoxic conditions for the bacteria in the bottom.
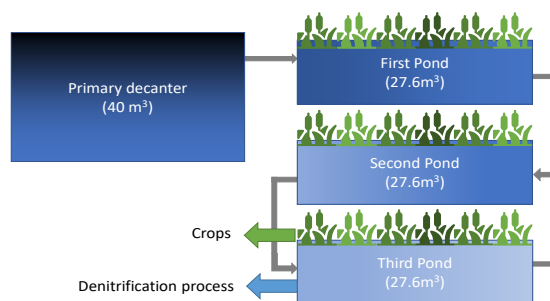
Figure 1. Scheme of phytodepuration system.

The placement of floating plates and plants began on 25/06/2020 (16 plants/m2). The *T. domingensis* came from the "Viveros Forestales La Dehesa SL", a specialised aquatic plant nursery for phytodepuration. The plants come from an alveolus tray, with a height of 15 cm in the aerial part and roots of 10 cm in length. They were kept in the shade under irrigation for seven days before their installation. Once the plant reached 1.67 m height and 35 cm root (02/09/2020), the study period starts. The studied period finished on 11/11/2020 when autumn tones began to appear, and the plants were harvested. Pictures of the different moments are shown in Figure 2. The dates of the photographs are Figure 2 (a) 18/05/2020, Figure 2 (b) 09/07/2020, and Figure 2 (c) 02/09/2020.

C. Measurement of DO in the ponds

Measurements of DO had been taken at two points per pond, one at the entrance and one at the exit of each pond. Thus, we have a total of 6 measurement points. In each point, DO was measured at four depth (6, 25, 50 and 75 cm). The measurements started on the water surface and finished at the bottom.

DO was measured with a probe HI98198 optical meter (HANNA [12]). The probe was calibrated with a 0 mg/L oxygen solution prior to data collection. For each measure, we wait until the value of DO is stabilised. A picture of the data gathering process and the probe is in Figure 2 (d).

IV. RESULTS

In this section, we analyse the variability of measured DO in the ponds. First of all, a general overview of the gathered data focusing on the temporal variations between points is shown. Then, the spatial variability along with the depth and the ponds is analysed. Following, we statistically analyze the data. Finally, we discuss the limitations of our study and the implication of the gathered data.

A. General overview of DO and its temporal distribution

The first step in order to analyse the variability of the DO is to have a general overview of the obtained values along the studied period. We can see the mean value of DO for each pond and each depth in Figure 3 (a) to (d). The different letters represent different depth from 6 cm to 75 cm, respectively. We can see that in general terms, the DO values are low. They never exceed the 2.6 mg/L. Although in some days, the DO increases, the detected increments are smaller for more profound points of the pond.

Concerning the temporal variability, we can identify mainly two peaks in the DO concentration. The first peak is found in the second measured day (7 days after starting the measurements). This peak increases the DO at all depth, but it only has an adverse effect (DO higher than 1mg/L) on the first pond. The second and third ponds have DO concentrations lower than 1 mg/L at all the depth. In fact, the DO values of the third pond are almost the same as in the previous measures. Meanwhile, in the second pond, we only found differences in the most superficial point. The second DO peak is found in two consecutive days, 41 and 49 days after starting the study. On day 43, the maximum DO concentration was found in the second pond with an average concentration of 1.44 mg/L at the most shallow depth. Meanwhile, the day 49, the DO concentration reached 2.47mg/L. On day 43, the second pond was the one with the higher concentration at all depth. Nonetheless, for day 49, the third pond had a higher concentration than the other at 50 and 75 cm depth. This trend might be explained by an accidental introduction of oxygen in the system at some moment before day 43.

B. Spatial distribution of DO in the ponds and their depth

After outlying the temporal distribution of DO concentration, we are going to focus on spatial variability. In Figure 4 (a) to (d), we represent the spatial distribution of the four measured points, entrance and exit of the first pond, and exit of the second and third pond, in the horizontal axis, and the four depth in the vertical axis. Figure 4 (a) to (c) displays the aspects of the ponds at different days, being Figure 4 (a), (b), and (d) the representation of normal distribution and Figure 4 (c) the spatial distribution in non-regular conditions. The different colours indicate the DO concentration (higher in blue tones and lower in green tones).

Focusing on the system's data in regular conditions, we can see how the DO decrease from the surface to the bottom of the pond and along with the ponds (from measured point 1 to 4). Comparing both days, the DO levels are higher in (a) than in (b) since that day there was a peak in the OD. Nonetheless, the spatial distribution is expected in the system. Figure 3 (c) shows that the aforementioned trend is not followed in unstable conditions.

(a)   (b)   (c)   (d)
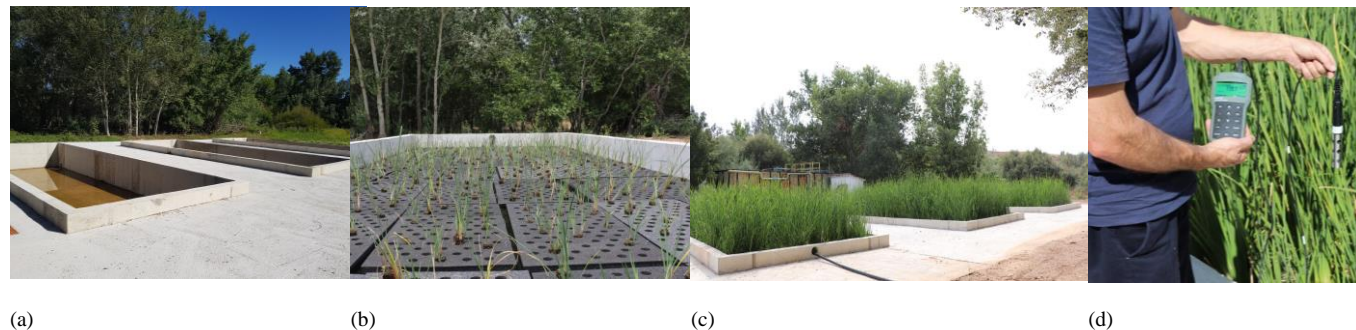
Figure 2.   Images of the phytodepuration system and the data gathering. Figure (a) shown the structure of the system Figures (b) and (c) show the growth of the crop in two months, and Figure (d) presents the used probe.
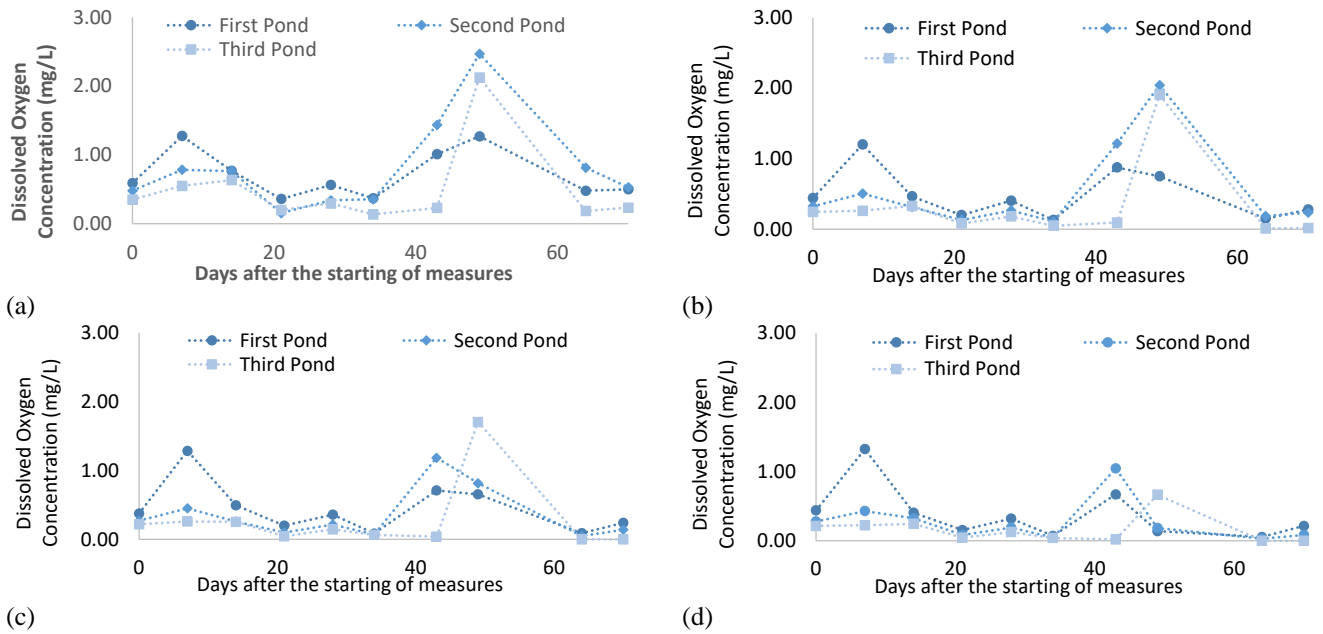
Figure 3. Overview of DO concentration at different depths (a) 6 cm, (b) 25 cm, (c) 50 cm, and (d) 75 cm.
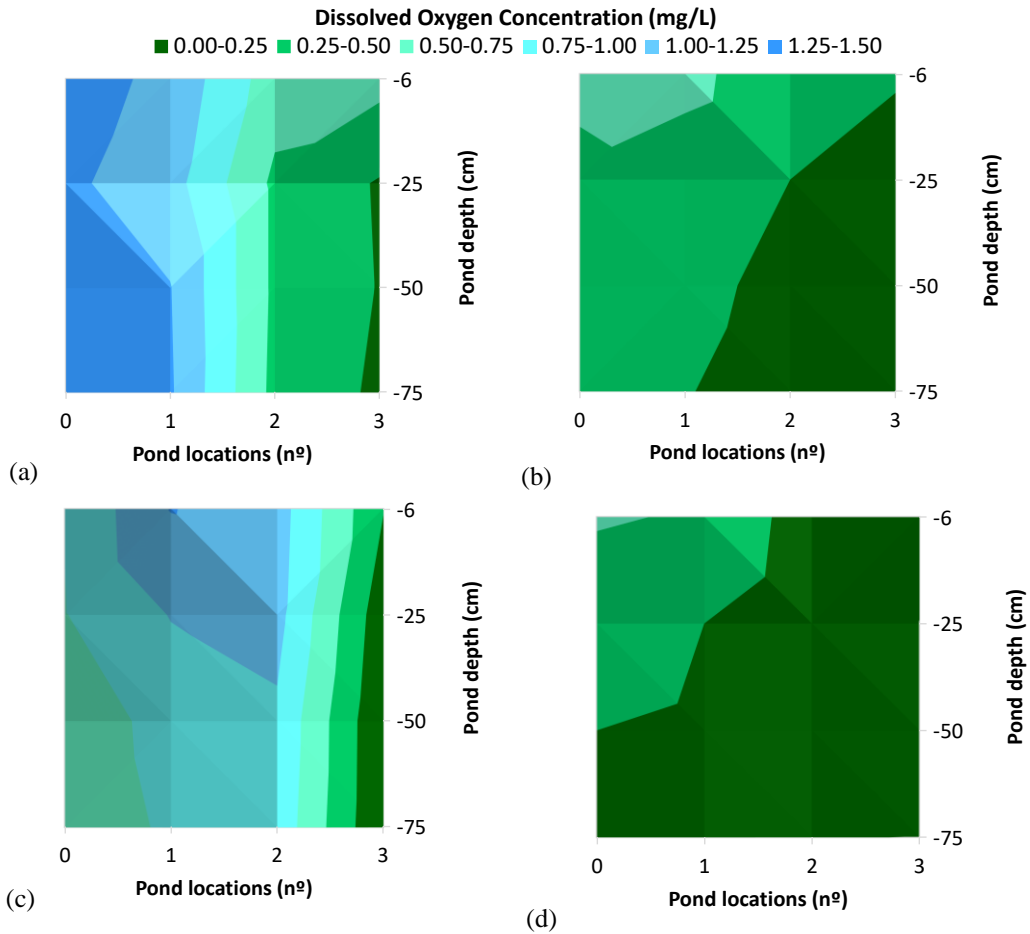
Figure 4. Spatial distribution of DO in different days, (a) 09/092020, (b) 30/09/2021, (c) 15/10/2020, and (d) 11/11/2021

In (c), we can identify a point with having a higher DO concentration than the previously measured point. This point is the measurement at the exit of the first pond. As detailed before, a possible explanation is that an accidental introduction of oxygen happened in the system, caused by diverse conditions of water input or an increased flow.

Concerning the area with low DO (nearly anoxic or anoxic-dark green colour), we see that in regular conditions, we can see that in Figure 4 (a) and (c), most of the ponds present DO concentrations of up to 0.75 mg/L. Thus, only some points of pond 3 present the optimal conditions for the operation of the bacteria.

On the other hand, focusing on Figure 4 (b) and (d), the whole volume of the ponds has a concentration of DO lower than 0.75 mg/L. Thus, up to 50% of the ponds are in a nearly anoxic condition in Figure 4 (d) and up to ¾ in Figure 4 (b).

C. Temporal variability in each measured point

Following, we are going to focus on the temporal variability in each one of the measured points. In this case, we are going to represent all the measured points, including the beginning and end of each pond (6 measured points).

The average value of DO for each sampling point and each depth can be seen in Figure 4, represented in vertical coloured bars. Meanwhile, the black error bars indicate the standard deviation of gathered data. In general terms, we can see that the average values follow the trend of decreasing DO along with the measured points and the depth. Nevertheless, there is a point that does not follow this trend. Measured point 3 has a higher DO concentration than measured point 2. The peak causes this detected on 15/10/2020; this data can be considered as an outlier value. The average values at the bottom are almost identical for the two measured points of the third point (point 5 and 6).

With regards to the standard deviation, we can see that the higher variation is found for measured points 3 and 4 (depth of 6 and 25 cm). Again, this is caused by the peak of DO on 15/10/2020. For measured points 1 and 2, the standard deviation values are between 0.41 and 0.34 (relatively stable along the pond and the depth). Concerning pond 3 (measured points 5 and 6), the standard deviation is much lower in the bottom (0.25 and 0.16 mg/L) than in the surface (0.71 and 0.48 mg/L). Thus, we can affirm that we can find more stable conditions in the third point and less
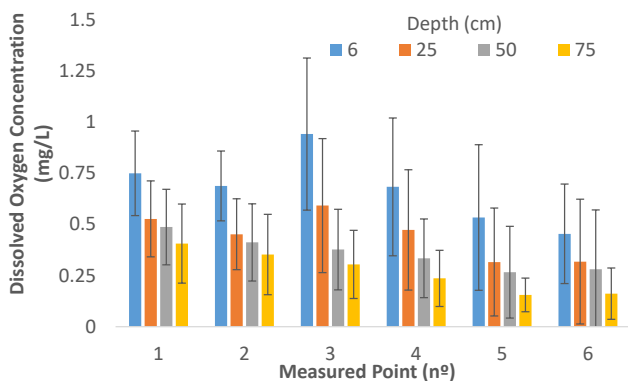
DO than in the previous ponds. This is explained by the characteristics of pumped water in the ponds. The pumped water might suppose an input of oxygen in the system. Moreover, the included oxygen is consumed by the bacterial during the denitrification process.

D. Limitations of the study and evaluation of phytodepuration performance

In this section, we are going to analyse the limitations of the presented research and the implications of the DO concentration on the performance of the phytodepuration.

First of all, the main limitation of our study is the limited number of measurements. Therefore, it will be more accurate to have an in-situ sensor with continuous measurements. Nonetheless, considering the scope of phytodepuration, it is not feasible to bear the costs of the acquisition of this monitoring technology. Therefore, punctual samples are required to evaluate the operation of the whole system.

In addition, there is a limitation in our study considering the input of water. In our case, the pumped water into the system comes from a small area, including the work centre of a research area and a small amount of agroindustry wastewater. Nonetheless, no control has been done regarding the water flow. Thus, we cannot know the flow in our system since it varies over the days, and we cannot estimate a fixed retention time. Moreover, we have performed the study during a rainy period in which abrupt changes in water flow are expected. Finally, we do not know the water conditions in the water reception tank.

Finally, we will evaluate the effect of DO concentrations on the performance of the process. Considering that the majority of the denitrification happened in the bottom of the ponds, we are going the classify if the denitrification process is optimal (nearly anoxic conditions 0 to 0.5 mg/L), good (0.5 to 1 mg/L) or not good (>1 mg/L), see Figure 6. For the first measured point, the entrance of pond 1, in 70% of the measures, the conditions are nearly anoxic; only in 1 case, we find a condition characterised as not good for the bacteria. Similar results are found for the ending of the first pond. Focusing on the second pond, only 10% of the time operates in non-optimal conditions. Lastly, the third pond is always optimal (90%) or good (10%) conditions.

Figure 5.   Mean and standard deviation of measured DO concentration along with the ponds.
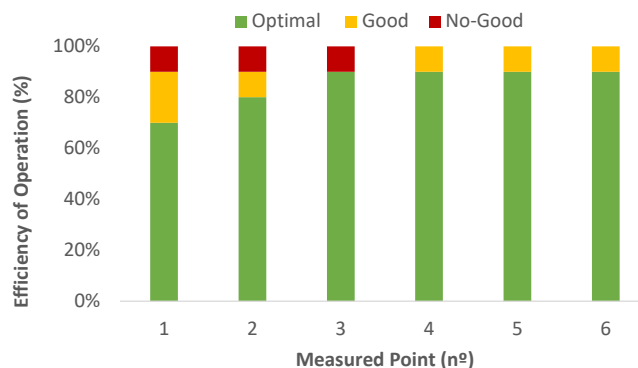
Figure 6.   Operational conditions of the ponds in the studied period.

Although the system has been operating without any restriction or condition in the water flow, we can confirm its proper operation based on water quality values and the DO values. In all the analysed period, both the input and the output of the phytodepuration were periodically measured. The data of total suspended solids confirms that there is a reduction of 80% as average. However, CDO values are relatively low (at the entrance and exit), and the effect of phytodepuration on the reduction or increase of CDO is not yet apparent. Although in some cases CDO decreased, in other cases, it increases. Thus, more research is needed. Concerning the system's productivity, a total of 187.88 kg of typha biomass was harvested on 11/11/2020. It supposes average productivity of 1.8 kg/m^2.

According to our data, the *Typha domingensis* injects a minimal amount of oxygen in the water and has nearly no impact on the measured DO. In similar papers [7], authors have shown how other species have much higher oxygen transference rates. Although the low DO concentration, the combined nitrification-anammox-denitrification process is operating well, and the crops have grown.

V. CONCLUSIONS

In this paper, the temporal variability of DO in phytodepuration ponds is analysed. In phytodepuration, we need a stable and low DO in the bottom to allow denitrification, which converts the organic matter into valuable nutrients for the plants above the water. Thus, the optimal operation of bacteria ensures the cleaning of the water and the growth of the crops.

Our results indicate that the DO is low in the three ponds in general terms, mainly due to the water input and a decreasing DO concentration along with the ponds. The DO also follows a negative gradient along with the depth of the pond. Thus, we have confirmed that our design of a small-scale phytodepuration system with no control on the flow accomplishes DO's expected values and variability.

As future work, we want to evaluate the denitrification process in each pond. We will include low-cost water quality sensors measuring the turbidity and the organic matter developed in [13]. On the other hand, we will study the crop performance in each pond to evaluate if the different amounts of nutrients in the ponds affect crop performance.

ACKNOWLEDGMENT

REFERENCES

[1] A. Petroselli, M. Giannotti, T. Marras, and E. Allegrini, Integrated system of phytodepuration and water reclamation: A comparative evaluation of four municipal wastewater treatment plants. International journal of phytoremediation, 19(6), 2017, pp. 563-571.

[2] D. Chen et al., Denitrification-and anammox-dominant simultaneous nitrification, anammox and denitrification (SNAD) process in subsurface flow constructed wetlands. Bioresource technology, 271, 2019 pp. 298-305.

[3] U. F. Hassan, H. F., Hassan, H. Baba, and A. S. Suleiman, The Feed Quality Status of Whole Typha domingensis Plant. International Journal of Scientific and Engineering Research, 9(5), 2018, pp. 1609-1617.

[4] A. S. Ringim, B. B. Sabo, and H. Harry, Implication of invasive plant Typha domingensis on biodiversity: An ecological study of the Hadejia-Nguru wetlands, Nigeria. Scholarly Journal of Biological Science, 4, 2015, pp. 40-46.

[5] L. García, L. Parra, J. M. Jimenez, J. Lloret, and P. Lorenz, IoT-based smart irrigation systems: An overview on the recent trends on sensors and IoT systems for irrigation in precision agriculture. Sensors, 20(4), 2020, pp. 1042.

[6] A. K. P. Borges, S. M. Tauk-Tornisielo, R. N. Domingos, and D. D. F. D. Angelis, Performance of the constructed wetland system for the treatment of water from the Corumbataí river. Brazilian Archives of Biology and Technology, 51(6), 2008, pp. 1279-1286.

[7] A. Caselles-Osorio, H. Vega, J. C. Lancheros, H. A. Casierra-Martínez, and J. E. Mosquera, Horizontal subsurface-flow constructed wetland removal efficiency using Cyperus articulatus L. Ecological Engineering, 99, 2017, pp. 479-485.

[8] A. Garcia-Perez, M. Harrison, and B. Grant, Recirculating vertical flow constructed wetland for on-site sewage treatment: an approach for a sustainable ecosystem. Journal of Water and Environment Technology, 9(1), 2011, pp. 39-46.

[9] G. H. P. Prado and S. M. Velasco, Fitodepuración de aguas residuales domesticas con poaceas: brachiaria mutica, pennisetum purpureum y panicum maximun en el municipio de Popayán, Cauca. Biotecnología en el sector agropecuario y agroindustrial, 11(2), 2013, pp. 57-65.

[10] R. H. Kadlec and S. D. Wallace, TREATMENT WETLANDS. (2º edition) CRC Press. Taylor & Francis Group. pp. 89, 2009, pp. 90-92.

[11] Z. Chen et al., Hydroponic root mats for wastewater treatment a review. Environmental Science and Pollution Research 23, 2016, pp. 15911-15928.

[12] Specifications of Optical Dissolved Oxygen Meter - HI98198. Available at: https://www.hannainst.com/optical-dissolved-oxygen-meter.html. Last access in 16/04/2021.

[13] L. Parra, S. Sendra, L. García, and J. Lloret, Design and deployment of low-cost sensors for monitoring the water quality and fish behavior in aquaculture tanks during the feeding process. Sensors, 18(3), 2018, pp. 750.

Estimating the Canopy Cover of *Camelina sativa* (L.) Crantz through Aerial RGB Images

David Mostaza-Colado[1], Lidia Díaz-Fuentes[2], Andrea Collado-Gómez[2], Pedro V. Mauri[1], and Aníbal Capuano[3]

[1]Instituto Madrileño de Investigación y Desarrollo Rural, Agrario y Alimentario (IMIDRA), Finca "El Encín", Ctra. A-2, Km 38.200, 28805 - Alcalá de Henares, Madrid, Spain.

[2] Universidad de Alcalá, Alcalá de Henares, Madrid, Spain.

[3] Camelina Company España, Fuente el Saz de Jarama, Madrid, Spain.

Email: david.mostaza@madrid.org, pedro.mauri@madrid.org, acapuano@camelinacompany.es

Abstract—In rainfed agriculture, where crop extensions are high, yields are low and profit margins are tight, expensive solutions for crop monitoring are ineffective. Therefore, achieving an effective, fast, low time consuming, and cheap Crop Coverage or Canopy Cover estimation is important, as it is an indicator of the crop vigor or any issue taking place during the plant growth. Moreover, it is also an interesting way to estimate and evaluate the soil covered by vegetation in degraded rural areas and assess problems with soil erosion due to the lack of vegetation. The use of Remote Sensing Technologies as satellite MultiSpectral images offers numerous advantages, as it is a powerful tool. However, lacks the speed of an Unmanned Aerial Vehicle or drone when gathering images, as it depends on the satellite acquisition calendar. On the other hand, gathering images with conventional cameras is not possible on large farms and plots or hard-to-reach areas. The use of a commercial non-professional drone to gather conventional images of a crop is a useful tool to estimate the canopy cover of the crop in different growth stages. This estimation allows detecting problems during the seeding phase or detecting areas where the crop is not growing, along with measuring the percentage of covered soil by the plant. As showed in this paper, we have managed to estimate the canopy coverage of camelina in an experimental plot seeded in two different dates, and assess the crop performance in a reliable way. The average canopy cover for the late seeded plot was 15.55 %, while the in the early seeded plot was 76.09 %.

Keywords—camelina; remote sensing; canopy cover, soil erosion.

I. INTRODUCTION

Soil erosion is one of the most important factors in land degradation and one of the principal mechanisms of desertification at national and regional levels [1][2]. Due to its geographical location and climate, Spain is one of the country's most severely affected by soil erosion in the European Mediterranean region [3]. The main effects caused by erosion are the loss of agricultural and forest soil fertility, increased degradation of vegetation cover, and a decrease in natural hydrologic control. All these interrelated processes are linked to the threat of desertification and global climate change [4].

In rural areas, poor soil use has negative effects such as loss of fertility, degradation, and desertification. Therefore, it is a natural resource suffering from gradual deterioration; and generates a negative impact on the environment. For this reason, recovery processes of the vegetation and soil cover must be carried out, along with control and mitigation measures of erosion. In addition, it is recommended to implement natural mechanisms that do not generate new environmental impacts. Thus, the use of natural materials or vegetal covers is proposed as a natural remediation [5].

The establishment of vegetal covers is an excellent alternative to prevent erosive processes, since it increases the hydraulic resistance of the land by increasing the stability of the soil aggregates. The soil acquires protection against the impact of raindrops by increasing its infiltration capacity and stopping runoff. Native plants are the best guarantee of a healthy ecosystem, since they are adapted to the characteristics of the field [6].

Camelina sativa (L.) Crantz [camelina] has emerged in recent years as an alternative oilseed and cover crop from the Brassicaceae family. Camelina seed meal and oil can be used for both animal feed and human food, but also has many industrial applications [7]. With a short life cycle, camelina can be an ideal rotational crop as it has two distinctive biotypes, spring, and winter. Winter biotypes require a vernalization treatment to enter the reproductive phase, while spring biotypes do not [8][9]. Increased interest in broadening the diversity of winter-hardy cover crops to reduce soil erosion through the winter months has led this crop to become an excellent choice [8][10]–[12].

As an example, camelina cultivation in the central area of Spain (Comunidad de Madrid, Castilla-La Mancha and Castilla y León) has increased in the past years due to the effort of private and public actors such as Camelina Company Spain [CCE] and Madrid Institute for Rural, Agricultural and Food Research and Development [IMIDRA] [13]–[17]. Therefore, camelina is considered as a growing crop in Spain, leading a special interest in crop diversification. It is a practical and economically viable alternative, supported by its short growth period. At present, institutions promote the production of non-food biomass to contribute to the worldwide change of energy policies. This requires fast-growing species to produce energy or raw materials to produce other combustibles. Two areas of emerging interest from the agricultural sector have converge in recent years: 1) the convenience to promote new systems of agrarian production that result in sustainable rural development in Spain, and 2) the need to substitute the demand of fossil energy with renewable energies, based on the benefit of the environment [18].

Within the CAMEVAR project, we are assessing several varieties of camelina provided by CCE, together with

cultivation techniques and practices in combination with new technologies. In this paper, we analyze the use of Red, Green and Blue [RGB] images gathered with a Parrot Bebop 2 UAV [Unmanned Aerial Vehicle] to estimate the Crop Coverage or Canopy Cover [CC] of camelina. We will determine the percentage of soil and vegetation through a combination of the images bands to assess the evolution of the crop, seeded in two different dates.

The rest of the paper is structured as follows: Section II outlines related works; Section III describe the materials and methods; Section IV analyzes the results and highlights the importance of assessing the evolution and coverage of certain crop; finally, conclusions and future work are summarized in Section V.

II. RELATED WORK

In this section, we summarize some of the related works to estimate crop coverage through remote sensing, either with RGB images or MultiSpectral [MS] sensors.

Alatorre et al. [19] analyzed the temporal evolution of plant activity on vegetated areas and in erosion risk zones in a small area of the central Pyrenees during the period 1984-2007 from two Landsat Normalized Difference Vegetation Index [NDVI] time series for the months of March and August through MS sensors. This allowed the analysis of the spatial and temporal dynamics of plant activity in areas with good plant cover (forests and dense scrub) and in degraded areas affected by erosion processes (gullies and erosion risk areas). Through a multivariate regression, NDVI trends were analyzed considering climatic factors. The spatial resolution of the Landsat image allowed a good representation of the selected covers. The study showed that in the Pyrenees there has been an increase in plant activity in the last 24 years due to the increase in temperature. However, the extreme conditions that exist in this area with active erosion and areas at risk of erosion did not allowed the recovery of the vegetation among the study period. The issue about MS sensors is that they are more sensitive and expensive compared to RGB sensors.

Basterrechea et al. [20] proposed a system to evaluate the changes in grass coverage between covered plots and non-covered plots, between summer and winter. They aimed to obtain an economical device for farmers to consult the status of grass coverage in crops and to improve the quality and quantity of harvested fruits. The study used the Sentinel-2 satellite platform to gather images in the different bands of RGB, Near InfraRed [NIR], Water Vapor Permeability [WVP], and NDVI index for different times of the year to evaluate changes between plots with coverage and plots without grass coverage.

Regarding the use of RGB images, an alternative to obtain high-resolution spatial and temporal images is the implementation of UAVs equipped with digital cameras. In images with high spatial resolution, it is necessary to know the vegetation index that best identifies the pixels that contain vegetation and those that do not, as well as the threshold value that allows separating both classes. Marcial Pablo et al. [21], used the Otsu-Valley algorithm to estimate the plant cover of the corn crop combined with the Excessive Greenness index

[ExG]. This algorithm establishes that the optimal threshold to separate the image into differentiated classes resides in the value of the spectral histogram located between its two maximum peaks. As it calculates the most appropriate threshold during the intermediate stage of crop growth, with accuracies greater than 94 %. Therefore, they accomplished a high precision in the estimation of vegetation cover using the ExG index and the Otsu algorithm in early stages of crop growth.

As Asahpure et al. recall [22], RGB-based CC estimation methods can be divided into two categories: 1) thresholding method that requires the specification of the color thresholds or the ratios to identify canopy pixels; and 2) pixel classification methods that use a supervised or unsupervised pixel-wise classification method to identify canopy pixels. Though pixel classification methods are highly accurate, they are time consuming and computationally extensive. Supervised classification methods require training samples to be collected, which is expensive and prone to human error. However, pixel classification methods are particularly useful to calibrate thresholding methods [23].

There is a large amount of work in the literature that uses RGB sensors to compute CC. Early work in this direction includes the quantification of turfgrass cover using digital image analysis by Richardson et al. [24], where digital image analysis proved to be an effective method to determine turfgrass cover, producing both accurate and reproducible data. Lee and Lee [25], estimated canopy cover over the rice field using an RGB sensor which is a nondestructive, low-cost, and convenient method for estimating CC using digital camera image analysis. CC was estimated by the ratio of plant pixels to total pixels with an image analysis program developed in Visual Basic to extract RGB features from the mosaic images. Then they calculated the RGB-based color index and compute the minimum segmentation error for separating rice plant from background.

Finally, Marín et al. [26] showed the accessibility, easy use and low cost of digital RGB cameras as a perfect device for turfgrass green biomass estimation and water management, especially under limited growing conditions.

As we have showed, the use of RGB images is common in CC estimation of diverse crops, but there is no evaluation of these methods in camelina; as most of the studies are based on MS index to evaluate other crops performance or yield [27][28]. The use of UAVs for proximal remote sensing on a crop as camelina offers better results than satellite remote sensing, ground taken images or Unmanned Terrestrial Vehicles [UTVs]. Therefore, using UAV imaging produces a detailed CC map of the field in timely and inexpensive manner. Moreover, the crop growth can also be monitored by using UAVs and generate on-go vegetation index to assess the crop health and determine if it is necessary to apply fertilizers or herbicides [29].

III. MATERIAL AND METHODS

In this section, we will detail the procedure followed to gather and process the data from the field, as well as the software and hardware employed to obtain and analyze the results.

A. Crop seeding

Within the framework of CAMEVAR project, IMIDRA collaborates with CCE in assessing several camelina varieties and how they adapt to the central area of Spain. To perform this essay, we seeded four replicas of a winter camelina variety (V11) in two different dates (December 2nd, 2020 and February 18th, 2021) in "Finca El Encín", Alcalá de Henares, Madrid (Spain) facilities. The soil at this location is a typical Fluvisol (Calcaric), according to the World Reference Base for Soil Resources 2014 [30]. These soils are developed in fluvial deposits as river plains, valleys, lake depressions and tidal marshes on all continents and in all climate zones. They lack of groundwater or high salt contents in the topsoil. In addition, many Fluvisols under natural conditions are flooded periodically. Also, these soils profiles have evidence of stratification and a weak horizon differentiation, but a distinct topsoil horizon may be present.

We used two seeding techniques and applied two concentrations of Urine derived Fertilizer [UdF] (low-60 and high-90). Therefore, each plot had a combination of two different seeding methods: 1) broadcast, without burying the seed and 2) in rows, burying the seed. Each individual plot was 1m wide and 15m long. For this purpose, we used a Wintersteiger self-propelled TC plot seeder. The seeding dose was 8 kg/ha and the plot had no irrigation, as it is a rainfed crop. The distribution of the individual plots was as follow: (A) 1st seeding date – broadcast – 60UdF; (B) 1st seeding date – broadcast – 90UdF; (C) 1st seeding date – rows – 60UdF; (D) 1st seeding date – rows – 90UdF; and (E) 2nd seeding date – broadcast – 60UdF; (F) 2nd seeding date – broadcast – 90UdF; (G) 2nd seeding date – rows – 60UdF; (H) 2nd seeding date – rows – 90UdF (H) (Figure 1).

B. UAV specifications and image gathering

Images to estimate the camelina CC where taken on April 19th, 2021 at X475093 Y4486168 ETRS89-30N. We used a Bebop 2 UAV with a 24-bit color RGB camera and a resolution of 1440x1080 pixels to take zenithal pictures of the camelina canopy at 15 m height. This UAV has an autonomy of 25 min, enough to capture the study area or even larger surfaces.

C. Image processing

We selected QGIS 3.16.4-Hannover [31] to process the images, as it is a free and open software, to simplify the CC calculation. First, images where cropped to treat each image individually (P1 to P8) (Figure 1). And they were later included in QGIS.

A RGB image is composed of three bands. The linear combination of these bands produces the picture that the naked eye sees. Nonetheless, when these bands are combined in a different way, several indexes appear. As we wanted to estimate the CC, we choose to differentiate soil form vegetation. We also supposed that all the crop present in the picture was camelina, as the presence of weeds was low. Later we processed the images according to a soil index Eq. (1) [32].

$$Soil\ Index\ (SI) = G_{band}/R_{band} \quad (1)$$
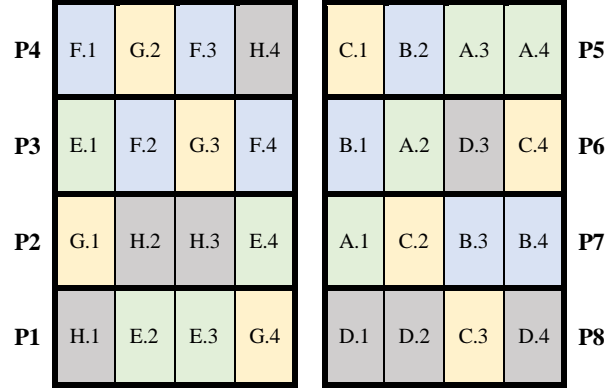
Figure 1. Plots disposition for each seeding date.
(A to D: first seeding date; E to F: second seeding date).
P1 to P8 are enumerated according to the flight order of the UAV (clockwise).

This index is based on the fact that the soil has higher values of brightness in the red band [R] than in the green band [G]. Therefore, it divides the green band by the red band obtaining a new image, which gives information about the soil/plant coverage. Following, each image was reclassified with a determinate threshold to differentiate soil from vegetation. Pixels between 0 and 1 where reclassified as 0 and considered soil (black pixels); pixels over 1 where classified as 1 and considered vegetation (white pixels) (Figure 2 and Figure 3). Once the images were reclassified, we used the QGIS tool "*zonal statistics*" to calculate the numbers of pixels with 0 and 1 value. Finally, we estimated the proportion of CC in each plot from this numbers, expressed as a percentage of soil covered by the camelina canopy (Table I).

IV. RESULTS

In this section, we will analyze the obtained data. We will compare the CC of the same camelina variety, seeded in two different dates and with differential fertilization rates.

A. Canopy cover

We have considered the camelina CC in two different growth stages of the crop. One, almost fully developed with flower and fruits appearing (1st seeding date – P5 to P8) and 40 cm to 50 cm height (600 BBCH scale [33]), and another as a rosette with the plant at ground level (2nd seeding date – P1 to P4). The differences in the CC are remarkable and as expected. Camelina phenological stages are different so the percentage of soil covered is higher as the plant is bigger (TABLE I). The average CC for P1 to P4 plots is 15.55%, while the average CC for P5 to P8 plots is 76.09%.

In addition to the CC ratio, there are other interesting parameters that can be assessed with the RGB processed images: the correctness of the seeding procedure or the effects of the different crop management procedures employed, as long as if there are differences in the applied fertilization dose.

We must emphasize that this paper we are presenting is a work in progress, as the crop is still growing, and we keep gathering data.

Nevertheless, we have detected some issues with the Wintersteiger plot seeder: the middle of the seeding route has

less density than the edges. This is a phenomenon that happens in all the plots (P1 to P8) (Figure 2 and Figure 3). Because of this, the central area CC is lower, as is the density of plants too. Even though the dose of seeds was the same, the blooming of the plant was not.

TABLE I. CAMELINA CANOPY COVERAGE

Camelina Canopy Cover (CC)	PLOT (P)
14.88%	1
27.04%	2
9.67%	3
10.64%	4
69.17%	5
76.19%	6
78.24%	7
80.76%	8

P1 (RGB)   P1 (CC)   P2 (RGB)   P2 (CC)

P3 (RGB)   P3 (CC)   P4 (RGB)   P4 (CC)
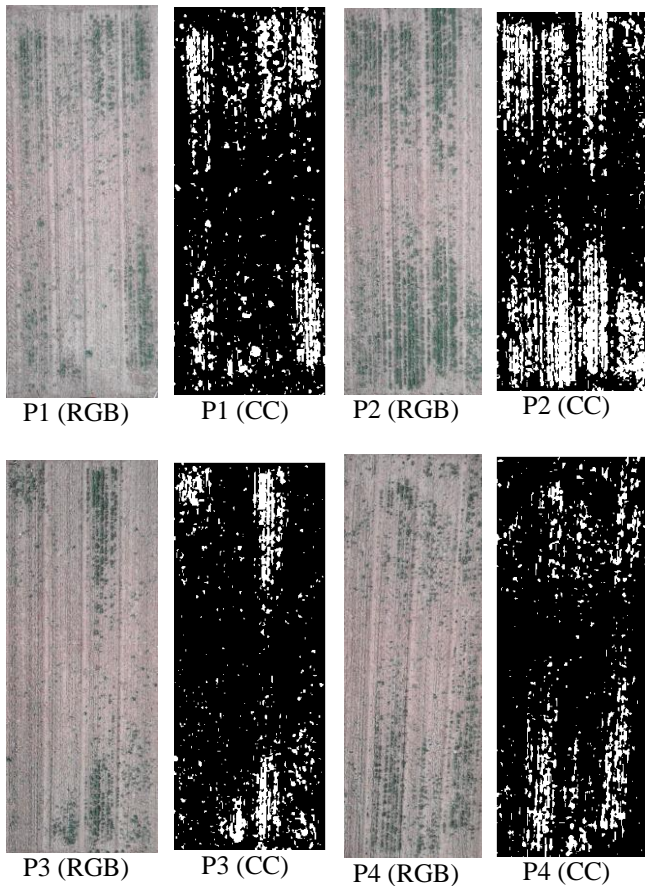
Figure 2.   Camelina coverage. Plots seeded on February 18th, 2021.

If we analyze P5 to P8, as they were seeded first, we appreciate some differences in the seeding procedure: P5-C.1 and P8-D.1-D.2-C.3-D.4 replicas were seeded using the rows procedure (the seed is slightly buried in the ground) and they

have a higher CC (Figure 3). The visible density of white pixels is higher in those bands. When compared to P1 to P4 plots, the rows seeding procedure seems to behave better, as there is a higher density of white pixels in those bands too, e.g., P2-G.1-H.2-H.3 and P4-G.2-H.4.

P5 (RGB)   P5 (CC)   P6 (RGB)   P6 (CC)

P7 (RGB)   P7 (CC)   P8 (RGB)   P8 (CC)
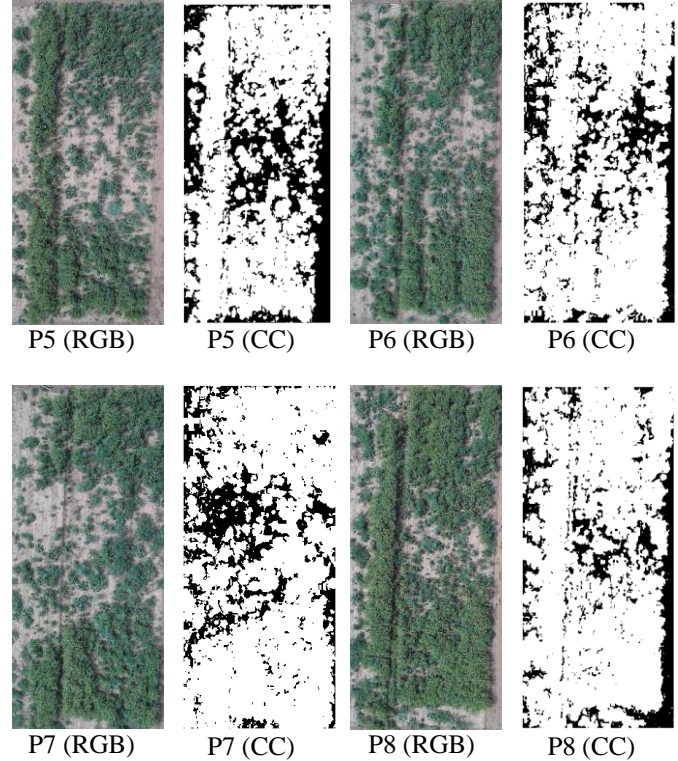
Figure 3.   Camelina coverage. Plots seeded on December 2nd, 2020.

Regarding the use of two fertilizer doses, results are not conclusive yet. As we have to harvest the crop and calculate the seed yield per hectare and plant weight (biomass). However, the CC results are quite promising. When comparing P8-D.1 to P5-C.1 (same seeding date and procedure, but different UdF doses), P8-D.1 (90UdF) seems to have a more consistent CC of camelina. The remaining bands do not seem to show remarkable differences when compared by the fertilizer dose. Still, we expect to appreciate these differences in further UAV flights, when the crop is in a later phenological stage.

V.   CONCLUSIONS

Through this paper, we have presented an easy, cheap, and effective way to assess the canopy coverage of camelina crops. This is relevant as it allows the farmer or investigator to assess the growing of the crop and determine if there has been any issue during the seeding procedure. Even though, once the essay or crop are seeded, if there is any problem it would be difficult to solve. So by flying the UAV as a check procedure, this could be issued in further campaigns to avoid echoing the previous mistakes. Capturing images with this kind of UAVs and RGB cameras is very cheap, as well as the post processing of the images. In addition, the information

gathered could be a potential game changer in the management of large rainfed crops areas, where the benefits of the crop are tight.

As this paper is a current work, we aim to compare the gathered data with results from seed yield and plant development, and with thermal images in larger plot areas. Therefore, we could aim to assess detecting diseases in large crop areas, or not growing spots that could reduce the final yield of the crop.

REFERENCES

[1] L. Martín-Fernández and M. Martínez-Núñez, "An Empirical Approach to Estimate Soil Erosion Risk in Spain," *Science of the Total Environment*, vol. 409, no. 17, pp. 3114–3123, 2011, doi: 10.1016/j.scitotenv.2011.05.010.

[2] MARM, "Suelo," in *Perfil Ambiental de España 2008. Informe basado en indicadores*, Madrid: Ministerio de Medio Ambiente y Medio Rural y Marino, 2008, pp. 102–113.

[3] A. S. Benet, "Spain," in *Soil Erosion in Europe*, J. Boardman and J. Poesen, Eds. Chichester, UK: John Wiley & Sons, Ltd, 2006, pp. 311–346. doi: 10.1002/0470859202.ch26.

[4] M. Torres-Quevedo Garcia De Quesada, F. Jarabo Sanchez, E. Del Palacio Fernández-Montes, and J. A. Garcia De Las Barreras, "El Inventario Nacional de Erosión de Suelos 2002–2012," *Revista Montes*, no. 75, pp. 34–41, 2004.

[5] C. Díaz-Mendoza, "Alternativas para el control de la erosión mediante el uso de coberturas convencionales, no convencionales y revegetalización," *Ingeniería e Investigación*, vol. 31, no. 3, pp. 80–90, 2011.

[6] V. Alvarado García, "La vegetación como factor de control de la erosión," *Repertorio Científico*, vol. 19, no. 1, pp. 13–17, 2016.

[7] M. Berti, R. Gesch, C. Eynck, J. Anderson, and S. Cermak, "Camelina Uses, Genetics, Genomics, Production, and Management," *Industrial Crops and Products*, vol. 94, pp. 690–710, 2016, doi: 10.1016/j.indcrop.2016.09.034.

[8] A. Wittenberg, J. V. Anderson, and M. T. Berti, "Winter and Summer Annual Biotypes of Camelina Have Different Morphology and Seed Characteristics," *Industrial Crops and Products*, vol. 135, no. March, pp. 230–237, Sep. 2019, doi: 10.1016/j.indcrop.2019.04.036.

[9] A. Wittenberg, J. V. Anderson, and M. T. Berti, "Crop growth and productivity of winter camelina in response to sowing date in the northwestern Corn Belt of the USA," *Industrial Crops and Products*, vol. 158, no. October, p. 113036, 2020, doi: 10.1016/j.indcrop.2020.113036.

[10] M. Leclère, C. Loyce, and M. H. Jeuffroy, "Growing camelina as a second crop in France: A participatory design approach to produce actionable knowledge," *European Journal of Agronomy*, vol. 101, no. November, pp. 78–89, 2018, doi: 10.1016/j.eja.2018.08.006.

[11] A. Solis, I. Vidal, L. Paulino, B. L. Johnson, and M. T. Berti, "Camelina seed yield response to nitrogen, sulfur, and phosphorus fertilizer in South Central Chile," *Industrial Crops and Products*, vol. 44, pp. 132–138, 2013, doi: 10.1016/j.indcrop.2012.11.005.

[12] R. N. Dharavath, S. Singh, S. Chaturvedi, and S. Luqman, "Camelina sativa (L.) Crantz A mercantile crop with speckled pharmacological activities," *Annals of Phytomedicine: An International Journal*, vol. 5, no. 2, pp. 6–26, 2016, doi: 10.21276/ap.2016.5.2.2.

[13] P. V. Mauri Ablanque, A. Capuano, J. Ruiz Fernández, and D. Mostaza Colado, "Operational Group Project for Disclosure of the Cultivation of the Camelina in the Center of Spain," in *23rd International Congress on Project Management and Engineering*, 2019, vol. 029, no. July, pp. 1584–1594. [Online]. Available: http://dspace.aeipro.com/xmlui/handle/123456789/2344

[14] P. V. Mauri Ablanque, A. Plaza Benito, G. Hernando, and A. Capuano, "Methodological Comparison of Different Camelina Cultivation Cycles: Species of Interest in Spain," in *22nd International Congress on Project Management and Engineering*, 2018, pp. 1315–1323.

[15] D. Mostaza-Colado, P. v. Mauri Ablanque, and A. Capuano, "Assessing the Yield of a Multi-Varieties Crop of Camelina sativa (L.) Crantz through NDVI Remote Sensing," in *2019 Sixth International Conference on Internet of Things: Systems, Management and Security (IOTSMS)*, Oct. 2019, pp. 596–602. doi: 10.1109/IOTSMS48152.2019.8939264.

[16] S. Martinez, S. Alvarez, A. Capuano, and M. del M. Delgado, "Environmental performance of animal feed production from Camelina sativa (L.) Crantz: Influence of crop management practices under Mediterranean conditions," *Agricultural Systems*, vol. 177, no. January, p. 102717, 2020, doi: 10.1016/j.agsy.2019.102717.

[17] M. del M. Delgado *et al.*, "Efecto residual provocado por dos lodos de depuradora procedentes de un ensayo de fitorremediación con cardo en un cultivo de camelina (Camelina sativa (L.) Crantz) en Madrid," *Revista de la Facultad de Ciencias Agrarias*, vol. 48, no. 2, pp. 13–30, 2016.

[18] D. Mostaza-Colado, P. v. Mauri, S. Yousfi, and A. Capuano, "Camelina sativa (L.) Crantz Seed Germination: Measurement of the Germination Potential under Different Temperatures," in *EUBCE 2020 (28th European Biomass Conference and Exhibition)*, 2020, pp. 242–245. doi: 10.5071/28thEUBCE2020-1DV.2.38.

[19] L. C. Alatorre, S. Beguería, and S. M. Vicente-Serrano, "Análisis de la evolución espacio-temporal del NDVI sobre áreas vegetadas y zonas de riesgo de erosión en el Pirineo Central," *Pirineos*, vol. 165, no. 165, pp. 7–27, Dec. 2010, doi: 10.3989/Pirineos.2010.165001.

[20] D. A. Basterrechea, L. Parra, M. Parra, and J. Lloret, "A Proposal for Monitoring Grass Coverage in Citrus Crops Applying Time Series Analysis in Sentinel-2 Bands," in *4th EIA Inernational Conference, Industrial IoT 2020*, 2021, pp. 193–206. doi: 10.1007/978-3-030-71061-3_12.

[21] M. de J. Marcial Pablo, W. Ojeda Bustamante, S. I. Jiménez Jiménez, and R. E. Ontiveros Capurata, "Estimación De La Altura Del Cultivo De Maíz Usando Imágenes RGB Obtenidas Con Un Dron," 2019.

[22] A. Ashapure, J. Jung, A. Chang, S. Oh, M. Maeda, and J. Landivar, "A Comparative Study of RGB and Multispectral Sensor-Based Cotton Canopy Cover Modelling Using Multi-Temporal UAS Data," *Remote Sensing*, vol. 11, no. 23, p. 2757, Nov. 2019, doi: 10.3390/rs11232757.

[23] D. T. Booth, S. E. Cox, and R. D. Berryman, "Point Sampling Digital Imagery with 'Samplepoint,'" *Environmental Monitoring and Assessment*, vol. 123, no. 1–3, pp. 97–108, Nov. 2006, doi: 10.1007/s10661-005-9164-7.

[24] M. D. Richardson, D. E. Karcher, and L. C. Purcell, "Quantifying Turfgrass Cover Using Digital Image Analysis," *Crop Science*, vol. 41, no. 6, pp. 1884–1888, Nov. 2001, doi: 10.2135/cropsci2001.1884.

[25] K.-J. Lee and B.-W. Lee, "Estimating canopy cover from color digital camera image of rice field," *Journal of Crop Science and Biotechnology*, vol. 14, no. 2, pp. 151–155, Jun. 2011, doi: 10.1007/s12892-011-0029-z.

[26] J. Marín, S. Yousfi, P. V. Mauri, L. Parra, J. Lloret, and A. Masaguer, "RGB Vegetation Indices, NDVI, and Biomass as Indicators to Evaluate C3 and C4 Turfgrass under Different Water Conditions," *Sustainability (Switzerland)*, vol. 12, no. 6, 2020, doi: 10.3390/su12062160.

[27] C. Zhang *et al.*, "Image-Based Phenotyping of Flowering Intensity in Cool-Season Crops," *Sensors*, vol. 20, no. 5, p. 1450, Mar. 2020, doi: 10.3390/s20051450.

[28] F. Angelopoulou, E. Anastasiou, S. Fountas, and D. Bilalis, "Evaluation of Organic Camelina Crop Under Different Tillage Systems and Fertilization Types Using Proximal Remote Sensing," *Bulletin of University of Agricultural Sciences and Veterinary Medicine Cluj-Napoca. Horticulture*, vol. 77, no. 1, p. 1, Jun. 2020, doi: 10.15835/buasvmcn-hort:2019.0025.

[29] M. C. Vuran, A. Salam, R. Wong, and S. Irmak, "Internet of underground things in precision agriculture: Architecture and technology aspects," *Ad Hoc Networks*, vol. 81, pp. 160–173, 2018, doi: 10.1016/j.adhoc.2018.07.017.

[30] IUSS Working Group WRB, "World Reference Base for Soil Resources 2014, update 2015. International soil classification system for naming soils and creating legends for soil maps," Rome, 2015. doi: 10.1017/S0014479706394902.

[31] QGIS Development Team, "QGIS Geographic Information System." Open Source Geospatial Foundation Project, 2018.

[32] L. Parra, M. Parra, V. Torices, J. Marín, P. V. Mauri, and J. Lloret, "Comparison of Single Image Processing Techniques and Their Combination for Detection of Weed in Lawns," in *International Journal On Advances in Intelligent Systems*, 2019, vol. 12, no. 3–4, pp. 177–190.

[33] T. Martinelli and I. Galasso, "Phenological growth stages of Camelina sativa according to the extended BBCH scale," *Annals of Applied Biology*, vol. 158, no. 1, pp. 87–94, 2011, doi: 10.1111/j.1744-7348.2010.00444.x.

Development of a Low-Cost Optical System for Monitoring Plastics in Irrigation System Grids

Daniel A. Basterrechea[1], Sandra Sendra[1], Lorena Parra[1,2], Jaime Lloret[1]

[1] Instituto de Investigación para la Gestión Integrada de Zonas Costeras, UniversitatPolitècnica de València. C/ Paranimf nº 1, Grao de Gandía – Gandía, Valencia (Spain)

[2] Instituto Madrileño de Investigación y Desarrollo Rural, Agrario y Alimentario (IMIDRA), Finca "El Encin", A-2, Km 38, 2, 28800 Alcalá de Henares, Madrid, Spain

E-mail: - dabasche@epsg.upv.es, sansenco@upv.es, loparbo@doctor.upv.es, jlloret@dcom.upv.es

Abstract— The plastics incorporated into the irrigation channel of agricultural plots is a major problem due to the outline produced by these in the gratings present in these systems. In this article, we present a low-cost system based on artificial intelligence to monitor the presence of plastics in the gratings of agricultural irrigation channels. For this purpose, an experiment has been carried out using a fish tank, where a grid with bag sections has been placed. Different photographs were taken at 10 cm from the camera, with 0 g, 5 g and 10 g of soil added. Once the images were obtained, the Matlab programme was used to process them and obtain histograms of the red, green, and blue bands. The best results are shown in the image with 0 g of soil and 5 g of soil. The verification carried out with 0 g of turbidity shows that the % of pixel number of the grids are above the limit of 5%, the maximum value for the grids is 84.08%, being the percentage of pixel number of the bags below this limit with a maximum value of 0.09%.

Keywords—Optical system; plastic monitoring; irrigation system; image processing, RGB.

I. INTRODUCTION

Plastics are synthetic materials produced by synthetic or semi-synthetic organic polymers [1]. More than 8.3 billion metric tons of plastics have been produced since the 1950s and the proliferation in their use has been exponential [2]. Plastics are inexpensive, versatile, lightweight, and durable. This fact makes plastic containers used to store a multitude of different materials, from objects to food, because they act as a barrier preventing contamination. Besides, they support the family economy and food security by minimizing post-harvest losses, increasing shelf life and storage capacity [3].

The great versatility of these makes their production increase every day, making them one of the most important pollutants at the marine and terrestrial level due to their difficult degradation. The fact of its prevalence in these environments makes it become a worldwide problem. One of the main problems is that it prevents the proper growth of plants, as well as that of crops, generating agricultural pollution [4].

Plastics can also be a major problem for the irrigation system because the accumulation of plastics in the gratings of agricultural irrigation canals causes runoff, reducing the irrigation flow. In addition to a reduction in water flow, the accumulation of these plastics indirectly also causes other materials, such as leaf debris or branches to accumulate on these gratings, allowing the flow to increase in one part of the grating, causing overflow and loss of water. This loss of water may be relevant, since Agriculture accounts for about 33% of total water use in Europe, and water use is most intensive in southern parts of Europe, where 80% of total water consumption goes to crop irrigation [5].

The most commonly used method for the detection of plastics is the satellite method. This system is especially suitable for open surfaces with a large surface area. In this case, satellite images are not suitable because the irrigation channel of agricultural plots is a small system, which results in the inefficiency of this type of method. In addition, satellite imagery is often very expensive and not affordable for farmers [6]. In this paper, we propose a sensor for detecting the presence of plastics in the irrigation grids to control, detect, eliminate and prevent plastic bags, bottles, or other plastic waste, dumped by humans, from damaging not only the crops, if not our own body. The proposed system will be of great use to farmers, as it will provide a plastic detection tool to prevent outbreaks in irrigation canals. It will be useful to ensure optimal water flow within the system. To do this, a camera will be installed in the irrigation grid, which will be able to detect the presence of plastics and differentiate it from other materials. Artificial intelligence will be used for this, through image processing. In this way, this sensor will send an alert to the user of the said grid of the presence of plastics, so that the user can remove them, avoiding not only the contamination of their growing area but also the subsequent dumping of said plastics in more advanced areas of a said chain like the seas, oceans, or our bodies.

The rest of the paper is structured as follows. In Section II, we explain the related work. The test bench is presented in Section III. Section IV shows the system proposal for our prototype. The results are described in Section V. Then, Section VI displays the verification of the experiment. Finally, in Section VII, we expose the main conclusion and future work.

II. RELATED WORK

In this section, we analyze the different methods used to detect the presence of plastics in aquatic environments, although it should be noted that so far, no detection system has been found in irrigation grids for agriculture.

In 2018 Karaba et al. [7], using equipment mounted on a C-130 aircraft, which captured SWIR Red, Green, and Blue (RGB) and hyperspectral images, detect plastics in the ocean. However, this technique requires a large infrastructure, as well as being very expensive. They established that the absorption of ~1215 and ~1732 nm can be used for applications in the detection of ocean plastics from spectral information. Secondly, Biermann et al. in 2020 [8] demonstrated that floating macroplastics are detectable in optical data acquired by the sentinel-2 satellites of the European Space Agency (ESA). In addition, these could be distinguished from natural materials like algae. On the other hand, they detected patches of materials on oceanic surfaces, which employing the Floating Debris Index (FDI). Taking advantage of this way, the spectral information to differentiate the macroplastics. The classification was carried out with 86% precision. Recently, Iri et al. [9] in 2021, have developed an optical system capable of detecting microplastics in water. The developed sensor is based on a low-cost system based on a spectrophotometer. The system

they use is capable of detecting microplastics below 0.015 p / v.

In 2020, a methodology was carried out to provide a rapid and cost-effective characterization and quantification of the transport of floating macroplastics in the Rhine river by Vriend [10]. This study is based on visual observation, combined with passive sampling to arrive at an estimate of the transport of macroplastics as well as the most abundant types of plastics in this river. In this way, they studied the advantages and disadvantages of current sampling systems and established a new perspective for new monitoring systems. In the same year, Van Lieshout et al. [11], presented a method for the detection of plastics. This system is based on an automated system monitoring that detects said contamination. They installed cameras on bridges along the river, and from the images taken and through deep learning; they were able to estimate the plastic density. Its system is capable of distinguishing plastics from environmental elements.

Studies on the hyperspectral reflectance of virgin plastics degraded by nature and submerged in water at different concentrations and depths of suspended sediments have been carried out by Moshtaghi et al. in 2021 [12]. Besides, more analysis has been carried out on the different types of existing polymers to had better understand the effect of water absorption. The results show the importance of using spectral wavebands in both the visible and Short-Wave Infrared (SWIR) spectra for debris detection, especially when plastics are damp or slightly submerged, which is often the case in environments natural aquatic.

Although some of these systems are based on optical systems, at the moment no system has been found that is established in a fixed point, and that sends alarms simply and easily to the farmer himself. In addition, the systems found are often expensive systems that require sophisticated devices such as airplanes, satellites, among others. It is for this reason that the sensor that we have developed, in addition to being cheap, easy to use, and allows monitoring in real-time what is happening at a specific point.

III. PROPOSAL

Because the presence of plastics or objects in the irrigation channels of pipes can cause important problems and damages in systems, it is important to determine if some element is hindering the normal flow of water. To do that, we propose the use of a camera and an intelligent algorithm to periodically analyse the status of the grid. This section describes the decision algorithm used to detect if plastic is present in our grid.

A. System description.

In order to detect if plastic or object is blocking or hindering the flow of water through a grid, we propose the use of a camera to take pictures of this grid when water is being used. As Figure 1 shows, the camera is inside the water channel. The system also includes a turbidity sensor [13]. After taking a picture, the image is wirelessly transmitted to a node that will be in charge of processing the received image. Although there are several techniques for data computing, our system performs a local computation (edge computing). In this sense, the replies required to solve the problem of plastic presence in the grid are faster than techniques such as fog computing or cloud computing.

When plastic is detected, the node creates an alarm and sends it to the server application. The server is in charge of warning the users or farmers through a Graphic User Interface (GUI) previously installed in the farmer's Smartphone. The farmer can stop the irrigation process and remove the plastic from the grid.

On the other hand, the whole process is stored in a database join with other possible parameters monitored in the crop. The images are also stored in the database with the results of processing them. With that, we are creating a database to permit the system to learn from previous experiences for generating more accurate decisions in further situations.
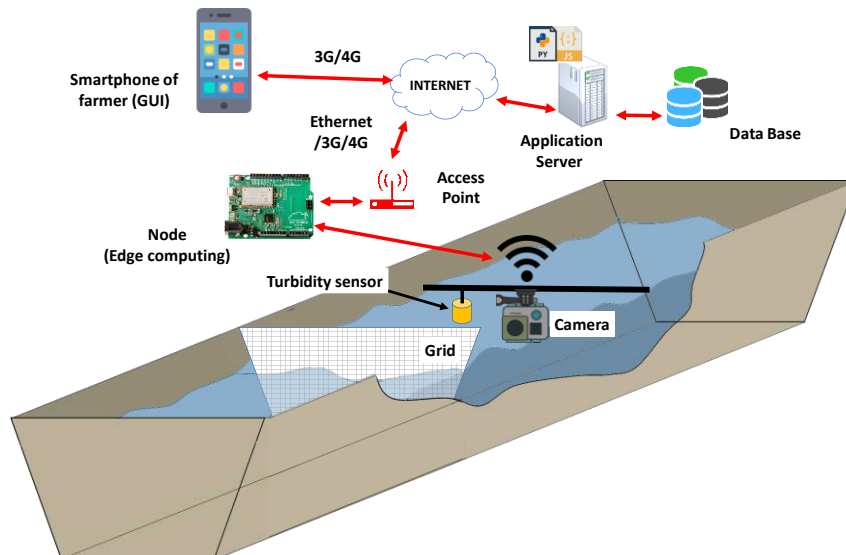
Figure 1. Proposed system.
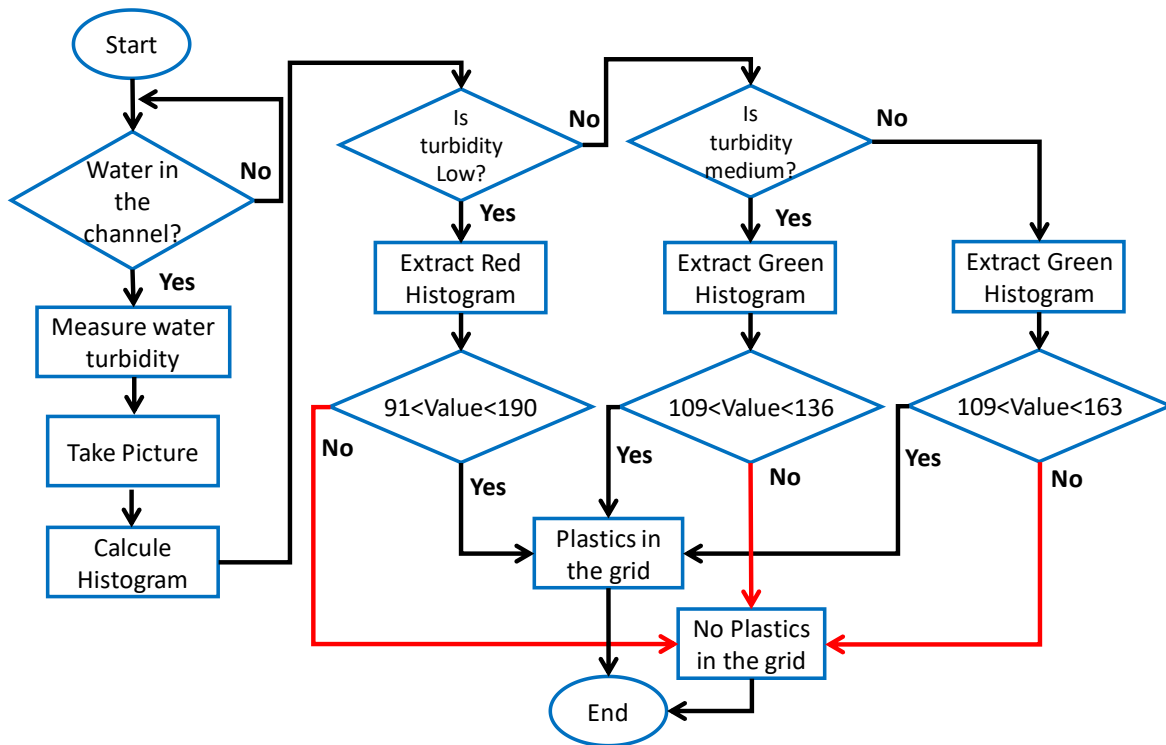
Figure 2. Decision Algorithm

B. Decision algorithm.

In order to be able to detect the presence of plastics in the grid, it is important to recognize the grid shape from the plastics that do not usually present the same shape. It is possible to apply complex AI-based algorithms to firstly detect the shape of the grid and subtracts it from the obtained image. In our case, we will distinguish the grid by analyzing its RGB components from the RGB components of plastics. Figure 2 displays the decision algorithm that we propose.

When the irrigation process is started, the system checks if there is water in the channel. After that, the level of turbidity is measured. According to the turbidity level, the thresholds for detecting plastics on grids will change. The next step is to take the picture and calculate its RGB histogram. When low turbidity is detected, the red histogram is considered. In this case, the biggest contributions in pixels should be concentrated between 91 and 190. When a medium turbidity level is detected, the green histogram is analysed. In this case, the biggest contributions in pixels should be concentrated between 109 and 136. Finally, if high turbidity is detected, we have also considered the green turbidity. In this case, the biggest contributions in pixels should be concentrated between 109 and 163. Inside these ranges, the system will inform on the presence of plastics. In any other case, the system will tag the measures as non-plastic in the grid.

IV. TEST BENCH

In this section, we present the materials used for the experiment. Besides, the methodology used for data collection is described.

A. Materials

For the experiment, a rectangular glass fish tank with dimensions of 24.5 cm high, 26 cm wide, and 50 cm long were used. A white plastic grid 23 cm high and 25 cm wide was used to simulate the presence of a grid. Two pieces of plastic supermarket bags were placed on the grid to represent the plastic waste that humans throw into the environment. Soil with a composition of 4.3 % sand, 67.3% silt, and 28.4 % clay was used as a turbidity-enhancing compound. In order to stabilize the light input in the tank and to obtain a homogeneous light distribution, a tank light was used. In addition, a Xiaomi Red Mi Note 6 Pro mobile phone with a 20-megapixel sensor camera was used to capture the images required for the subsequent study.

Finally, a black blanket was placed on top of the tank to limit the entry of external light and thus reduce interference to a minimum. Figure 3 displays the experimental setup. The grid used and the arrangement of the two pieces of plastic used can be seen. The grid is located at 10 cm distances from the fish tank glass on the horizontal axis. Besides, the homogeneity of the light distribution can be observed by placing a fish tank lamp on top of the tank.

Figure 3. Experimental tank.

B. Methodology

The implementation of the experiment has two phases. The first is based on the experiment itself, where the necessary images are taken. The second is the processing and analysis of these images in order to obtain the different histograms of these images and to be able to differentiate between the grid and the plastic bag in different conditions.

For the first phase of the experiment, images are taken of a grid with two pieces of a plastic bag at different distances and with different turbidity. To do this, we start by filling the tank with 37 L of tap water at a height of 18.5 cm to 6 cm from the top edge of the tank. Then we introduce the grid with the plastic bags. The images are always taken from a fixed point, from the side of the tank. In addition, each round of images is captured while a black blanket to block outside light permanently covers the tank. Photographs are taken by placing the grid at 10cm from the camera. This is repeated in triplicate, with 0 g of soil, 5 g of soil and 10 g of soil to increase turbidity.

Once the images have been obtained, we start with the second phase. In this part, the images obtained are processed and analysed. For this, we use the Matlab software [14] with which we can acquire different histograms in red, green, and blue. Figure 4 presents pseudocode used in the programming process of the images, obtaining the histograms of different colours, as well as the tables with their respective data.

To obtain the necessary information, we choose 3 bag sections and another 3 pieces of the grid from each image and we introduce them into the software. Matlab generates three histograms in red, green, and blue for each section of the image entered, with their respective data. Once these histograms are obtained, we put them together to obtain the different ranges of pixel values for bag and grid, in order to differentiate between them. Figure 5 presents the image where the grid is 20 cm from the camera. Image a) displayed picture without soil and b) image represents water with 10 g of soil to increase the turbidity. It can be seen how the pockets begin to diffuse and start to look like part of the grid.

V. RESULTS

In this section, the results obtained after treating the images with the Matlab software are presented. The different histograms for each image are evaluated to verify the ranges of pixel values for the bag or grid.

A. The image at 10 cm from the camera

Figure 6 displays the histograms obtained from the image captured at 10 cm from the camera, without turbidity. Section a) represents the blue histogram, b) the green histogram and c) the red histogram. Besides, each of them shows the graphical representation of three pieces of the bag (in reddish colours) and three pieces of grids (in bluish colours). It can be seen that in the three histograms, it is easy to differentiate in which pixels and values the grid or bag is

located. The most representative graph is c) where we can find the presence of grid between pixel values from 1 to 90 and from 91 to 190 for the presence of pockets. The maximum pixel percentage for grids is 4 % and 5.3 % for the bag. The results show a noticeable difference between the grid and the plastic bags, as the pixel values are different in the different pixel ranges. These results show that in non-turbidity conditions, the system is able to differentiate between the two objects.

B. Imagen at 10 cm from the camera with 5 g of soil.

In the case of Figure 7, it represents the values obtained for the blue, green, and red band of the image at 10 cm from the camera with 5 g of soil added to the water. Section a) represents the blue histogram, b) the green histogram and c) the red histogram. In addition, each of them shows the graphical representation of three pieces of the bag (in red colours) and three pieces of grids (in blue colours). It can be seen that in the three histograms, it is hard to differentiate in which pixels and values the grid or bag is located. In this, case the best section is the b) with the green band. We can observe that parts of grids 2 and 3 can be distinguished from the presence of bags. The presence of the grid is located between the values 55 to 105, with a maximum pixel percentage of 3%. The results show that the system is able to differentiate some pieces of bag. This is because the turbidity, together with the dark edges of the tank, could have caused interference in differentiating between the objects.

C. Imagen at 10 cm from the camera with 10 g of soil.

Figure 8 represents the values obtained for the blue, green, and red band of the image at 10 cm from the camera with 10 g of soil added to the water. Section a) represents the blue histogram, b) the green histogram and c) the red histogram. In addition, each of them shows the graphical representation of three pieces of the bag (in red colours) and three pieces of grids (in blue colours). It can be seen that in the three histograms, it is hard to differentiate in which pixels and values the grid or bag is located. In this, case the best section is the b) with the green band. We can observe that parts of grids 2 and 3 can be distinguished from the presence of bags. The presence of the grid is located between the values 109 to 163, with a maximum pixel percentage of 12.5%.The results show that at higher turbidity the system starts to have difficulties in differentiating between different objects. In addition, the reflections produced by the tank used produce more interference.

```
Function [Hist_RED, Hist_GREEN, Hist_BLUE,] = Read_Comp_Image
(Comp_RE, Comp_GR, Comp_BL, Col, Row]
//Calcule Histogram Red
Repeat
        vector_RE [i]=0   // Create_vector_RED
Up to (i=256)
Repeat
        Repeat
                Read Value= Comp_RE
                vector_RE [i]= Value
                Comp_RE++
        Up to (Column == end)
Up to (Row == end)

//Calcule Histogram Green
Repeat
        vector_GR [i]=0   // Create_vector_GREEN
Up to (i=256)
Repeat
        Repeat
                Read Value= Comp_GR
                vector_GR [i]= Value
                Comp_GR++
        Up to (Column == end)
Up to (Row == end)
```

Figure 4. Pseudocode used to get RGB histograms.

Figure 5. a) Grid 20 cm from the camera; b) Grid 20 cm from the camera

with 10 g of soil added to the water;
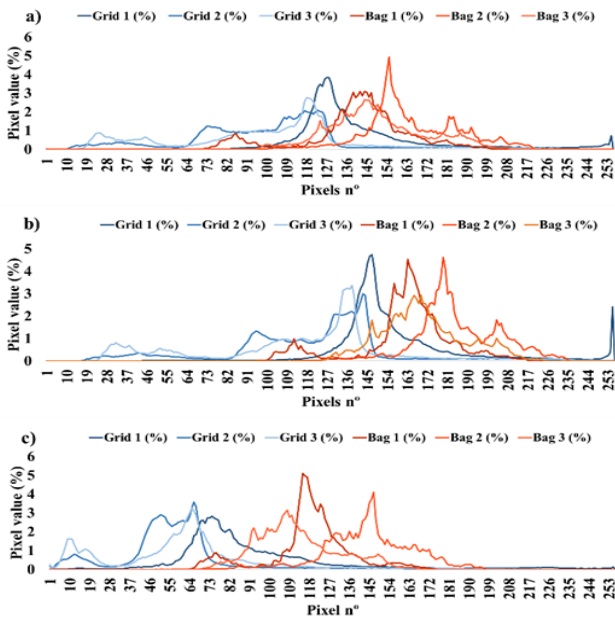
Figure 6. a) Histogram of the blue band at 10 cm; b) Histogram of the green band at 10cm; c) Histogram of the red band at 10cm.
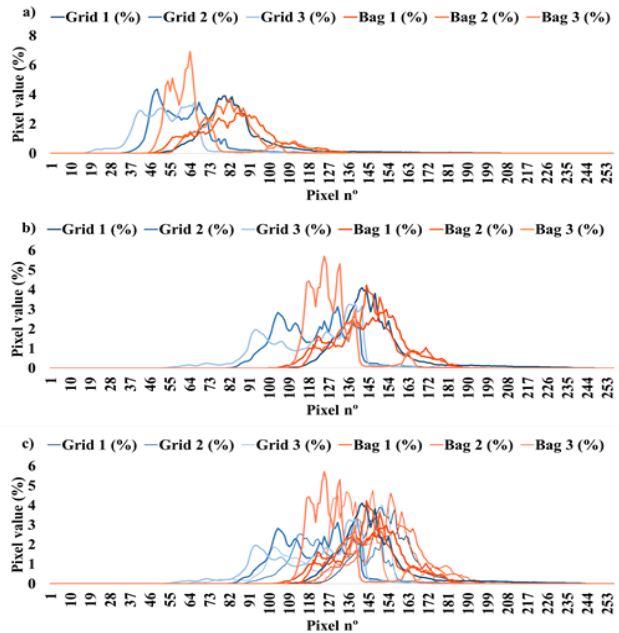
Figure 7. a) Histogram of the blue band at 10 cm with 5 g of soil; b) Histogram of the green band at 10cm with 5 g of soil; c) Histogram of the red band at 10cm with 5 g of soil.
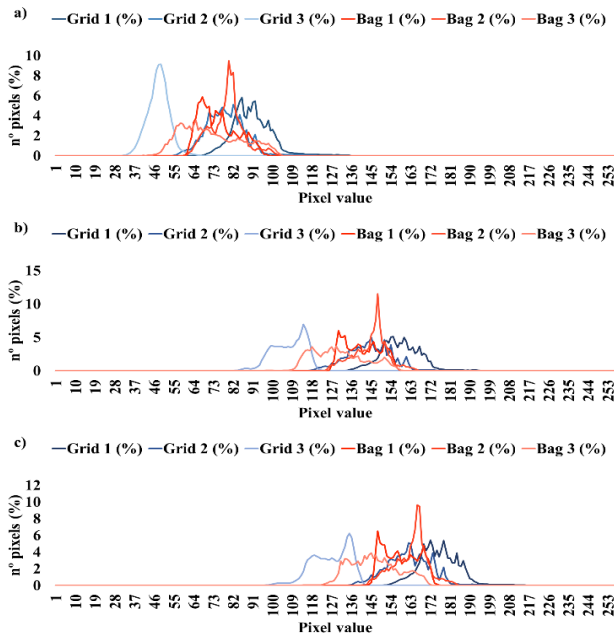
Figure 8. a) Histogram of the blue band at 10 cm with 10 g of soil; b) Histogram of the green band at 10cm with 10 g of soil; c) Histogram of the red band at 10cm with 10 g of soil.

Figure 9. a) Analysis of image at 10cm with 0g of soil; b) Verification Analysis of image at 10cm with 0g of soil.

VI. VERIFICATION

To determine the effectiveness of the developed system, we conducted a verification. For this purpose, the image at a distance of 10 cm without added soil is used. New sections of the image are taken and their values are obtained. Figure 9 shows the differences between the grid and the bag. Section a) represents the values taken in the experiment, where it can be seen that the percentage of pixels above the 5% limit are considered part of the grid and below the bag. Graph a) displays that the grids show a maximum pixel % of 74.8% in

grid 2, and a maximum pixel % of bags of 0.02%. In addition, section b) represents the verification performed, taking other different pieces of grid and bag. This graph shows a maximum pixel % of 84.08% in grid 2 and a maximum pixel % of bags of 0.09%.

The results demonstrate the similarity of the data, showing the presence of grating above 5 % of the number of pixels.

VII. CONCLUSION AND FUTURE WORK

The presence of plastics in the agricultural irrigation system represents a major problem due to the possible outlines produced in the grids of the same, producing a decrease in the irrigation flow, as well as the need for control in situ for its solution.

In this paper, we propose a system to monitor the presence of plastics in the gratings used in irrigation channels for agriculture. We have determined that it is possible to differentiate between bags and the grid up to 5g of added soil. It has additionally been found that at higher turbidity the results are not optimal due to the dark edges and reflections possibly produced by the fish tank. The proposed system is based on the application of artificial intelligence, being of great help, in this case, to be able to differentiate and learn about the presence or absence of plastics in the grid.

In future work, we want to test at different distances. We will extend the number of objects to be detected. In addition, we will use leaves and other types of waste to perform the experiment, to provide to our system more information about the different objects that could be presents in irrigation channel grids.

REFERENCES

[1] J. Manzoor, M.. Sharma, I. R. Sofi, and A. A. Dar, "Plastic Waste Environmental and Human Health Impacts", Handbook of Research on Environmental and Human Health Impacts of Plastic Pollution, IGI Global, pp. 29-37, 2020.

[2] R. Geyer, J. R. Jambeck, and K. L. Law, "Production, use, and fate of all plastics ever made", vol.3, no 7, pp. e1700782, July 2017, doi: 10.1126/sciadv.1700782.

[3] J. Yates et al. "A systematic scoping review of environmental, food security, and health impacts of food system plastics",Nature Food, vol 2, no. 2, pp. 80-87, February 2021, doi: https://doi.org/10.1038/s43016-021-00221-z.

[4] D. Zhang et al., "Plastic pollution in croplands threatens long‑term food security", Global change biology, vol. 26, no.6, pp. 3356-3367, April 2020, doi: https://doi.org/10.1111/gcb.15043.

[5] S. M. Markland, D. Ingram, K. E. Kniel, and M. Sharma, "Water for agriculture: the convergence of sustainability and safety", Preharvest food safety, pp. 143-157, April 2018, doi: https://doi.org/10.1128/9781555819644.ch8.

[6] K. Topouzelis, A. Papakonstantinou, and S. P. Garaba, "Detection of floating plastics from satellite and unmanned aerial systems (Plastic Litter Project 2018)", International Journal of Applied Earth Observation and Geoinformation, vol. 79, pp. 175-183, July 2019, doi: https://doi.org/10.1016/j.jag.2019.03.011.

[7] S. P. Garaba et al., "Sensing ocean plastics with an airborne hyperspectral shortwave infrared imager", Environmental science & technology, vol. 52, no 20, pp. 11699-11707, 2018, doi: http://dx.doi.org/10.1021/acs.est.8b02855.

[8] L. Biermann, D. Clewley, V. Martinez-Vicente, and K. Topouzelis, "Finding plastic patches in coastal waters using optical satellite data", Scientific reports, vol. 10, no 1, pp. 1-10, April 2020, doi: https://doi.org/10.1038/s41598-020-62298-z.

[9] A. H. Iri et al., "Optical detection of microplastics in water", Environmental Science and Pollution Research, pp. 1-7, January 2021, doi: https://doi.org/10.1007/s11356-021-12358-2.

[10] P. Vriend, C. et al. "Rapid assessment of floating macroplastic transport in the Rhine", Frontiers in Marine Science, vol.7, pp.10, January 2020, doi: https://doi.org/10.3389/fmars.2020.00010.

[11] C. van Lieshout, K. van Oeveren, T. van Emmerik, and E. Postma, "Automated river plastic monitoring using deep learning and cameras", Earth and space science, vol. 7, no 8, pp. e2019EA000960, July 2020, doi: https://doi.org/10.1029/2019EA000960.

[12] M. Moshtaghi, E. Knaeps, S. Sterckx, S. Garaba and D. Meire, "Spectral reflectance of marine macroplastics in the VNIR and SWIR measured in a controlled environment", Scientific Reports, vol. 11, no 1, pp.1-12, March 2021, doi: https://doi.org/10.1038/s41598-021-84867-6.

[13] S. Sendra, L. Parra, V. Ortuño, J. Lloret, and U. P. De Valencia, "A low cost turbidity sensor development", Proceedings of the Seventh International Conference on Sensor Technologies and Applications (SENSORCOMM 2013), Spain 2013, pp. 25-31.

[14] MatLab. [Online]. Available from: https://www.mathworks.com/products/matlab.html. [Retrieved: May, 2021]

Scalable Video Streaming over Multi-RAT Network

Jounsup Park
Department of Electrical Engineering
The University of Texas at Tyler
Tyler TX, USA
jpark@uttyler.edu

Abstract— **Efficient utilization of wireless resources is becoming more important with increasing data traffic being over wireless networks, especially multimedia traffic. Since the display panels in mobile devices are getting bigger and having a higher resolution, video streaming over a wireless network becomes a more challenging problem. Multiple Radio Access Technology (Multi-RAT) system is one of the solutions for streaming high-quality video through wireless channels since most mobile devices are equipped with multiple radio technologies, such as Wi-Fi and LTE. Moreover, scalable video is suitable to adaptively change the quality of the video depends on the wireless channel condition. In this research, optimal rate distribution through the Wi-Fi and the LTE will be derived to efficiently utilize both wireless technologies to transmit video to provide the best video quality to the user equipped with Wi-Fi and LTE.**

Keywords- Multi-RAT, SVC, integer programming.

I. INTRODUCTION

The Multi-RAT system can achieve a high data rate by using multiple data paths [1][2]. Long-Term Evolution (LTE) technology allows users to use both licensed and unlicensed spectrum to transmit data. When the licensed channels are congested because of a large number of users, LTE can off-load its data to an unlicensed spectrum. There are two ways to offload the data to an unlicensed spectrum. First, License Assisted Access (LAA) utilizes unlicensed spectrum by aggregate licensed spectrum and unlicensed spectrum. In this case, LTE users occupy a certain amount of unlicensed spectrum. Second, LTE can transmit its data over an unlicensed spectrum using Wi-Fi protocol. LTE users should fairly compete with Wi-Fi users in this case. We design our Multi-RAT system based on the second option because it fairly shares the unlicensed spectrum with Wi-Fi users. Figure 1 shows the overall system architecture transmitting Scalable Video Coded (SVC) video through Wi-Fi and Long-Term Evolution (LTE) channel [3]. First, the source video is coded, and it will be separated as multiple video layers which are composed of a single base layer and several enhancement layers. Second, depending on the channel quality, we will decide the number of layers to be transmitted. Third, the bit streams will be distributed to Wi-Fi and LTE channels to provide the best video quality to the user. Since the channel characteristics of Wi-Fi and LTE are different, the channel characteristics will be used to decide what portion of the data will be transmitted through the Wi-Fi and LTE, respectively.
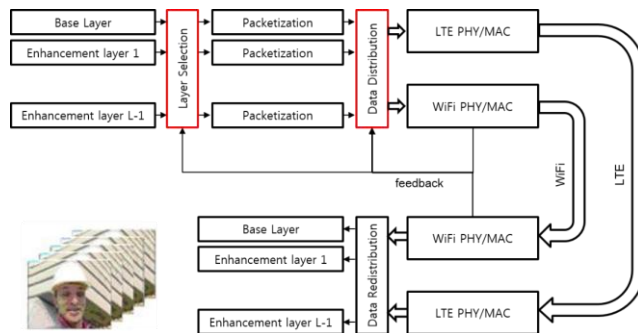
Figure. 1**.** The proposed SVC video streaming system.

The rest of the paper is structured as follows. In section II, we present a problem formulation. Section III presents a problem-solving strategy. Section IV presents simulation results and Section V concludes the paper.

II. PROBLEM FORMULATION

Peak Signal-to-Noise Ratio (PSNR) is the most popular way to measure the Quality of Experience (QoE) for video. However, in wireless communication settings, the receiver has no information about the original video and cannot measure the PSNR while still receiver also need to measure the QoE to adaptive rate control to efficiently utilize the wireless resource. Since SVC video has several data streams, receiver can estimate the QoE by counting the number of video layer successively received. For example, if the receiver has 4-video layers, then it will have better video quality than the receiver having 3-video layers. Therefore, this project focused to maximize the number of layers.

The optimization problem can be formulated as (1), which is maximizing utility function subject to the data rate constraint (2)~(5) of LTE and Wi-Fi channels. Defined utility is summation of all the layer's estimated utilities successfully received, where *u* is the QoE model from [4]. LTE and Wi-Fi have different PHY and MAC layer design, but both technologies are using OFDM as a fundamental data allocation. Therefore, we can estimate the throughput of each channel by using the number of sub-carriers allocated for the user in our interest.

$$\max_{r_{LTE}, r_{WiFi}} U(r_{LTE}, r_{WiFi}) = \sum_{l=0}^{L-1} u_l f_l(r_{LTE}, r_{WiFi}) \qquad (1)$$

subject to

$$\sum_{l=0}^{L-1} r_{l,WiFi} \le (k_{WiFi} - k_{ov}) \frac{B_{WiFi}}{k_{WiFi}T}, \quad \sum_{l=0}^{L-1} r_{l,LTE} \le \frac{B_{LTE}}{T}, \quad (2)$$

$$r_l \le r_{l,LTE} + r_{l,WiFi}, \text{ for } l = 0,...,L-1, \quad (3)$$

$$f_l(r_{LTE}, r_{WiFi}) = \prod_{k=0}^{l} corr_{LTE} corr_{WiFi}, \quad (4)$$

$$corr_{LTE} = (1 - P_e(\gamma_{LTE}, M_{LTE}))^{ceil\left(\frac{r_{k,LTE}T}{\log_2 M_{LTE}}\right)}$$
$$corr_{WiFi} = (1 - P_e(\gamma_{WiFi}, M_{WiFi}))^{ceil\left(\frac{r_{k,WiFi}T}{\log_2 M_{WiFi}}\right)}, \quad (5)$$

u_l is the utility of l-th layer, L is the total number of video layers, T is symbol duration, $B_{LTE/WiFi}$ is the number of bits allocated to LTE and Wi-Fi channels, $\lambda_{LTE/WiFi}$ is received SNR of LTE and Wi-Fi, $M_{LTE/WiFi}$ is a modulation size of LTE and Wi-Fi, $k_{LTE/Wi-Fi}$ is the number of sub-channels in LTE and Wi-Fi spectrum, k_{ov} is the overhead for Wi-Fi channel to avoid collisions, $corr_{LTE/Wi-Fi}$ is the correction rate of LTE and Wi-Fi channels.

III. PROBLEM SOLVING

To solve the optimization problem, logarithm is taken to simplify the problem. Then, the problem turns out to be the integer linear programming problem. We can relax the problem to a general linear programming problem and rounding the result to get the integer results.

$$\bar{f}_l(N^k{}_{LTE}, N^k{}_{WiFi}) = \log f_l(r_{LTE}, r_{WiFi})$$
$$= \sum_{k=0}^{l} \alpha_{LTE} N^k{}_{LTE} + \alpha_{WiFi} N^k{}_{WiFi} \quad (6)$$

where,

$$N^k_{LTE} = ceil\left(\frac{r_{k,LTE}T}{\log_2 M_{LTE}}\right), N^k_{WiFi} = ceil\left(\frac{r_{k,WiFi}T}{\log_2 M_{WiFi}}\right)$$
$$\alpha_{LTE} = \log(1 - P_e(\gamma_{LTE}, M_{LTE}))$$
$$\alpha_{WiFi} = \log(1 - P_e(\gamma_{WiFi}, M_{WiFi})) \quad (7)$$

A new problem statement is

$$\max_{N_{LTE}, N_{WiFi}} \bar{U}(N_{LTE}, N_{WiFi}) = \sum_{l=0}^{L-1} u_l f_l(N_{LTE}, N_{WiFi}) \quad (8)$$

subject to

$$\sum_{l=0}^{L-1} N_{l,WiFi} \le \frac{k_{WiFi} - k_{ov}}{k_{WiFi}} N_{WiFi}, \sum_{l=0}^{L-1} N_{l,LTE} \le N_{LTE} \quad (9)$$
$$r_l \le r_{l,LTE} + r_{l,WiFi}, \text{ for } l = 0,...,L-1$$

The problem is restated using standard form of the Linear Programming described as [5]

α	LTE (0.9)	WiFi (0.9)	α	LTE (0.9)	WiFi (0.9)	α	LTE (0.8)	WiFi (0.9)
Base	12	49	Base	15	46	Base	1	60
Layer1	7	26	Layer1	8	25	Layer1	1	33
Layer2	2	9	Layer2	3	8	Layer2	1	10
Layer3	5	18	Layer3	6	17	Layer3	4	19
(a) No overhead			(b) $K_{ov} = 10$			(c) $K_{ov} = 10$		

Figure 2. Packet Distribution
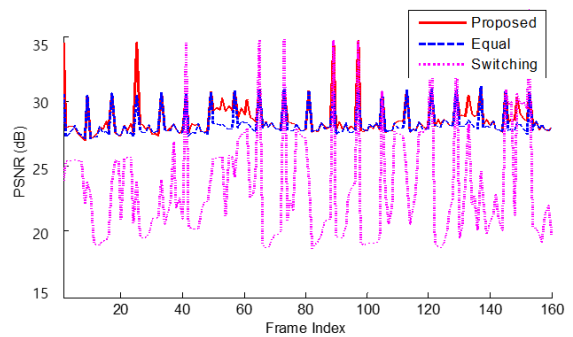
Figure 3. PSNR (dB) Performance

$$\max_{x} f^T x \quad (10)$$
$$\text{subject to } Ax \le b, \ x \ge 0, \text{ and } x \in Z^n$$

where,

$$f^T = \left[\sum_{l=0}^{L-1} \alpha_{l,LTE} u_l \quad \sum_{l=0}^{L-1} \alpha_{l,WiFi} u_l \quad \cdots \quad \alpha_{0,LTE} u_0 \quad \alpha_{0,WiFi} u_0 \right] \quad (11)$$

$$x = \left[N_{LTE}^0 \quad N_{LTE}^0 \quad \cdots \quad N_{LTE}^{L-1} \quad N_{LTE}^{L-1} \right]^T \quad (12)$$

$$A = \begin{bmatrix} 1 & 0 & 1 & 0 & 1 & 0 & 1 & 0 \\ 0 & 1 & 0 & 1 & 0 & 1 & 0 & 1 \\ -1 & -1 & 0 & 0 & 0 & 0 & 0 & 0 \\ 0 & 0 & -1 & -1 & 0 & 0 & 0 & 0 \\ 0 & 0 & 0 & 0 & -1 & -1 & 0 & 0 \\ 0 & 0 & 0 & 0 & 0 & 0 & -1 & -1 \end{bmatrix} \quad (13)$$

IV. SIMULATION RESULTS

Matlab and Joint Scalable Video Model (JSVM) software [6] were used to evaluate the proposed algorithm. Fig 2. shows the simulation results with different settings. We assume that the available number of resources are $N_{LTE} = 30$ and $N_{WiFi} = 120$. Fig 2(a). shows the packet distribution results with no overhead, where the overhead K_{ov} means required amount of resource to avoid collision in Wi-Fi network. Fig 2(b) shows the packet distribution when the overhead $K_{ov} = 10$, which is the case that Wi-Fi cannot fully utilize its resource to avoid congestion. Fig 2(c) shows the packet distribution when the channel condition of LTE is worse than the channel condition of Wi-Fi. The

simulation results show that the proposed algorithm allocates more video packets to more reliable network.

For the comparison, equal data distribution and switching algorithm were also implemented. Equal data distribution only distributes the data to two channels with the same data rate. The switching algorithm selects the one channel which has better channel gain than other. Fig 3. shows that the proposed algorithm has the best PSNR.

V. CONCLUSION

Multi-RAT is a useful technology for streaming videos, since it can achieve better data rate than using only one channel at once. Moreover, if we distribute the data in an optimal way, the receiver will get better quality video. We proposed the optimal solution for data distribution between LTE and Wi-Fi and found that the proposed scheme can provide better quality video. The proposed algorithm will be expanded to 5G license assisted access (LAA) as a future work.

REFERENCE

[1] R. Zhang, M. Wang, L. X. Cai, Z. Zheng, X. Shen, and L.-L. Xie, "LTE-unlicensed: The future of spectrum aggregation for cellular networks," IEEE Wireless Communications, vol. 22, no. 3, pp. 150–159, Jun. 2015.

[2] O. Galinina, A. Pyattaev, S. Andreev, M. Dohler, and Y. Koucheryavy, "5G multi-rAT LTE-WiFi ultra-dense small cells: Performance dynamics, architecture, and trends," IEEE Journal on Selected Areas in Communications, vol. 33, no. 6, pp. 1224–1240, Jun. 2015.

[3] J. Park, "Video Streaming over the LWA Systems," International Conference on Computing, Networking and Communications (ICNC), 2019, pp.597-601, doi: 10.1109/ICCNC.2019.8685626.

[4] Z. Ma, M. Xu, Y-F. Ou, and Y. Wang, "Modeling of rate and perceptual quality of compressed video as functions of frame rate and quantization stepsize and its applications", IEEE Transactions on Circuits and Systems for Video Technology, vol. 22 no. 5, pp. 671-682, Nov. 2011.

[5] S. Boyd, and L. Vandenberghe, Convex Optimization, Cambridge University Press 2004.

[6] JSVM Software Manual. 2006. Available online: http://scholar.google.com/scholar?hl=en&btnG=Search&q=in title:JSVM+ Software+Manual#0 (accessed on 15 March 2021).

On Security and Energy Efficiency in Underwater Wireless Sensor Networks for Maritime Border Surveillance

Seungmo Kim*
*seungmokim@georgiasouthern.edu
Department of Electrical and Computer Engineering
Georgia Southern University
Statesboro, GA, USA

Abstract—Underwater wireless sensor networks (UWSNs) based on acoustic communications attract interest as an enabling technology of maritime border surveillance. However, due to differences in environments, many of the techniques used in typical terrestrial wireless communications are not directly applicable to UWSNs. Of the challenges, designing a secured and energy-efficient UWSN takes the greatest significance for application to maritime surveillance applications. To provide an overview on the UWSN technology, this paper (i) characterizes key technical challenges that are drawn in UWSNs and (ii) discusses methodologies to improve security and energy efficiency of an UWSN.

Index Terms—Underwater acoustic communications; UWSN; Security; Energy efficiency

I. INTRODUCTION

Underwater wireless sensor networks (UWSNs) contain several components such as vehicles and sensors that are deployed in a given geographic area to perform collaborative monitoring and data collection tasks. Today, the UWSN has become a key wireless communication technology that can be used for a wide range of homeland security applications including tactical surveillance, offshore exploration, monitoring of subsea machinery such as oil-rigs and pipelines.

A. Challenges

Nonetheless, it is still a daunting task to establish a stable UWSN due to several key challenges. Focusing on maritime border surveillance applications, we identify the following two challenges particularly important to revolve.

1) Challenges in Security: First, *time synchronization* is important in several underwater applications resembling coordinated sensing tasks. Also, programming algorithms resembling time division multiple access (TDMA) need precise temporal order between nodes to regulate their sleep-wake up schedules for power saving. Achieving precise time synchronization is particularly tough in underwater environments because of the characteristics of UWSNs.

Second, *localization* could be a vital issue for detection and sharing the sensed knowledge. Nevertheless, the localization techniques built for ground-based wireless networks cannot be directly be applied to the underwater underwater environment because of the aforementioned unique challenges. Hence, more concern should be given to the architecture of underwater wireless networks.

2) Challenges in Energy Efficiency: With UWSN protocol designs, saving energy is a major concern, especially for long-term aquatic monitoring and sensing applications and due to its node mobility, most of the energy-efficient protocols designed for terrestrial wireless networking are not feasible [5].

B. Contribution of This Paper

As a survey, this paper describes the present-day techniques to address the challenges. We provide an extensive investigation on the system model–*i.e.*, path loss, noise, multi-path, and Doppler spread–in order to draw accurate analyses subsequently. Accounting the system model, we study the methodologies to improve *security* and *energy efficiency*–the two aspects that this paper identifies as the key challenges in operation of maritime border applications.

II. SYSTEM MODEL

The key rationale that we put a particular significance on an accurate characterization of a UWSN system model is as follows. UWSN and terrestrial wireless systems share common properties but they have critical differences, which is attributed to the communication medium.

It is less efficient for UWSNs to use radio frequency (RF) signals since they have an enormous attenuation in the subaquatic medium. Therefore, acoustic signals are more commonly used in underwater communications scenarios [1].

Acoustic communication regarding underwater environment is a complex phenomenon because a lot of environmental factors affect acoustic communication. These factors vary including long propagation delays, environmental noise, path loss, Doppler spread, and multipath effect.

A. Path Loss

When sound propagates from underwater environment then some of its strength converts into heat. Sound wave propagation energy loss can be categorized into three main categories [2]:

1) *Geometric Spreading Loss:* When source generates acoustic signal it propagates away from the source in the form of wave fronts. This loss is independent of frequency, while only depends on the distance.
2) *Attenuation:* Within acoustic communication, the most common attenuation appears as conversion into heat.

The level of attenuation is directly proportional to frequency and distance.

3) *Scattering Loss:* This type of loss occurs at the surface of the water. Surface roughness is usually generated by the wind, which in turn changes the pattern of scattering. Scattering at the surface of the water causes power losses of acoustic signals.

B. Noise

Types of underwater noise are two-fold [2]. First, noise can generated by *humans* while operating various activities from use of underwater machines to shipping and fishery. Second, *ambient noise* is generated by a combination of different sources that are often impossible to identify [3]. Underlying noise is considered as thermal noise in the absence of all other sources of noise, including self-noise. Thermal noise is directly proportional to the frequency which is used for acoustic communication.

C. Multipath

In terrestrial wireless communications, a multipath effect is well known to cause delay spread in a signal, which in turn cause an inter-symbol interference. In underwater acoustic communications, number of propagation paths, propagation delays, and its strength are determined by the acoustic channel impulse response that is determined by the geometry. For instance, in deep oceans, refraction of sound occurs because of variable sound speed that cases of multipath effect in acoustic channel. On the other hand, sound propagation in shallow water is influenced by surface reflections while deep water propagation is affected by bottom reflection that becomes cause of large and variable communication delay in acoustic communication.

D. Doppler Spread

In underwater environments, just as in terrestrial wireless communications scenarios, there also are relative spatial movement among a transmitter, a received, and obstacles in the middle of a communications path, which causes Doppler shift. The subsequent impact is the same to be the frequency offset.

III. SECURITY AND ENERGY EFFICIENCY IN UWSN

A. Security

We identify the key attack types and understand them in UWSN's perspectives as follows.

1) *Jamming:* A jamming attack is a type of denial of service (DoS) attack, which prevents other nodes from using the channel to communicate by occupying the channel that they are communicating on. UWSNs area unit prone to narrowband electronic jamming due to the narrowband nature of acoustic communications.

In terrestrial networks, when a jamming is detected, the sensors are quickly able to report the intrusion to other nodes in order to re-route the packets around the impacted area. However, it is not trivial to apply this resolution to UWSNs mainly due to 'sparse deployment' of nodes in underwater

scenarios. In other words, there usually are not enough sensors to provide a detour and to re-route traffic around the jammed area. Another resolution projected for ground-based detector networks against electronic countermeasures is to use various technologies for communication resembling in fared or optical. However, this resolution can't be applied either, since optical and infrared waves square measure severely attenuated below water.

2) *Wormhole Attack:* A wormhole attack is known to severely destroy the performance of an ad-hoc network [4]. In a wormhole attack, an attacker records packets (or bits) at one location in the network, tunnels them (possibly selectively) to another location, and retransmits them there into the network. For example, most existing ad hoc network routing protocols, without some mechanism to defend against the wormhole attack, would be unable to find routes longer than one or two hops, severely disrupting communication.

One methodology for detection of a wormhole attacker in terrestrial networks is based on estimation of the physical distance between two nodes as the key indicator of the "neighborship." However, the correct estimation of a distance depends on precise localization and tight clock synchronization. In underwater communications, both of them become extremely challenging.

3) *Sybil Attack:* In a sybil attack, a node in the network operates multiple identities actively at the same time and undermines the authority/power in reputation systems. The main aim of this attack is to gain the majority of influence in the network to carry out illegal (with respect to rules and laws set in the network) actions in the system. To outside observers, these multiple fake identities appear to be real unique identities.

Again, designing a countermeasure against a sybil attack in an UWSN is challenging because of the difficulty in precise localization of an underwater node. Specifically, authentication and position verification are efficient countermeasures against a sybil attack; yet the accurate position verification becomes difficult in an UWSN due to challenges in communications introduced in Section II.

B. Energy Efficiency

Since most of the underwater sensors operate on battery powers, it is essential for maritime surveillance to design an UWSN that is energy-efficient.

One popular method that can be applied to UWSN is packet size optimization. Again, selection of a packet size becomes more challenging in an UWSN due to wider variations of environmental factors. Moreover, due to the movement of sensor nodes under the influence of ocean currents, collection of information among a wide enough network also becomes an issue. This 'myopic' sight on a network hinders a faster dissemination of knowledge on 'link costs' over an entire network, which in turn causes a higher delay in routing.

IV. CONCLUSIONS

Today, UWSN has garnered a staggering amount of attention in the research society for the homeland security. How-

ever, when compared to terrestrial wireless sensor networks, the UWSN presents one with an intricate complexity. This study identified *security* and *energy efficiency* as the major factors to resolve in design of an UWSN. Then, it went on discussing the particular reasons that the UWSN makes it more difficult to address the two goals. This work can form the basis for further research in designing novel algorithms for managing a large number of nodes in an UWSN. It will further show a significant contribution to securing the nation's land/maritime borders.

REFERENCES

[1] S. Jiang, "On securing underwater acoustic networks: a survey," *IEEE Commun. Surveys Tut.*, vol. 21, iss. 1, 2019.

[2] P. Amoli, "An overview on researches on underwater sensor networks: applications, current challenges and future trends," *Int. J. Electr. Comput. Eng.*, vol. 6, no. 3, Ju. 2016.

[3] A. Manigopal and R. Panneerselvam, "Underwater wireless sensor networks: a survey," *Int. J. Comput. Sci. Inf. Technol. Security*, vol. 2, iss. 6, 2012.

[4] Y. Hu, A. Perrig, and D. Johnson, "Wormhole attacks in wireless networks," *IEEE J. Sel. Areas Commun.*, vol. 24, iss. 2, Feb. 2006.

[5] H. Choudhary, "Challenges of underwater wireless communications networks," [Online] Available: https://dspcommgen2.com/ challenges-of-underwater-wireless-communications-networks/, Accessed on May 14, 2019.

Simulations for Stochastic Geometry on the Performance of V2X Communications in Rural Macrocell Environment

Victor Obi* and Seungmo Kim*

*{vo00840,seungmokim}@georgiasouthern.edu

Department of Electrical and Computer Engineering

Georgia Southern University

Statesboro, GA, USA

Abstract—Vehicle-to-everything (V2X) communications is a concept that has been around for the past decade. It involves communication between vehicles and other types of infrastructure. This application is exceptionally useful for emergency services such as ambulances, fire trucks etc. This is because an emergency vehicle can communicate with the traffic light infrastructure and make it give the green signal thereby allowing vehicle to pass quickly. This is useful because it alerts other cars and pedestrians on the road when an emergency vehicle is present. In this paper, a V2X communications system in an urban setting will be simulated using MATLAB and the Automated Driving Toolbox. The purpose of simulation in MATLAB is to test if vehicle to vehicle communication is affected by buildings and other infrastructure. The first Simulation is constructed using the Automated driving simulator. In this simulation clover highway is constructed and cars are added to mimic a busy highway. The second simulation involves several nodes being programmed in MATLAB and intersecting at various points to simulate an overpass highway. The end goal of this project to successfully simulate a V2X communications system with additional components added within the program to represent additional cars and infrastructure.

Index Terms—Stochastic geometry, V2X, Rural macrocell, Suburban highway

I. INTRODUCTION

The purpose of this paper is to construct a clover highway with vehicles on all roads and have movement by the cars on all junctions. The project will be accomplished using MATLAB and the toolboxes associated with it. Through this project we will simulate vehicle-to-everything communications (V2X) communications which stands for vehicle to everything communications. There are several components to V2X, which include Vehicle to vehicle (V2V), vehicle to infrastructure (V2I), vehicle to pedestrian (V2P), vehicle to network (V2N), etc. As such, V2X has already taken the notion as a leading driver technology enabling cars to communicate with each other and other external systems (i.e. traffic lights, streetlights, parking garages, pedestrians) [1].

Nevertheless, the V2X communications are at the most critical moment in its history. The main reason is the federal government's movement that favors the Wi-Fi as an effort to meet the burgeoning bandwidth demand. The movement directly affected the spectrum for V2X communications. The spectrum of 5.850-5.925 GHz (also known as the *5.9 GHz band*) was assigned to V2X communications for supporting the intelligent transportation system (ITS) use cases in 1999 by the United States Federal Communications Commission (U.S. FCC). However, after many years of hearing and discussion, the FCC voted in a bipartisan support to reduce the bandwidth for V2X from 75 MHz (5.850-5.925 GHz) to 30 MHz (5.895-5.925 GHz) while granting the remainder of the 5.9 GHz to Wi-Fi [2].

In particular, a V2X communications system has been found to be interference-constrained mainly due to a large communications range for each vehicle [3]. There were two main technologies supporting the V2X communications functionalities, namely the dedicated short-range communication (DSRC) [4][5] and C-V2X [6][7]. Moreover, such an inter-technology interference between dissimilar wireless systems has been studied quite a few times in the litereature [8][9]. Albeit not presented in this paper, our analysis has found that a suburban geometry yielded a higher level of interference because of the *openness* in signal exchange among vehicles. On the other hand, ironically, an urban geometry marked a lower level of interference among vehicles due to existence of *blockage* provided by physical obstacles (e.g., buildings). Motivated from this finding, this paper focuses on the performance evaluation of a V2X communications system in a suburban environment.

Contribution of This Paper: This paper provides a suburban highway environment where the performance of a V2X communications can be evaluated. The framework aims to serve as a conceptual basis for further study based on the stochastic geometry, which will more precisely assess the performance of V2X communications in safety-critical use cases. As a means to accommodate a higher level of flexibility in the distribution of vehicles, this study is focused on providing a computer simulations framework.

II. SYSTEM MODEL

Recall from Section I that a suburban environment is of particular significance in the analysis of V2X communications due to a higher interference. As an effort to capture the unique characteristics of a suburban geometry, this paper adopts a *Rural Macrocell (RMa)* environment that is defined in the channel model by the 3rd Generation Partnership Project (3GPP) [10]. Technical details follow in this section.

```
1 -     scenario = drivingScenario;
2
3       %HIGHWAY JUNCTION
4
5       % % Highways
6 -     road(scenario, [-300 -8 0; 300 -8 0], 15); % north
7 -     road(scenario, [-300  8 0; 300  8 0], 15); % south
8 -     road(scenario, [-8 -300 8; -8 300 8], 15); % east
9 -     road(scenario, [ 8 -300 8;  8 300 8], 15); % west
0       %Adding vehicles
1 -       egoVehicle = vehicle(scenario,'ClassID',1, ...
2                                 'Position',[-232 -10 15]);
3 -       egoVehicle2 = vehicle(scenario,'ClassID',2, ...
4                                 'Position',[-229 -5 20]);
5 -       egoVehicle3 = vehicle(scenario,'ClassID',1, ...
6                                 'Position',[-226 -10 15]);
7 -       egoVehicle4 = vehicle(scenario,'ClassID',2, ...
8                                 'Position',[-222 -5 20]);
9 -       egoVehicle5 = vehicle(scenario,'ClassID',1, ...
```
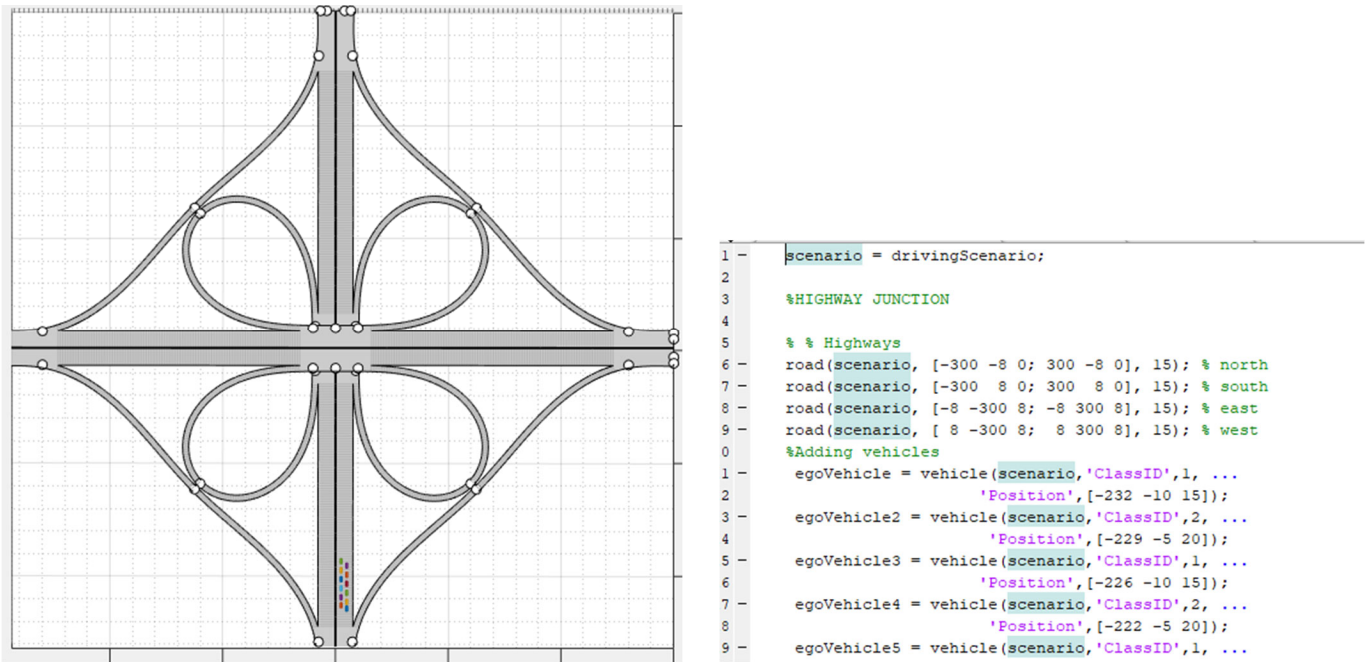
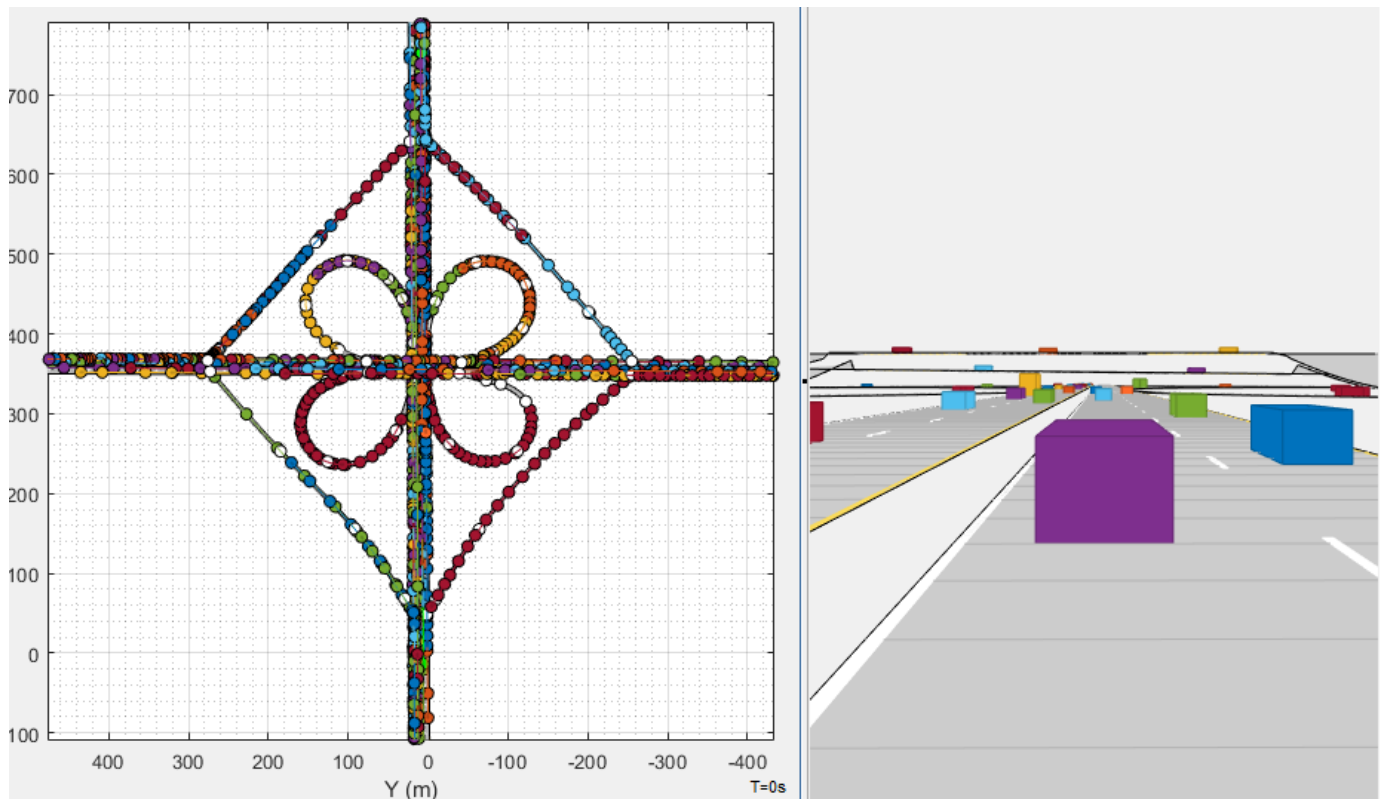Fig. 1. The original approach for the project

Fig. 2. Highway Simulation using automated driving toolbox (The blocks represent the vehicles and the dots represent the paths the vehicles take.)
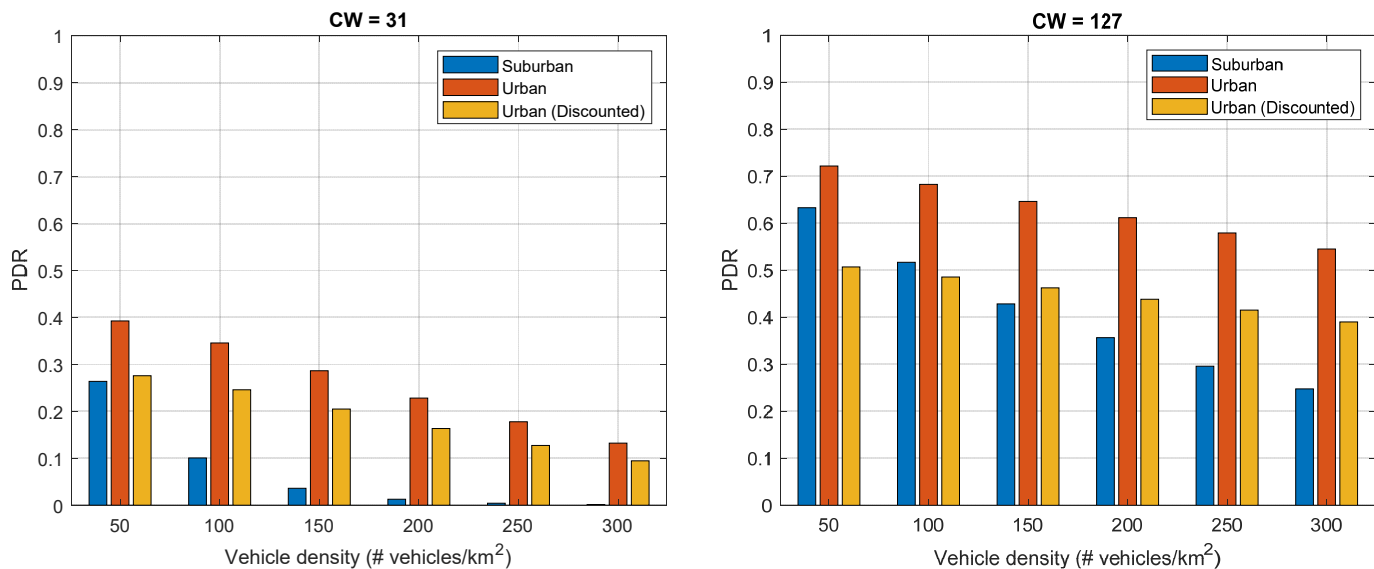
Fig. 3. Comparison of PDR between urban and suburban geometries (with CW = {31, 127})

A. Path Loss

The rural deployment scenario focuses on larger and continuous coverage. The key characteristics of this scenario are continuous wide area coverage supporting high speed vehicles. Several key technical characteristics are provided in the specification [10]:

- *Distribution of nodes:* Uniform
- *Indoor/Outdoor:* 50% indoor and 50% outdoor
- *LOS/NLOS:* Both LOS/NLOS

where LOS and NLOS stand for line-of-sight and non-line-of-sight, respectively.

For the path loss model characterized for the RMa geometry, the readers are encouraged to refer to Table 7.4.1-1 of the specification [10].

B. Geometry

Now, we proceed to creation of geometric models for the RMa. As a representative of the RMa model, we create a suburban environment where two highway segments cross, which forms a 4-way junction. Fig. 1 describes the geometry (on the left) and a snapshot of the MATLAB code implementing the geometry (on the right).

On the created geometry, we move on to distribute vehicles at the density of 100 vehicles per km^{-2}, which is illustrated in Fig. 2. The normalization by km^2 is attributed to the *dimension* of the geometry as shown on the righthand side of Fig. 2. Details on our methodology will follow in the next section.

III. SIMULATIONS METHODOLOGY

This section depicts *why* and *what* we do in the simulations as proposed in the previous section.

A. Justification of Methodology

We found that simulation would accomplish the best efficiency as the main method to evaluate the performance of the proposed mechanism, based on several advantages [11].

First, as presented through Figs. 1 through 2, the parameters defining and operating the proposed study are quite diverse in types and values, which makes it challenging to explore the parameters' dynamic orchestration in concert. A simulation provides a relatively easier control over such a large space composed of various parameters with wide ranges of values. It gives an obvious advantage over mathematical derivations and testbed implementations. One can easily anticipate a high degree of complexity in changing the setting every time a new round of simulation is executed, while a large number of iterations is inevitable to present a statistically stable result in such a complex setting. As an effort to deal with the complexity, we adopt simulation as the main methodology, which, as shall be presented in this section, did efficiently evaluate the proposed system in a wide diversity of parameter settings.

Second, simulations enable computations without being caught up with restrictions or errors caused by computing environmental factors including hardware, compiler, language, etc. Taking into account all the available options for all of those factors will complex the performance evaluation to a too high degree, which, as such, will make it hard to precisely identify the factors determining the key performance.

B. Development of Simulations Framework

During the early stages of the project, there was an attempt to construct the highways in MATLAB programmatically however that proved to be in efficient for the goal in mind (as shown in Fig. 1). The approach for the project was then changed and instead of creating the roads programmatically we

decided to draw it out using the Automated driving toolbox (as seen in Fig. 2). Through use of the automated driving toolbox, the highways were constructed, and the moving vehicles were able to be simulated.

IV. RESULTS

Taking a comparative look at the urban and suburban geometries, we calculate the performance of a V2X network in terms of the packet delivery rate (PDR) as shown in Fig. 3. The figure shows that with CW of 31 and 127, a vehicle can achieve a higher PDR in an urban scenario. The rationale is that that the blockage acts to reduce the number of neighboring vehicles that "compete" for a channel. In other words, in an urban scenario, the receivability among the Rx vehicles not undergoing blockage is higher compared to a suburban setting. The reason is that the blockage also serves as physically dividing a large network into smaller ones.

However, we would not recommend one taking the result in Fig. 3 that an urban setting is more advantageous in the performance of exchanging signals. This is because the PDR is not displaying the number of vehicles that received the BSM. In other words, the physical *coverage* of a message broadcast must be suppressed in an urban setting compared to a suburban scenario where no blockage exists. Therefore, the third bar ("orange" in color) in the figure shows the PDR that is "discounted" by the blockage rate, which gives the number of vehicles that are actually able to receive a BSM after consideration of the blockage.

V. CONCLUSION AND FUTURE WORK

This paper has presented a simulation framework that provides an analytical capability based on the stochastic geometry. The paper has put particular focus on the suburban geometry, in consideration of a higher interference caused by lack of blockage of signals among vehicles. Based on the simulations, this paper has also presented a comparative analysis between the urban and suburban scenarios. The result indicated that a higher PDR could be achieved in an urban setting, but a discount must be applied because the higher performance was achieved only among a certain subset of vehicles due to the blockage.

Moving forward the plan is to add more nodes at various points of the graph and vary the speeds for each node to see how that affects the performance of the simulation. Though certain aspects of the code have been manipulated to help reach the goal of consistency, the plan is to push the boundaries of the code and see what other applications the code can be used in.

REFERENCES

[1] S. Kim, "Impacts of mobility on performance of blockchain in VANET," *IEEE Access*, vol. 7, May 2019.

[2] U.S. FCC, "Use of the 5.850-5.925 GHz band," *FCC-20-164A1_Rcd*, Nov. 2020.

[3] Y. S. Song and S. K. Lee, "Analysis of periodic broadcast message for DSRC systems under high-density vehicle environments," in *Proc. IEEE International Conference on Information and Communication Technology Convergence (ICTC) 2017*.

[4] S. Kim and C. Dietrich, "A novel method for evaluation of coexistence between DSRC and Wi-Fi at 5.9 GHz," in *Proc. IEEE Global Communications Conference (Globecom) 2018*.

[5] S. Kim and B. J. Kim, "Crash risk-based prioritization of basic safety message in DSRC," *IEEE Access*, vol. 8, Nov. 2020.

[6] S. Kim and B. J. Kim, "Reinforcement learning for accident risk-adaptive V2X networking" in *Proc. IEEE Vehicular Technology Conference (VTC) 2020 Fall*.

[7] S. Kim, B. J. Kim, and B. Park, "Environment-adaptive multiple access for distributed V2X network: A reinforcement learning framework," in *Proc. IEEE Vehicular Technology Conference (VTC) 2021 Spring*.

[8] J. Lee, T. Kim, S. Han, and S. Kim, "An analysis of sensing scheme using energy detector for cognitive radio networks," in *Proc. IEEE International Symposium on Personal, Indoor and Mobile Radio Communications (PIMRC) 2008*.

[9] S. Kim and C. Dietrich, "Coexistence of outdoor Wi-Fi and radar at 3.5 GHz," *IEEE Wireless Commun. Lett.*, vol. 6, iss. 4, Aug. 2017.

[10] 3GPP, "5G; Study on channel model for frequencies from 0.5 to 100 GHz (3GPP TR 38.901 version 16.1.0 Release 16)," *ETSI TR 138 901*, v16.0.0, Nov. 2020.

[11] S. Kim and A. S. Ibrahim, "Byzantine-fault-tolerant consensus via reinforcement learning for permissioned blockchain implemented in a V2X network," *arXiv:2007.13957*, Jul. 2020.

High Resolution mmWave Radar by Radar Fusion and Sparse SAR

Thomas Moon

Electrical and Computer Engineering
University of Illinois at Urbana-Champaign
Urbana-Champaign, USA
tmoon@illinois.edu

Abstract—In automotive applications, mmWave radar has been limited to measuring the range of objects. Its limited role comes from two reasons: low resolution in three-dimensional (3D) imaging and blind spot from specularity. A single automotive radar typically has less than 5GHz bandwidth, and therefore its distance resolution is insufficient. By fusing multiple radars operating different frequencies, the total bandwidth of the radar system can be increased. Strong specular effects of mmWave signals cause incomplete or shabby radar images due to few reflected signals. We address the blind spot problem with random spatial sampling, resulting in the ability to reconstruct the radar image with missing reflected signals. Numerical results are used to prove the concept.

Index Terms—FMCW radar; SAR; Compressive Sensing; Autonomous Vehicle.

I. INTRODUCTION

Autonomous Vehicles (AVs) are no longer a dream, but a close reality. Google has been working on self-driving technology since 2009 and begun testing their prototype without a safety driver in 2017 [1]. Major automotive companies, such as Nissan, BMW, Ford, Tesla, GM, have already started testing their AVs and some of them announced a plan to develop commercial AVs in the consumer market by 2020. The recent progress in AVs has been achieved by the cutting-edge technology including advanced control theory, deep learning, sensor technology and so on. Among these advanced technologies, sensors that obtain 3D images of the environment are the first stage and one of the most important processes that enable autonomous driving. Even in today's non-autonomous vehicles, a number of sensors are implemented to assist the driver.

However, fully autonomous vehicles without any driver's intervention require some challenges to be cleared. In 2014, the Society of Automotive Engineers (SAE) published a standard that defines six different levels for vehicles from fully manual (Level-0) to fully automated system (Level-5) [2]. To achieve a Level-5 autonomous vehicle, the vehicle should perform all the driving functions under all roadway and environmental conditions that can be managed by a human driver. In current AVs' sensing system, optical sensors such as Light Detection And Ranging (LiDAR) and camera take a major role for 3D imaging. As both sensors operate at the optical wavelength, they can provide accurate perception in most scenarios. However, their sensing performance is significantly degraded in low visibility conditions such as fog, smog, and snow because the light is scattered before it arrives at the targets in such conditions [3].

In contrast to LiDAR and camera, radar can perform equally well in fog, smog, snow, and dark, as well as in sunny weather. A typical commercial LiDAR and radar system can achieve around 150m range detection and camera can do 300m in the sunny weather. While the camera visibility drops below 100m in the dark and the LiDAR below 50m in fog, smog, and snow, the radar can maintain almost the same performance in any conditions [4]. F In recent years, the automotive industry has started to adapt mmWave radar whose wavelength is much shorter than the conventional radar. This advance provides the radar system a higher resolution image. In addition to the resolution benefits, the size of the radar system is shrunk by the shorter wavelength. With the compact size, forming an array of antenna is feasible and practical.

However, the role of mmWave radar has been limited to measuring the range of the objects in automotive application. Its limited role comes from two reasons: (1) low resolution in 3D imaging, (2) blind spot from specularity. A commercial LiDAR can offer 3D images with the distance accuracy of 2cm, the vertical resolution of 1 degree and the horizontal resolution of sub-degree [5]. On the other hand, the current commercial automotive mmWave radar typically provides the distance resolution of 5-70cm and the horizontal resolution of 7-15 degree, which is not accurate enough to perform the 3D imaging [6] [7]. Furthermore, mmWave signals experience mirror-like specular reflections causing only a few reflections back to the radar receiver. According to recent researches [8]–[10], 80% of the received power at 60-70GHz is carried by specular contribution rather than by scattering effects. This mirror-like characteristic can produce a blind spot of the radar image.

Indeed, mmWave radar is a great candidate to support LiDAR and camera in harsh driving conditions in AVs. However, we observe the following challenges that hamper the mmWave radar from producing high resolution imaging.

- The upper limit of the distance resolution of mmWave radar is no better than 3cm. In theory, the distance resolution depends on the bandwidth of the transmitted radar signal, i.e., a radar with wider bandwidth can give a higher distance resolution. However, a single automotive

radar today typically has less than 5GHz bandwidth. The limited bandwidth comes from hardware constraints (antenna or front-end Radio Frequency (RF) devices). In order to cover the wider bandwidth in a single radar platform, its antenna should also support the wide bandwidth which brings other technical challenges [11] [12]. A wideband tunable RF device with low latency is also another requirement.

- The image acquired by mmWave radar can be either incomplete or shabby due to strong specular effects of mmWave signals. Because of the specular reflection, few or none of the reflected signals off the object head back to the radar.

We briefly outline our core approaches and research questions next.

- Radar fusion: We propose to use the existing radar platforms without any hardware modification and utilize them to collaborate with each other. By fusing the multi-radars over different operating frequencies, the combined information can be helpful to achieve a better resolution. However, new challenges emerge when fusing the multi-radars. (1) Simply concatenating the sample sets will lose the coherency between them, and therefore does not lead to improving the resolution. Preserving mutual coherence is required prior to processing further. (2) With the mutual coherence, the information is still missing in the frequency gaps between the multi-radars. Precise modeling of the missing gaps is a critical problem. (3) Adapting compressive sensing algorithm to reconstruct the missing information is not fully feasible in this scenario because the operating frequencies are not spread over randomly. As they are rather located in a specific frequency range, the performance of the compressive reconstruction will be compromised.
- Spatial diversity: In order to resolve the specularity in mmWave signals, we exploit spatial diversity. We observed that the specularity can give the radar a stronger reflection than the scattering when the radar locates at the right angle. By the mobility of automotive radar due to vehicles' movement, a synthetic aperture can be created. However, implementing Synthetic Aperture Radar (SAR) on vehicles has the following challenges. (1) Unlike airborne flight path whose velocity and trajectory are close to constant and linear, the vehicles create an irregular velocity and driving trajectory. (2) While the size of synthetic aperture in airborne objects can be extremely large, a much shorter aperture in the vehicle scenario may not be enough to resolve the specularity by itself.

The rest of the paper is organized as follows. Section II presents the proposed high resolution Frequency Modulated Continuous Wave (FMCW) radar system. Section III discusses the conclusions and future works.
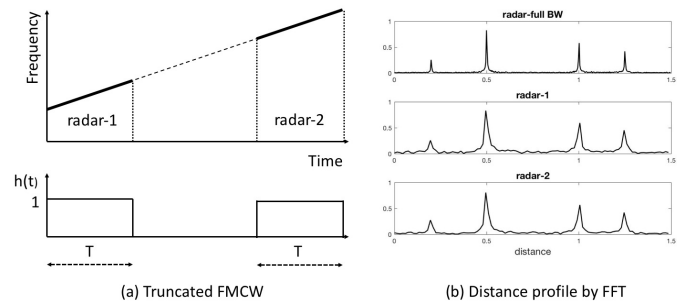

Fig. 1. An example of fusing two radar systems is shown. (a) Two radar systems operating different bands. (b) Comparison of the resulting distance profiles.

II. HIGH RESOLUTION FMCW

A. Radar Fusion

The distance resolution of FMCW radar, Δd, is bounded by its bandwidth,

$$\Delta d = \frac{C}{2B} \tag{1}$$

where C is the speed of light, and B is the bandwidth of the FMCW radar. Increasing the bandwidth of radar, however, is not a simple task. RF devices that support the wide bandwidth are an expensive solution, especially to sweep the wide range in a short period. It is also a challenging problem to design a wideband antenna [11], [12]. Hence, it is urged to consider a new approach for this problem. Instead of increasing the bandwidth of a single radar, we propose to exploit the existing mmWave radar platforms (i.e., 24GHz, 60GHz, and 79GHz radars) without any hardware modification and utilize them to collaborate. By fusing the multiple radars over different frequencies, the combined information can be helpful to achieve a better resolution.

Consider an FMCW system with a full bandwidth that can achieve the desired distance resolution. Fig. 1 (a) shows an example of two sub-radar systems operating in two different frequencies. Each sub-radar system has a worse distance resolution than the one with the full bandwidth shown in Fig. 1 (b). For the sake of simplicity, we assume every radar has the same FMCW slope, α, and the same period of measurement, T. Then, the sub-radars can be viewed as a truncated FMCW system. The received signal for the full-bandwidth FMCW is

$$x_{full}(t) = \sum_{m=1}^{M} e^{j2\pi(\alpha\tau_m t + f_0\tau_m)}, t = nT_s, n = 0, ..., N-1 \tag{2}$$

where M is the number of reflectors, τ_m is the TOF of the m-th reflector, f_0 is the starting frequency of the FMCW, T_s is the sampling period, and N is the number of samples. Note that the frequency and the phase of the received signal are related to τ_m. Then, we can define a support function $h(t)$ as

$$h(t) = rect_T(t - t_1) + rect_T(t - t_2) \tag{3}$$

where $rect_T(t)$ is a rectangular function centered at 0 whose period is T, and amplitude is 1. The measured beat signal from the sub-radars is expressed by multiplying $h(t)$ and x_{full}:

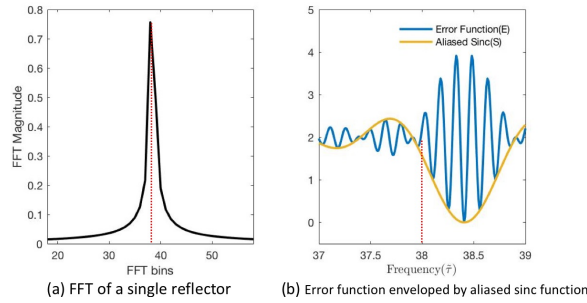$$x_{meas}(t) = h(t) \cdot x_{full}(t) + w(t). \tag{4}$$

Fig. 2. (a) FFT magnitude of the measured beat signal reflected by a single reflector. (b) Error function.

where $w(t)$ is additive white Gaussian noise. The best estimate of τ_m would minimize the following error function:

$$E(\widetilde{\boldsymbol{\tau}}) = \frac{1}{N} \sum_{n=0}^{N-1} \| x_{meas}(nT_s)$$
$$- h(nT_s) \cdot \sum_{m=1}^{M} e^{j2\pi(\alpha\widetilde{\tau_m}nT_s + f_0\widetilde{\tau_m})} \|^2,$$

where $\widetilde{\boldsymbol{\tau}}$ is a M-length vector of $\tau_1, ..., \tau_M$. However, the error function is not convex due to the complex exponentials. For further simplicity, consider a single τ and the frequency bands of the two radars are right next to each other, leading to a single rectangular function $h(t)$ with a full band period. The error function can be re-written as

$$E(\tilde{\tau}) = \frac{1}{N} \sum_{n=0}^{N-1} \| e^{j2\pi(\alpha\tau nT_s + f_0\tau)} - e^{j2\pi(\alpha\tilde{\tau}nT_s + f_0\tilde{\tau})} \|^2$$
$$= 2 - \frac{2}{N} \cos\left[2\pi\left(f_0 + \frac{\alpha(N-1)T_s}{2}\right)(\tau - \tilde{\tau})\right]$$
$$\cdot \frac{\sin\left[\pi\alpha NT_s(\tau - \tilde{\tau})\right]}{\sin\left[\pi\alpha T_s(\tau - \tilde{\tau})\right]}$$

If one can find $\tilde{\tau}$ that satisfies the minimum value of the error function, the distance resolution can be improved better than $\frac{C}{2B}$.

The error function can be considered as an amplitude modulated signal with a carrier signal of frequency $f_0 + (N-1)\alpha T_s/2$ enveloped by the aliased sinc function as shown in Fig. 2 (b). Note that the period of the carrier signal is dominated by the starting frequency f_0 (20-80GHz range) than the bandwidth term (below 5GHz), which results in multiple periods of the carrier signal in one FFT bin. Hence, gradient descent would not find the global optimum point due to many local minima in the search range. One can evaluate the error function by exhaustive search. The initial estimation of $\tilde{\tau}$ can be given by the location of the FFT peak (38th FFT bin) in Fig. 2 (a). However, finding the global minimum (38.4 in Fig. 2 (b)) requires a very fine step size due to high-frequency components from the carrier signal. The computation time will even worsen when there are multiple reflectors in a single FFT bin. Therefore, we propose to leverage the envelope instead of directly using the error function as a cost function. Because the envelope shares the minimum point with the original error function, one can find the same solution. The envelop signal

varies slower and has fewer local minima, which will cause fewer difficulties to find the minimum value.

The description above assumes a single reflector and a smooth truncated FMCW system. Various research questions show up when these assumptions are not valid anymore. (1) The number of reflectors is usually unknown. An additional process to estimate the number of reflectors before solving the problem is required. (2) Multiple numbers of reflectors can be located within a single FFT bin. It will increase the number of variables to solve. Even with the single reflector assumption, an extremely fine step size is required due to the high-frequency component in the error function. (3) The truncated FMCW systems will have a frequency gap between them. It will make the error function complicated and challenging to solve.

B. Spatial Diversity

mmWave signals experience mirror-like reflections on the surface of the objects [8]–[10]. Because of the specular reflection, few or none of the reflected signals off the object can head back to the radar unlike the scattering effect (or diffuse reflection). The specular reflection becomes even more substantial on a smooth metallic surface, such as vehicles. The weak back-reflection due to specularity will produce an either incomplete or shabby image.

In order to resolve the specularity in mmWave signals, we exploit the spatial diversity of the vehicles. We observed that the specularity can give the radar a stronger reflection than the scattering when the radar locates at the right angle. In addition to resolving specularity, the spatial diversity can also help the radar improving its image. During the motion of the radar on a vehicle, the data is collected over time. The different geometric positions of the radar created by the motion of the radar produce a large synthetic aperture. In theory, a larger antenna aperture can produce a higher resolution.

The conventional SAR algorithms, such as Range-Doppler, utilize the phase-modulation effect of the echo signals and transform the spatial domain into the spatial frequency domain to resolve the locations of the objects. The Range-Doppler approach, however, is challenging to adapt non-uniform spatial sampling. In this paper, we consider a linear inverse-based SAR algorithm in order to incorporate random radar motion. SAR imaging can be viewed as a linear inverse problem in which the unknowns are the reflectivity map of the objects. A received signal at position u is linearly related to the unknowns as:

$$r_u(t) = \iint s(x,y)e^{j2\pi\left[\alpha\tau(x,y;u)t + f_0\tau(x,y;u)\right]} dx\,dy \quad (5)$$

where $s(x,y)$ is the reflectivity map at x and y. Note that τ is a function of x and y at given u. We can discretize x and y and vectorize $s(x,y)$ and obtain the following system equation at u:

$$\mathbf{r_u} = \mathbf{A_u}\mathbf{s} + \mathbf{w}, \quad (6)$$

where $\mathbf{s}$ is the vectorized $s(x,y)$, w is additive white Gaussian noise, and $\mathbf{A_u}$ is the matrix whose columns are the complex-exponential kernels in (5). By stacking the entire received
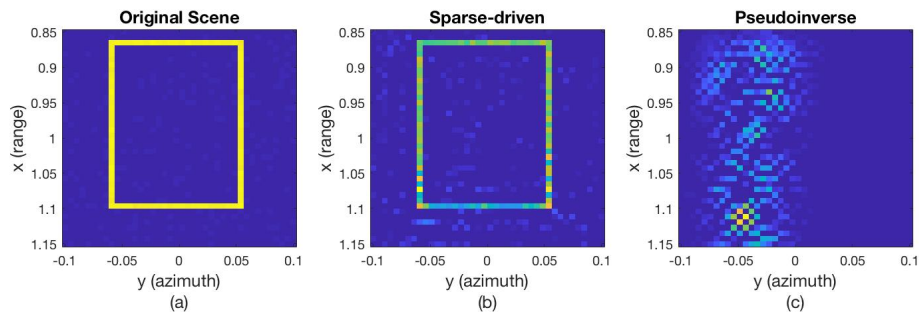
Fig. 3. SAR performance comparison by simulation : (a) original scene, (b) proposed sparse-driven SAR, and (c) conventional SAR by pseudo-inverse.

signal at all u, the entire system becomes $\mathbf{r} = \mathbf{As} + \mathbf{w}$. Given the limited number of measurements, the inverse problem can be ill-posed. We exploit the observation that the reflectivity map is sparse consisting of a small number of objects. Hence, the estimation of s can be obtained by

$$\min_{\mathbf{s}} \quad \frac{1}{2}\|\mathbf{r} - \mathbf{As}\|^2 + \lambda\|\mathbf{s}\|_1 \qquad (7)$$

The choice of λ determines the relative contribution of the sparsity. Fig. 3 illustrates the simulation results of SAR images. By randomly taking 30% of the entire spatial samples, the reconstructed images by the sparse-driven SAR and by the pseudo-inverse are shown in Fig. 3(b) and (c), respectively.

While the sparse-driven SAR can reconstruct accurate SAR images with random radar positions, several research questions remain as the followings: (1) The target objects are assumed to be ideal scatters. Can we model the specularity and reconstruct the image? (2) The position of the radar has no error in the above simulation. When there exists noise in the measurement of the radar position, how can we adapt the errors? (3) In the practical scene, the targets are expected to be piecewise smooth, which is not modeled in the above model. Can we incorporate such smoothness in our model?

III. CONCLUSION AND FUTURE WORK

The proposed research demonstrates how the performance of mmWave radar can be extended and provide autonomous vehicles with more reliable sensing capability. This research provides a new method for increasing the mmWave radar resolution by understanding the principles of electromagnetic (EM) radiation and the mathematical model of radar under dynamic vehicle motion.

- The proposed research will develop a model to combine multiple radar platforms and fuse the information in order to achieve better distance resolution. We will gain a better understanding of radar fusion and establish a framework to investigate the behavior of mmWave signals at different frequencies.
- The proposed research will investigate how the specularity of mmWave signal degrades the radar image. By understanding its specular behavior in vehicle situations, we will develop a new model for automotive radar imaging that resolves the specularity.

- The proposed research will incorporate the dynamics of vehicles in radar sensing/imaging. We will integrate the principles of EM radiation and the mathematical model of the radar in dynamic vehicle motion. This will provide a new algorithm for higher resolution radar images.

REFERENCES

[1] A. J. Hawkins, "Waymo is first to put fully self-driving cars on US roads without a safety driver," https://www.theverge.com/2017/11/7/16615290/waymo-self-driving-safety-driver-chandler-autonomous, accessed: 2021-05-19.

[2] SAE On-Road Automated Vehicle Standards Committee and others, "Taxonomy and definitions for terms related to driving automation systems for on-road motor vehicles," *SAE International*, 2021, accessed: 2021-05-19.

[3] B. Yamauchi, "Fusing ultra-wideband radar and lidar for small ugv navigation in all-weather conditions," in *Int. Soc. Opt. Eng.(SPIE)*, vol. 7692, 2010, pp. 1–10.

[4] M. Barnard, "Tesla and Google Disagree About LIDAR? Which Is Right?" https://cleantechnica.com/2016/07/29/tesla-google-disagree-lidar-right/, 2016, accessed: 2021-05-19.

[5] Velodyne, http://velodynelidar.com/products.html, 2018, accessed: 2021-05-19.

[6] Bosch, "Radar-based driver assistance systems," https://www.bosch-mobility-solutions.com/media/global/products-and-services/passenger-cars-and-light-commercial-vehicles/driver-assistance-systems/predictive-emergency-braking-system/mid-range-radar-sensor-(mrr)/product-data-sheet-mid-range-radar-sensor-(mrr).pdf, 2018, accessed: 2021-05-19.

[7] J. Hasch *et al.*, "Millimeter-wave technology for automotive radar sensors in the 77 ghz frequency band," *IEEE Transactions on Microwave Theory and Techniques*, vol. 60, no. 3, pp. 845–860, 2012.

[8] W. Fan, I. Carton, J. Ø. Nielsen, K. Olesen, and G. F. Pedersen, "Measured wideband characteristics of indoor channels at centimetric and millimetric bands," *EURASIP Journal on Wireless Communications and Networking*, vol. 2016, no. 1, p. 58, 2016.

[9] K. Haneda, J. Järveläinen, A. Karttunen, M. Kyrö, and J. Putkonen, "A statistical spatio-temporal radio channel model for large indoor environments at 60 and 70 ghz," *IEEE Transactions on Antennas and Propagation*, vol. 63, no. 6, pp. 2694–2704, 2015.

[10] F. Fuschini *et al.*, "Analysis of in-room mm-wave propagation: Directional channel measurements and ray tracing simulations," *Journal of Infrared, Millimeter, and Terahertz Waves*, vol. 38, no. 6, pp. 727–744, 2017.

[11] P. S. Hall, P. Gardner, and A. Faraone, "Antenna requirements for software defined and cognitive radios," *Proceedings of the IEEE*, vol. 100, no. 7, pp. 2262–2270, 2012.

[12] P. S. Hall *et al.*, "Reconfigurable antenna challenges for future radio systems," in *Antennas and Propagation, 2009. EuCAP 2009. 3rd European Conference on*. IEEE, 2009, pp. 949–955.

CurTail: Distributed Cotask Scheduling with Guaranteed Tail-Latency SLO

Zhijun Wang
The University of Texas at Arlington
Arlington, USA
email: zhijun.wang@uta.edu

Hao Che
The University of Texas at Arlington
Arlington, USA
email: hche@uta.edu

Hong Jiang
The University of Texas at Arlington
Arlington, USA
email: hong.jiang@uta.edu

Abstract—**Today's user-facing interactive datacenter services, such as web searching and social networking, have to meet stringent tail latency Service Level Objectives (SLOs). Unfortunately, due to the scale-out nature of the workloads, how to enable both tail-latency-SLO guarantee for such services and high resource utilization remains a critical challenge. In this paper, we propose a distributed Cotask scheduler with guaranteed Tail-latency SLO (CurTail), aiming at providing both job tail-latency-SLO guarantee and high resource utilization. CurTail is a top-down, holistic approach. It decouples an upper job-level design from a lower task-level design. At the job level, a decomposition technique is proposed to translate a given job tail-latency SLO into task-level performance budgets for tasks in a cotask, i.e., the collection of tasks spawned by a job. At the task level, the task budgets are translated into both task compute and networking resource demands, hence allowing for distributed cotask scheduling. The preliminary testing results based on simulation indicate that CurTail can indeed provide job tail-latency SLO guarantee at high resource utilization.**

Index Terms—**Tail latency SLO guarantee, cotask scheduling, datacenter.**

I. Introduction

To date, datacenter service providers generally overprovision datacenter resources to provide high assurance of meeting Service Level Objectives (SLOs) for datacenter services, e.g., stringent tail-latency SLOs for user-facing interactive services. For instance, aggregate CPU and memory utilizations in a 12,000-server Google cluster are mostly less than 20% and 40%, respectively [1]. As datacenters are approaching their capacity limits, in terms of, e.g., computing capacity and power budget [2], *how to improve datacenter resource utilization while providing SLO guaranteed services* becomes an important design objective for job scheduling, called *the objective* for short hereafter. To this end, however, one must successfully tackle two key challenges.

The first challenge is how to translate job-level SLOs into precise runtime system resource demands at the task level. Today's user-facing interactive services are predominantly scale-out by design. Namely, a job may spawn a large number of tasks (the exact number is called the job fanout degree), collectively known as a cotask [3], to be dispatched to, queued at, processed by workers and the resulting data flows, collectively known as a coflow [4]–[10], returned from a large number of servers. The job response time is determined by the time the resulting data of the slowest task is returned

and hence, is a strong function of job fanout degree. Clearly, a job scheduler must know the exact cotask/coflow resource demands, so that the right amounts of compute and networking resources can be allocated to achieve the objective.

The second challenge is that the objective calls for joint compute and networking resource allocation. With interleaved task dispatching, task computing, and resulting data returning per job execution, it becomes clear that compute and networking resources must be jointly allocated to be effective.

The existing solutions are simply not up to the above challenges. First, largely due to the lack of a means to do the translation, the existing cotask-aware (e.g., [3], [9], [11], [12]) and coflow-aware job scheduling solutions (e.g., [4]–[6]) are centralized by design and hence not scalable, and exclusively focused on average performance targets, e.g., minimizing average job/coflow completion time, rather than meeting job-tail-latency SLOs.

Second, most existing job scheduling and resource provisioning solutions are point by design, concerned with either compute (e.g. [13]–[17]) or networking (e.g., [6], [7], [18], [19]) aspects of resource provisioning, rather than both jointly. This makes it difficult for the existing solutions to achieve the objective.

Third, the existing tail-latency-aware job scheduling solutions (e.g., [20]–[24]) are exclusively focused on storage applications and jobs with fanout degree of one only. Some solutions focusing on outlier alleviation have been developed to shorten the job tail latency. For example, several solutions of task-size-aware task reordering in a task queue have been proposed [25]–[27] to avoid head-of-line blocking of small-sized tasks by large-sized ones to reduce the overall task tail latency. CPU power control schemes [28], [29] have been designed to Dynamically adjust Voltage and Frequency Scaling (DVFS) for task servers based on task execution time to save energy and maintain low task tail latency. However, the approaches taken by such solutions cannot be applied to jobs with job fanout degrees larger than one, as the resource demands for tasks belonging to jobs with different fanout degrees are different.

To achieve the objective of high resource utilization while providing tail latency guarantee, this paper proposes a distributed **C**otask scheduler with g**uar**anteed **Tail**-latency SLO (CurTail). CurTail is a top-down, holistic approach. It decou-

ples the upper job-level design from the lower task-level or runtime-system design. At the job level, by leveraging a prior work [30], [31], we propose a decomposition technique that translates a given job tail-latency SLO into a task performance budget shared by all the tasks in the cotask of a job. This effectively decomposes a complex job-level cotask/coflow resource allocation problem into individual task/flow resource allocation subproblems at the task level. The design at this level is independent of the underlying runtime systems to be used and, hence, is portable to any datacenter platforms.

At the task or runtime system level, the task performance budgets are first translated into task compute and networking resource demands. Then, the proposed distributed task and flow schedulers allocate the resources to match the resource demands, hence, achieving the objective. The major contributions of the paper are:

- CurTail is a top-down approach, it decouples an upper job-level design from a lower task-level design and is independent on underlying systems, and hence it can be easily implemented;
- Curtail jointly allocates compute and networking resources based on the task resource demand to meet tail latency SLO, and hence can greatly improve system resource utilization.

The preliminary testing results based on datacenter simulation demonstrates that CurTail can indeed provide tail-latency-SLO guarantee and high resource utilization.

The rest of paper is structured as follows. Section II gives the detailed descriptions of CurTail and Section III presents the performance evaluation of CurTail, finally Section IV concludes the paper.

II. CurTail

CurTail schedules cotasks in two distinct logical steps. First, at the job level, the job tail-latency SLO for a given service is translated into task response time budgets for all the tasks a job spawns. Second, at the task level, the right amount of compute and networking resources are allocated to individual tasks that meet the task budgets, hence, achieving the objective. In what follows, we first give an overview of CurTail and then discuss the two steps, separately.

A. CurTail Overview

With reference to Figure 1, CurTail works as follows. When a job scheduler in a master receives a job with a given tail-latency SLO and a given fanout degree, K, it translates the tail-latency SLO into a task response time budget shared by all the tasks the job spawns. As long as the task response time, i.e., the sum of the task dispatch time, task queuing time, task compute time, and flow completion time for every flow in the task coflow is within the task budget for the tasks belonging to the job, the tail-latency SLO for that job is guaranteed to be met. This effectively decouples a complex job-level resource allocation problem into distributed task-level subproblems at individual workers the tasks are mapped to. The design at this
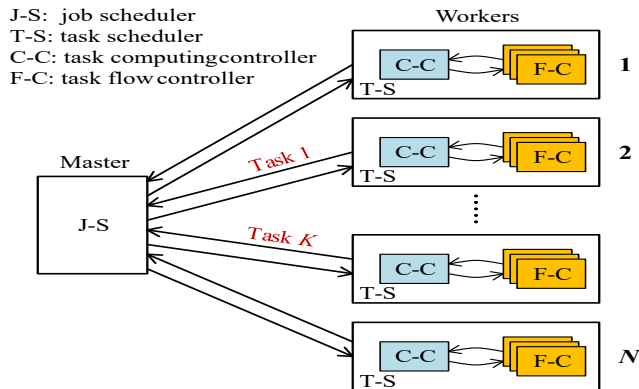

Fig. 1. A job scheduler, J-S, runs in a master node and distributed task schedulers, T-S, run in individual workers in the cluster, each of which is mainly composed of a compute controller, C-C, and a flow scheduler, F-C, per flow emitted from the worker.

TABLE I
THE 99-TH PERCENTILE TAIL-LATENCY VS. JOB FANOUT DEGREE

Fanout degree	1	10	100	1000
Tail-latency (ms)	23.03	34.51	46.03	57.54

level is runtime system independent and hence, can be pre-computed offline for jobs of different fanout degrees and is portable to any datacenter platforms.

Then, the tasks, together with the task budgets, are dispatched to K workers in a cluster to be processed. CurTail does not dictate what task dispatching algorithm should be used, and hence, can work with any task dispatching algorithms. It focuses on the task compute and task flow resource allocation at individual workers. Upon the arrival of a task at a worker, based on the budget, the task scheduler, T-S, in the worker, then sets parameters in a task compute controller, C-C, and a flow controller, F-C. Collectively, these controllers ensure that datacenter compute and networking resources are allocated with high precision to meet task budgets, and hence, SLOs for individual jobs at high resource utilization.

B. Job-Tail-Latency-to-Task-Budget Translation

We leverage an existing solution for a general black-box Fork-Join model (i.e., with all the fork nodes treated as black boxes) [30], [31]. This solution states that the pth-percentile job tail-latency x_p can be approximately expressed in terms of the mean (E) and variance (V) of task response time, and job fanout degree (K), i.e., $x_p \approx x_p(K, E, V)$ (see [30], [31] for details). This approximation is found to be sufficiently accurate at high load (e.g., 80% or above) for a wide range of Fork-Join structures of practical interests. In particular, with tail cutting [32], [33], or equivalently, light-tailed task execution time distribution, the solution is found to be accurate even at low load. Since tail-cutting techniques have been widely deployed to combat stragglers in practice [32], we assume that the approximation is accurate at any load level in practice.

In what follows, we make three important observations with regard to this approximation.

First, we observe that $x_p \approx x_p(K, E, V)$ is an increasing function of K. As K increases, the slowest task in the cotask of a job is likely to become slower, resulting in a longer job tail-latency. For example, assume that $E = 5$ ms and $V = 25$ ms^2, the 99th-percentile (i.e., $p = 99$) tail-latency for jobs with different fanout degrees are listed in Table I. As one can see, it increases from about 23 ms to 35 ms and then to 59 ms as job fanout degree increases from 1 to 10 and then to 1000. These results also indicate that the job tail-latency is a strong function of job fanout degree.

Second, we note that $x_p \approx x_p(K, E, V)$ must also be an increasing function of both E and V, simply because the slowest task gets slower as E and/or V increases and hence, the job tail-latency also increases. As a result, E and V can be viewed as *task performance budgets* in order to meet x_p. Specifically, to ensure that the job tail-latency is no larger than x_p, the means and variances of the task response time for all the tasks in cotasks must not exceed E and V, respectively. Moreover, we observe that to keep x_p unchanged as job fanout degree K increases, either E or V or both must be reduced. The implication of this observation is significant. It means that to meet the job tail-latency SLO for a given service in terms of x_p, the task budgets, and hence, per-task resource demand, for jobs with different fanout degrees are different.

Third, we note that the translation of a given job tail-latency x_p to the task budgets is one-to-many, admitting virtually unlimited number of $\{E, V\}$ budget pairs. This is because the change of x_p due to the increase (decrease) of E can be offset by properly decreasing (increasing) V and vice versa. In other words, a smaller budget in terms of V allows a bigger budget in terms of E, and vice versa. One may narrow down to one pair of task budgets by letting $\sqrt{V} = \alpha E$, where α is a tunable parameter, which as we shall discuss in more detail, may be estimated based on measurement. Now by taking the inverse of $x_p \approx x_p(K, E, V) \equiv x_p(K, E, \alpha)$, we have, $E \approx E(K, \alpha, p, x_p)$, the task budget in terms of the task mean response time. It means that for a service with tail-latency SLO in terms of x_p and α that guarantees that V will be met, as long as a job scheduler can ensure that the mean task response time for all the tasks is within $E(K, \alpha, p, x_p)$, the job tail-latency SLO is guaranteed.

As an example, for a service with the job tail-latency SLO in terms of $x_{99} = 100$ ms, Figure 2 (a) gives the mean task response time budgets at various α values for jobs with fanout degrees 1, 10 and 100, respectively. We can see that the mean task budget is sensitive to α. When α increases from 0.4 to 2.0, the mean task budget decreases from about 44, 33, and 27 ms to 10, 6, and 4 ms for jobs with fanout degree 1, 10 and 100, respectively.

Figure 2 (b) gives the mean task response time budget versus fanout degree at $\alpha = 0.5$, 1 and 2, respectively. The budget is sensitive to job fanout degree when it is small (from 1 to 10), and then become less sensitive as it further increases. The budget decreases from about 38, 22, and 10 ms to 28, 15, and
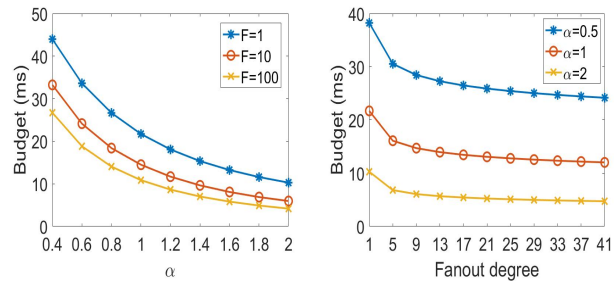

Fig. 2. Mean task response time budget: (a) varying with α; and (b) varying with job fanout degree.

6 ms as the fanout degree increases from 1 to 9 at $\alpha = 0.5$, 1 and 2, respectively. It confirms that the jobs with different fanout degrees may have quite different task budgets. In other words, the task resource demands for tasks from jobs with different fanout degrees can be significantly different.

C. Task Resource Allocation

This step is runtime system dependent, and hence, must be carried out at individual workers at runtime. We assume that the task dispatch overhead is small and can be treated as a small fixed task delay ΔE, which is assumed to have been deducted from E already. Namely, E now represents the mean task response time budget for task queuing, compute and task result return. Consider a service with the tail-latency SLO defined by x_p and task budget $E(K, \alpha, p, x_p)$ for jobs of fanout degree K. Further, consider task k in the jth job mapped to worker q, and denote $r_{j,k}^c$ and $r_{j,k}^f$ as the task compute rate and task flow rate at worker q, respectively. Then, we let,

$$r_{j,k}^c \geq \Lambda_{K,q}^c, \quad r_{j,k}^f \geq \Lambda_{K,q}^f, \quad j \in S(K), \quad (1)$$

where $S(K)$ is the set of all jobs with fanout degree K, and $\Lambda_{K,q}^c$ and $\Lambda_{K,q}^f$ are the minimum compute rate and flow rate constraints for any task in job j mapped to worker q, which in turn, satisfy the following inequalities,

$$\frac{W^c}{\Lambda_{K,q}^c} + \frac{W^f}{\Lambda_{K,q}^f} \leq E(K, \alpha, p, x_p), \quad (2)$$

where W^c and W^f are the predicted mean task compute workload size and mean flow size for all tasks in that service.

Clearly, as long as both the compute rate, $r_{j,k}^c$, and flow rate, $r_{j,k}^f$, satisfy the above inequalities for all K tasks in the cotask of a job, the job is guaranteed to meet its tail-latency SLO. Note that this guarantee is on a per job basis and hence, works even when different jobs have different tail-latency SLOs, i.e., different jobs are assigned different x_p and p pairs.

Now, the questions remain to be answered are how to estimate α, or equivalently, V, and how to determine and allocate the minimum compute rate, $\Lambda_{K,q}^c$, and the minimum flow rate, $\Lambda_{K,q}^f$. Assume that the task compute response time and the associated flow completion time are independent random variables. Then $V = V_c + V_f$ [34], where V_c and V_f are the budgets for the variances of the task compute time

and flow completion time, respectively. In what follows, we deal with flow related parameters, $\Lambda_{K,q}^f$ and V_f, separately from compute related parameters, $\Lambda_{K,q}^c$ and V_c. In CurTail, the network condition can be measured through packet round trip time and the unloaded job tail latency can be computed based on the task response time by excluding the queuing time, and hence its overheads are light.

Estimating $\Lambda_{K,q}^f$ **and** V_f: Since the datacenter network resources are shared by all the flows, one has limited control over these two parameters. So in CurTail, these parameters are, to a large extent, obtained based on measurement. CurTail applies Minimum Rate Guarantee (MRG) [35], a soft minimum flow rate guaranteed congestion control protocol, to maintain an average flow completion time with high probability, which serves as the flow controller, F-C, in Figure 1. Based on the measurement of the network condition, a proper minimum rate $\Lambda_{K,q}^c$ that can be sustained with high probability is set in MRG. Likewise, V_f will simply be set at the measured variance of the flow completion time.

Estimating $\Lambda_{K,q}^c$ **and** V_c: Again, V_c is simply set at the measured variance of the task compute time. Together with the estimated V_f above, V is set at $V_c + V_f$, with possibly a small extra margin to guard against the measurement errors. With given V, K, and x_p, α or $E = E(K, p, x_p, \alpha)$ is then uniquely determined. From Eq. (2), we have,

$$\frac{W^c}{\Lambda_{K,q}^c} \le E(K, \alpha, p, x_p) - \frac{W^f}{\Lambda_{K,q}^f} \equiv E_c(K, \alpha, p, x_p), \qquad (3)$$

where $E_c(K, \alpha, p, x_p)$ is the task compute budget. While $\Lambda_{K,q}^f$ and W^f are well defined and measurable, $\Lambda_{K,q}^c$ and W^c are not easy to quantify and measure. Hence, in the CurTail design, instead of attempting to directly estimate the minimum compute rate, $\Lambda_{K,q}^c$, we focus directly on how to allocate the task compute resource to meet the compute budget, $E_c(K, \alpha, p, x_p)$.

Let T_q^c be the unloaded mean task compute response time for a service at worker q. By "unloaded", we mean that the entire compute resource in a worker is allocated to the task without resource contention at worker q. We assume that T_q^c can be acquired by measurement. Clearly, we must have, $T_q^c \le E_c(K, \alpha, p, x_p)$, otherwise, the compute budget cannot be met, even with the entire worker compute resource allocated to the task. In each worker, tasks are scheduled using a time-sharing scheduler, i.e., the compute controller, C-C, in Figure 1. To meet the compute response time budget, the scheduler at a worker allocates at least $p_{K,q}^c = T_q^c / E_c(K, \alpha, p, x_p)$ percent of the total compute resource to the task from that service. If all the workers have equal compute resource, then $T_q^c = T^c$ and $p_{K,q}^c = p_K^c$, $\forall q$.

III. SIMULATION TESTING

Simulation setup: Consider two datacenter services, one with a tail-latency SLO, whose jobs are called T-jobs, and the other without SLO requirement, whose jobs are called B-jobs. We treat B-jobs as a single best-effort job and all the B-tasks, i.e., the tasks from B-jobs, share a First-in-Fisrt-Out (FIFO) queue at each worker, handled by a single thread. Each T-task, i.e., a task from a T-job, arriving at a worker, is handled by a new thread in the worker. CurTail allocates all the additional compute resources to the B-tasks, provided that p_K^c percent of the total compute resource is allocated to a T-task. In the absence of a B-task at a worker, the additional worker resources are then equally shared by T-tasks. Obviously, so long as the sum of p_K^c's for all the T-tasks mapped to the worker is less than one, the task compute budgets for all the T-tasks can be met. The additional compute resource, if available, will then be dedicated to the first B-task from the B-task FIFO queue.

The task processing time is time sliced with the slice size set at 1 ms. Each T-task is serviced for multiple time slices on average before context switching. If the execution time of a task is less than 1 ms, it can be switched out before the end of the time slice. This ensures that a context switching will consume no more than a few percent of the CPU resource, as each context switching takes about 50 μs to finish [36], [37].

As aforementioned, CurTail does not specify how tasks should be dispatched. To avoid the possible bias as a result of the use of a specific task dispatching algorithm, we consider two extreme task dispatching algorithms, one with the global information and the other with no information at all. For the former one, when a job arrives at a job scheduler, the tasks of the job are distributed to different workers which have the least numbers of tasks. For the latter one, upon a job arrival at a job scheduler, the tasks for the job are randomly distributed to workers. We test the performance of CurTail against a baseline case where each worker runs two strict priority FIFO queues. The high/low priority queue stores T-tasks/B-Tasks. The tasks from low priority queue cannot be served unless the high priority queue is empty.

Consider a datacenter with a 5x5 leaf-spine network topology and with each rack having 80 hosts (4 job schedulers and 76 workers). The bandwidth/propagation delay is set at 10Gbps/10μs between a host and a leaf node and 10Gbps/20μs between a leaf node and a spine node. While individual jobs in B-job are large jobs in terms of task execution time, representing background batch applications, T-jobs are small jobs, representing user-facing interactive applications. About equal numbers of the two types of jobs are generated, which arrive following a Poisson process. The task execution time for each task follows an exponential distribution with averages of 40 ms and 5 ms for the B-jobs and T-jobs, respectively.

Some background flows running among randomly selected worker pairs are also generated. The flow arrival process is a Poisson process and the flow arrival rate is adjusted so that the total network traffic load is the same as the compute load. This ensures that both compute and network resources will be simultaneously stressed as the load increases.

We further assume that each T-task or B-task execution generates a single task flow with flow size randomly selected from 1K to 500 Kbytes, resulting in an average size, $W^f = 250$

TABLE II
THE COMPUTE BUDGETS, E_c, AND THE PERCENTAGES OF COMPUTE
RESOURCE, p_K^c, IN A WORKER HAVE TO BE ALLOCATED FOR A T-TASK
FROM A JOB WITH FANOUT DEGREE K.

Fanout degree (K)	5	10	15	20	25
E_c(ms) (load$\leq$80%)	13.1	11.5	10.7	10.2	9.8
E_c(ms) (load 90%)	12.1	10.5	9.7	9.2	8.8
p_K^c(%) (load $\leq$ 80%)	38.2	43.5	46.7	49.0	51.0
p_K^c(%) (load 90%)	41.3	47.6	51.5	54.3	56.8

Fig. 3. Task dispatching with global information

Fig. 4. Random task dispatching

Kbytes for T-tasks. The flow rate $\Lambda_{K,q}^f$ that can be guaranteed is found to be 1 and 0.75 Gbps, $\forall q$, at the network loads of 80% or less and 90%, respectively. Then, the corresponding mean flow budget for T-tasks is set as 3 ms and 4 ms (including about ΔE=1 ms for task dispatch time) for load 80% or less and load 90%, respectively.

In this study, the fanout degrees for B-jobs and T-jobs are randomly selected from 1 to 50 and from the set of values (5, 10, 15, 20, 25), respectively. All the T-jobs share the same tail-latency SLO, with the 99th-percentile tail-latency set at 100 ms. By considering both the measured variances of the task flow and task compute times, $\alpha = 1$ is found to allow the variance budget guarantee. Then, we have the following task response time budgets (derived from [30]): 16.1, 14.5, 13.7, 13.2 and 12.8 ms for T-jobs with fanout degrees 5, 10, 15, 20 and 25, respectively. Finally, the compute budgets and the percentages of compute resource that have to be allocated in a worker (as the unloaded mean task compute time is 5 ms) are computed and listed in Table II.

Simulation results and analysis: First, we consider the case with global information. The 99th percentile tail-latency for T-jobs and the average job response times for both job types are used as the performance metrics. Figure 3 depicts the testing results. We see that for the baseline solution, the 99th-percentile tail-latency increases from about 150 ms to more than 250 ms when both compute and network loads increase from 50% to 90%, simultaneously. Note that all the tail latencies presented are measured for all T-jobs as a whole. Due to the lack of space, the tail-latencies for jobs of individual fanout degrees which are also found to meet the tail-latency SLO, are not given. The results indicate that a scheduler even with global information and using strict priority queuing cannot provide job tail-latency guarantee at medium and high loads (50% or higher), as in-service B-tasks can still block T-tasks from getting the worker resources. This explains why to date, the datacenters have to run at 20% to 50% resource utilization, in order to meet stringent tail-latency SLOs. On the other hand, for CurTail, the tail-latency increases from about 45 ms to about 80 ms only, below the tail-latency SLO of 100 ms. The
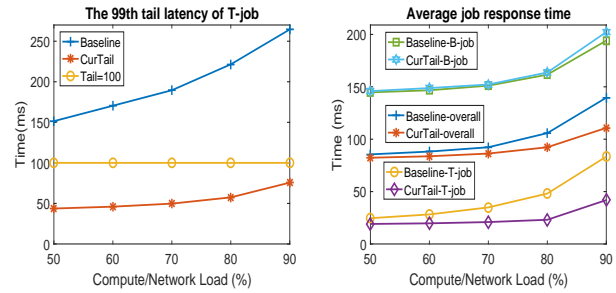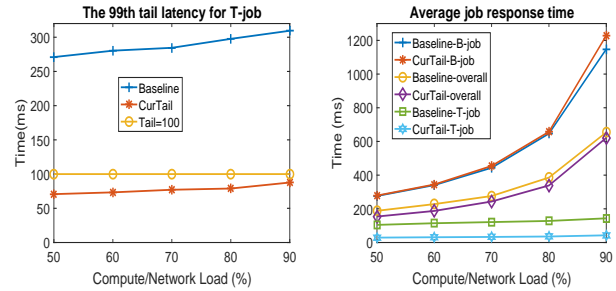
reason why CurTail can perform better than that required by the tail-latency SLO even at high load is that with global information for task dispatching, T-tasks still have good chances to find low load workers to map to, even though the overall load is high. As a result, they are still able to garner some additional compute and network resources to further push the tail-latency lower than the required SLO.

For CurTail, with the needed resources allocated to T-jobs with high precision, the average T-job response time increases from about 20 ms to 40 ms when the load changes from 50% to 90%. As a result, the overall average job response time for T-jobs also improves by about 50% at high load compared to the baseline solution. Meanwhile, CurTail offers almost the same performance for B-job as the baseline solution even at high load. CurTail achieves up to 20% better performance for overall job response time at high load.

Now, consider the case with random task dispatching. In this case, the task placement is much less balanced than the previous case, resulting in much longer tail-latency and average job response time. Figure 4 gives the testing results. As we can see, despite the less balanced load, CurTail still meets the tail-latency SLO, reaching about 90 ms at 90% load, close to the tail-latency SLO, whereas the tail-latency for the baseline solution reaches more than 300 ms. Due to the randomness of task placement, T-tasks have much less chance to find workers with low load, making it less likely to be able to garner much additional resource at high load. This clearly demonstrates the importance of using a solution like CurTail to meet the stringent tail-latency SLO, especially at high resource utilization. Similarly, CurTail performs about 70% better and has slightly better performance for average

T-job response time and overall job response time over the baseline solution, respectively, at the cost of less than 10% increase of the average B-job response time.

The above results strongly suggest that CurTail indeed provides tail-latency guarantee and high resource utilization for single Fork-Join job structure. An open issue is how to extend CurTail to deal with jobs with multi-stage Fork-Join structures or even a general Directed Acyclic Graph (DAG) workflow.

IV. CONCLUSIONS

In this paper, we propose CurTail, a distributed **C**otask scheduler with g**uar**anteed **Tail**-latency SLO (CurTail) aiming at providing job tail-latency-SLO guarantee and high resource utilization. CurTail is a top-down and holistic approach. It decouples an upper job-level design from a lower task-level design. At the job level, a decomposition technique is proposed to translate a tail-latency SLO to a task performance budget at the task level, which is runtime system independent and hence, portable to any datacenter platforms. In turn, the task performance budget is further translated into task resource demands at individual workers the tasks are mapped to. A distributed budget-aware cotask scheduling is developed. The preliminary testing results based on datacenter simulation indicate that CurTail can indeed provide job tail-latency SLO guarantee at high resource utilization.

ACKNOWLEDGMENT

REFERENCES

[1] C. Reiss, A. Tumanov, G. Ganger, R. Katz and M. Kozuch, "Heterogeneity and dynamicity of clouds at scale," Proceedings of the ACM SoCC, 2012.

[2] L. Barroso, J. Clidaras and U. Hölzle, "The Datacenter as a Computer: An Introduction to the Design of Warehouse-Scale Machines," Synthesis Lectures on Computer Architecture, vol. 8, no3, pp.1–154, 2013.

[3] Y. Zhao, S. Luo, Y. Wang and S. Wang, "Cotask scheduling in cloud computing," Proceedings of IEEE ICNP, 2017.

[4] S. Agarwal, S. Rajakrishnan, A. Narayan, R. Agarwal, D. Shmoys, and A. Vahdat, "Sincronia: Near-Optimal Network Design for Coflows," Proceedings of ACM SIGCOMM, 2018.

[5] S. Ahmadi, S. Khuller, M. Purohit and S. Yang, "On scheduling coflows,", Proceedings of MOS IPCO, 2017.

[6] M. Chowdhury and I. Stoica, Ion, "Efficient coflow scheduling without prior knowledge," Proceedings of ACM SIGCOMM, 2015.

[7] M. Chowdhury, Y. Zhong and I. Stoica, "Efficient coflow scheduling with varys," Proceedings of ACM SIGCOMM, 2014.

[8] Z. Qiu, C. Stein and Y. Zhong, "Minimizing the total weighted completion time of coflows in datacenter networks," Proceedings of ACM SPAA, 2015.

[9] F. R. Dogar, T. Karagiannis, H. Ballani and A. Rowstron, "Decentralized task-aware scheduling for data center networks," Proceedings of ACM SIGCOMM, 2014.

[10] M. Choedhury, and I. Stoica, "Coflow: A networking abstraction for cluster applications," Proceedings of ACM HotNets, 2012.

[11] B. Tian, C. Tian, H. Dai and B. Wang, "Scheduling coflow of multi-stage jobs to minimize the total weighted job completion time," Proceedings of IEEE INFOCOM, 2018.

[12] A. Munir, T. He, R. Raghavendra, F. Le and A. Liu, "Network Scheduling Aware Task Placement in Datacenters," Proceedings of ACM CoNEXT, 2016.

[13] Y. Xu, Z. Musgrave, B. Noble and M. Bailey, "Bobtail: Avoiding Long Tails in the Cloud," Proceedings of the USENIX NSDI, 2013.

[14] A. Ferguson, P. Bodik, E. Boutin and R. Fonseca, "Jockey : Guaranteed Job Latency in Data Parallel Clusters," Proceedings of the 7th ACM EuroSys, 2012.

[15] V. Vavilapalli et al., "Apache Hadoop YARN: Yet Another Resource Negotiator," Proceedings of the ACM Annual Symposium on Cloud Computing (SoCC), 2013.

[16] B. Hindman et al., "Mesos: A Platform for Fine-grained Resource Sharing in the Data Center," Proceedings of the USENIX NSDI, 2011.

[17] Z. Wang et al., "Pigeon: an Effective Distributed, Hierarchical Datacenter Job Scheduler," Proceedings of the ACM SoCC, 2019.

[18] M. Chowdhury, M. Zaharia, J. Ma, M. Jordan and I. Stoica, "Managing Data Transfers in Computer Clusters with Orchestra," Proceedings of the ACM SIGCOMM, 2011.

[19] C. Wilson, H. Ballani, T. Karagiannis and A. Rowstron, "Better Never than Late: Meeting Deadlines in Datacenter Networks," Proceedings of ACM SIGCOMM, 2011.

[20] A. Wang, S. Venkataraman, S. Alspaugh, R. Katz and I. Stoica, "Cake: Enabling High-level SLOs on Shared Storage Systems," Proceedings of the ACM SoCC, 2012.

[21] N. Li, H. Jiang, D. Feng and S. Zhang, "PSLO: enforcing the Xth percentile latency and throughput SLOs for consolidated VM storage," Proceeding of EuroSys, 2016.

[22] T. Zhu, A. Tumanov, M. Kozuch, M. Harchol-Balter and R. Ganger, "PriorityMeister: Tail Latency QoS for Shared Networked Storage,", Proceedings of the ACM SoCC, 2014.

[23] T. Zhu, D. Berger and M. Harchol-Balter, "SNC-Meister: Admitting More Tenants with Tail Latency SLOs," Proceedings of the ACM SoCC, 2016.

[24] T. Zhu, M. Timothy and M. Harchol-Balter, "WorloadCompactor: Reducing datacenter cost while providing tail latency SLO guarantees," Proceedings of the ACM SoCC, 2017.

[25] J. Li, N. Sharma, D. Ports and S. Gribble, "Tales of the Tail: Hardware, OS, and Application-level Sources of Tail Latency," Proceedings of ACM Symposium on Cloud COmputing (SoCC), 2014.

[26] P. Misra, M. Borge, I. Goiri, A.Lebeck, W. Zwaenepoel and R. Bianchini, "Managing Tail Latency in Datacenter-Scale File Systems Under Production Constraints," Proceedings of Eurosys, 2019.

[27] G. Prekas, M. Kogias and E. Bugnion, "ZygOS: Achieving Low Tail Latency for Microsecond-scale Networked Tasks," Proceedings of ACM SOSP, 2017.

[28] M. E. Haque, Y. He, S. Elnikety, T.D. Nguyen, R. Bianchini and K. McKinley, "Exploiting Heterogeneity for Tail Latency and Energy Efficiency," Proceedings of Annual IEEE/ACM MICRO), 2017.

[29] S. Kanev, K. Hazelwood, G. Wei and D. Brooks, "Tradeoffs between Power Management and Tail Latency in Warehouse-Scale Applications," Proceedings of IEEE International Workshop/Symposium on Workload Characterization, 2014.

[30] M. Nguyen, S. Alesawi, N. Li, H. Che and H. Jiang, "ForkTail: A Black-box Fork-Join Tail Latency Prediction Model for User-facing Datacenter Workloads," Proceedings of HPDC, 2018.

[31] M. Nguyen, S. Alesawi, N. Li, H. Che and H. Jiang, "A Black-Box Fork-Join Latency Prediction Model for Data-Intensive Applications," IEEE Transactions on Parallel and Distributed Systems, vol 31, no 9, pp.1983-3000, 2020.

[32] J. Dean and L. Barroso, "The Tail at Scale," Communications of the ACM, vol 56, no 2, pp.74–80, 2013.

[33] L. Suresh, M. Canini, S. Schmid and A. Feldmann, "C3: cutting tail latency in cloud data stores via adaptive replica selection," Proceeding of USENIX NSDI, 2015.

[34] "Statistical Review," http://www.kaspercpa.com/statisticalreview.htm.

[35] L. Ye, Z. Wang, H. Che and C. Lagoa, "TERSE: A Unified, End-to-end Traffic Control Mechanism to Enable Elastic, Delay Adaptive and Rate Adaptive Services", IEEE Journal on Selected Areas in Communications, vol26, no. 1, pp.938–950, 2011.

[36] Tsuna, "How long does it take to make a context switch?" https://blog.tsunanet.net/2010/11/how-long-does-it-take-to-make-context.html, 2010.

[37] F. David, J. Carlyle and R. Campbell, "Context Switch Overheads for Linux on ARM Platforms", Proceeding of the 2007 Workshop on Experimental Computer Science, 2007.